THEORETICAL INVESTIGATION OF IMMISCIBLE MULTIPHASE FLOW MECHANISMS IN POROUS MEDIA WITH CAPILLARITY

A Dissertation

by

LICHI DENG

Submitted to the Office of Graduate and Professional Studies of
Texas A&M University
in partial fulfillment of the requirements for the degree of

DOCTOR OF PHILOSOPHY

Chair of Committee,	Michael J. King
Committee Members,	Akhil Datta-Gupta
	Eduardo Gildin
	Art Donovan
Head of Department,	Jeff Spath

May 2019

Major Subject: Petroleum Engineering

ABSTRACT

The correct description of multiphase flow mechanism in porous media is an important aspect of research in fluid mechanics, water resources and petroleum engineering. The thorough understanding of these mechanisms is important for many applications such as waterflood, CO_2 sequestration, and enhanced oil recovery. Being different from single phase flow that is well described by Darcy's law and well understood for over 160 years, the multiphase flow mechanism requires more mathematical involvement with more complex fluid interaction which inevitably will incorporate relative permeability and capillary pressure into its description.

For typical two-phase flow problems, especially at the conventional reservoir scale, the Buckley-Leverett flow equations are normally applied with negligible capillarity to capture the flow behavior. However, as we extend our studies to higher resolution using multiscale calculations, or evaluate tighter or higher contrast heterogeneous reservoirs, capillarity becomes increasingly important. Also, for situations such as spontaneous imbibition that wetting fluid is displaced by non-wetting invading fluid, it is possible that capillary force becomes the dominating driving force with negligible viscous and gravity contributions. To better characterize the multiphase flow mechanism with capillarity, in this research, a detailed investigation is carried out in pursuit of more rigorous mathematical description and broader applicability.

The numerical simulation analysis of the described problem has long been a subject of interest with numerous publications addressing it. Being different from the

traditional methods where numerical simulation is used, we pursue the analytical description of the flow behavior using Lagrangian approach which is better in describing these frontal propagation problems. Also, the analytical solution tends to give more insight into the underlying physical characteristics of the problem itself. As one of the most important outcomes, the methodology derives a new dimensionless capillary group that characterizes the relative strength of capillarity at the continuum scale based on the analytical solution. Knowledge of this can be used for stability analyses, with future potential application in the design of computational grids to properly resolve the capillary physics.

DEDICATION

To my beloved parents, Jianmin Deng and Min Yang, who have always loved me unconditionally and taught me to work hard for the things I aspire to achieve.

To my beloved wife, Bo Li, who has been a constant source of support and encouragement.

To my advisor and committee members for their valuable guidance for me to successfully conduct the research.

And to all my friends who shared my happiness and sorrow during my graduate life and study.

ACKNOWLEDGMENTS

First, I would like to thank my committee chair, Dr. Michael J. King, for being an amazing advisor during my overall Ph.D. research journey.

I would also like to extend my sincere gratitude to the other committee members, Dr. Akhil Datta-Gupta, Dr. Eduardo Gildin and Dr. Art Donovan. I want to thank them for their support during my research.

My gratitude also goes to my colleagues and the petroleum engineering department faculty and staff for making my Ph.D. life easy and colorful.

Finally, thanks to my parents and my wife for their continuous support and encouragement.

CONTRIBUTORS AND FUNDING SOURCES

Contributors

Part 1, faculty committee recognition

This work was supervised by a dissertation committee consisting of Professor Michael King, Akhil Datta-Gupta and Eduardo Gildin of the Department of Petroleum Engineering and Professor Art Donovan of the Department of Geology.

Part 2, student/collaborator contributions

All other work conducted for the dissertation was completed by the student independently.

Funding Sources

Graduate study was supported by a fellowship from Texas A&M University and a graduate research assistantship from Energi Simulation (formerly Foundation CMG).

NOMENCLATURE

A	Cross-sectional area
A_{open}	Cross-sectional area open for imbibition
C	Buckley-Leverett frontal speed
C^{Im}	Imbibition proportionality constant – linear flow
$C^{\mathrm{Im},radial}$	Imbibition proportionality constant – radial flow
D	Downward unit vector
D_{frac}	Fracture aperture
F_i	Fractional phase mobility ($i: w = \text{water} / o = \text{oil} / g = \text{gas}$)
f_w	Water fractional flow (normalized to total flux)
f_w^{Im}	Normalized water flux (normalized to inlet water flux)
$\overline{f_w^{\mathrm{Im}}}$	Average normalized water flux (normalized to inlet water flux)
g	Acceleration due to gravity
G	Dimensionless capillary mobility function
h	Thickness
h_{frac}	Fracture height
$H(S)$	Inner saturation function
J	Leverett J-function

J_c	Pre-factor for Leverett J-function
k	Absolute permeability
k_{ri}	Relative permeability ($i: w = \text{water} / o = \text{oil} / g = \text{gas}$)
$\overline{k_{rg}}$	Apparent gas phase relative permeability
l	Total length
L	Rescaled total length or frontal location
m	Exponent for relative permeability model
M	Mobility ratio
$M(S)$	Inner saturation mass function
n	Exponent for relative permeability model
p	Pressure
p_c	Capillary pressure
q	Total flow rate
Q	Imbibed water volume
q_w	Water flow rate
q_{w0}	Water flow rate at the inlet
q_{w0}^{*}	Target water injection rate
R	Ratio of total flow rate and inlet water flow rate
S	Mobile saturation fraction

S_1	Inner saturation at the foot of profile
S_2	Inner saturation at the inlet
S_w	Water saturation
S_{w0}	Free water saturation
S_{wirr}	Irreducible water saturation
S_{wi}	Initial water saturation
S_{orw}	Residual oil saturation
S^*	Buckley-Leverett shock saturation
S^C	Composite saturation
S^O	Outer saturation
S^I	Inner saturation
S^m	Matched saturation
S^C_{inlet}	Composite saturation at the inlet
S^I_{inlet}	Inner saturation at the inlet
S^O_{inlet}	Outer saturation at the inlet
S^O_{foot}	Outer saturation at the foot of profile
t	Time
T	Rescaled time – total volume injected

T^{Im}	Rescaled time – water volume imbibed
u_i	Darcy velocity ($i: w = \text{water} / o = \text{oil} / g = \text{gas} / t = \text{total}$)
u^{Im}	Darcy velocity for spontaneous imbibition
V_{frac}	Fracture bulk volume
x	Distance
x_f	Fracture half-length
X	Rescaled distance – mobile pore volume
X^{Im}	Rescaled distance – pore volume
β	Exponent for capillary pressure function
β_c	Exponent for capillary pressure function
β_i	Exponents for relative permeability ($i: w = \text{water} / o = \text{oil}$)
δ	Combined parameter for gravity term
$\Delta\rho$	Density difference
ε	Small parameter for capillary dispersion
ε_D	Dimensionless capillary group – viscous dominated
$\varepsilon_D{}^{\mathrm{Im}}$	Dimensionless capillary group – capillary dominated
Θ	Heaviside function
λ_D	Dimensionless mobility
λ_i	Mobility ($i: w = \text{water} / o = \text{oil} / g = \text{gas} / t = \text{total}$)

μ_i	Phase viscosity ($i : w = \text{water} / o = \text{oil} / g = \text{gas}$)
ξ	Rescaled distance inner spatial variable
ξ^{Im}	Dimensionless rescaled parameter for saturation profile
σ	Interfacial tension
ϕ	Porosity
ϕ_{frac}	Fracture porosity

TABLE OF CONTENTS

Page

LIST OF FIGURES

Page

LIST OF TABLES

Page

CHAPTER I

INTRODUCTION

1.1 Motivation and Objectives

Immiscible displacement of oil by water or gas is a fundamental reservoir recovery mechanism which has been discussed in numerous publications, and the application of it extends to multiple scales such as lab scale and reservoir scale. At the reservoir scale, multiphase fluid flow is well characterized by the Buckley-Leverett (Buckley and Leverett 1942) flow equations and is usually treated by neglecting capillarity. This is because at this scale the viscosity/mobility ratio is the key factor that controls the efficiency and stability of the displacement, especially after the breakthrough of the injected fluid (Chuoke et al. 1959; Dake 1983; Welge 1952). However, as we extend the studies in higher resolutions using multiscale calculations, or evaluate tighter or higher contrast heterogeneous or fractured reservoirs, capillarity becomes increasingly important. Also, in some reservoir engineering contexts such as naturally fractured carbonate reservoirs or hydraulic fractured unconventional reservoirs, capillarity may become the primary driving force for the recovery.

Due to the complexity of the nature of the nonlinear immiscible displacement partial differential equations including capillarity, universal analytic solutions have remained unavailable. Numerical solutions have been investigated as well (McEven 1959; Fayers and Sheldon 1959), but analytic solutions, due to the nature of the Lagrangian

approach, are better in characterizing these frontal propagation problems. Numerous attempts have been given in the literature about the construction of analytic solution for this type of problems, but most of them require additional and nonessential assumptions which will further limit the applicability. Like Yortsos and Fokas (1983) derived an analytic solution which required specific functional forms for the relative permeability and capillary pressure with respect to saturation. Similar assumptions have continued to be studied in the literature (Desai et al. 2015; Wu and Pan 2003). Some other literature may place other constraints like McWhorter and Sunada (1990) have derived a self-similar solution that doesn't depend upon specific functional forms of the inputs. But their solution requires the injection rate to scale inversely proportional to one over the square root of time. The main purpose of this research is to derive a general solution to the immiscible displacement with as fewer constraints as possible and in accordance with physically achievable boundary conditions.

Another important aspect of this research is to distinguish between different boundary conditions as they will represent totally different mechanisms. For instance, drainage, spontaneous imbibition and forced imbibition are totally different mechanisms. The main difference between drainage and imbibition processes depends on the wettability of the system, and forced imbibition is still viscous dominated mechanism while spontaneous imbibition is mainly capillary dominated. Mathematically, the change of flow conditions will result in a change of boundary conditions to be solved, and in turn, will result in different solutions.

In this research, the first problem addressed is the derivation of the analytic solution for viscous dominated flow condition, or Buckley-Leverett type problems (Buckley and Leverett 1942), where the flux is imposed at the inlet or the inlet boundary condition is fractional flow equals one. In this section, we have treated capillarity as a correction to the original Buckley-Leverett equations and the system is solved using matched asymptotic expansions. The analytic solution has been benchmarked using numerical simulation and is applied to two lab scale problems. One is for the estimation of capillary pressure and relative permeability from displacement saturation profiles, and the other is for the capillary end effect during displacement experiments. The capillary end effect result is further extended for the estimation of relative permeability information from unsteady state experiments as well.

Secondly, the research also analyzed the spontaneous and forced imbibition processes. Recent research has proved that the original work by McWhorter and Sunada (1990) represents the actual boundary conditions of spontaneous imbibition (Schmid and Geiger 2012). But in this research, we will show that the presented methodology by McWhorter and Sunada (1990) has one major assumption that limits its application for physical boundary conditions except for purely counter-current flow conditions. In turn, a new semi-analytic solution is presented to analyze the transient imbibition problem with physical boundary conditions. Also, the impact of imbibition in unconventional reservoirs will be part of the study to analyze the water invasion during hydraulic fracturing and shut-in period, as well as a potential application of a new IOR technique.

1.2 Introduction and Literature Review

1.2.1 Capillary Corrections to Buckley-Leverett Flow

The first section of the research project is aimed to derive a general solution for viscous dominated immiscible displacement flow equations. The work extended the analytic solution of the Buckley-Leverett equations to include capillarity for the co-current flow condition. Specifically, we have solved the incompressible waterflood flow equations along a streamtube or streamline with an arbitrary cross-section for a heterogeneous porous media with variable injection water rate, including capillarity. The methodology is an application of a singular perturbation expansion with matched asymptotic solutions. This solution is presented in the context where the co-current flow is present where we will show that capillarity can be treated as a correction (Deng and King 2015). Also, the resulting analytic solution is benchmarked with high-resolution numerical simulation. One major advantage comparing with existing methodology is the independence of functional forms for capillary pressure and viscous forces, and the solution has also been extended to multiple scales like linear flow, radio flow, and streamtubes. The representation of the analytic solution in streamtubes allows future application in field level waterflood management in terms of representing inter-well connections using streamtubes.

The driving force of the solution is the application of the theory of matched asymptotic expansions and is due to the nature of the resulting singularly perturbed differential equation where the solution changes rapidly in a narrow region. This theory has been used previously to find approximate solutions in which we obtain multi-scale

solutions in either space or in time (Farajzadeh et al. 2013; Wallach 1998; Zazovskii 1985). In our application, the rapid change occurs at the location of the Buckley-Leverett shock. We separate the two-scale problem into an "outer" solution which is valid away from the shock and an "inner" solution which is valid in the vicinity of the shock. The outer solution is identical to the continuous portion of the Buckley-Leverett saturation profile while the inner solution is the stabilized front solution first noted by Terwilliger experimentally (Terwilliger et al. 1951). The two solutions match at the Buckley-Leverett shock saturation and all solutions can be expressed in a closed form. This composite solution is valid at both scales. A preliminary result of this method is presented by King and Dunayevsky (1989) when analyzing the stability of waterflood, but the equations were not fully satisfied at that time. In this research, in order to close all the equation (i.e. to place the inner solution at the right location), a mass balance relationship is used for the moving boundary layer problem (before water breakthrough).

Based on the solution, the length scale of the saturation profile in the vicinity of the shock and its change with time are characterized by a small parameter ε and its dimensionless form ε_D. This parameter is part of the capillary dispersion coefficient which will be obtained as part of the solution. The results imply that the dimensionless group scales inversely with injected volume for linear flow and thus the composite solution reduces to the Buckley-Leverett solution at the late time, irrespective of the strength of capillarity. For linear flow at the early time, the dimensionless group will increase beyond the range for which the capillary correction is possible, indicating capillary dominance. In contrast, for radial flow, the dimensionless group does not depend upon time and the

impact of capillarity does not change with time. Unlike the capillary number which describes the relative magnitude of the capillary and viscous forces at the pore scale (Steigemeir 1977), our dimensionless group describes this quantity at the continuum scale. This dimensionless quantity is universal and widely applicable as we will show the applicability of it in the capillary end effect section and its comparison with Rapoport and Leas scaling group (Rapoport and Leas 1953). It will also be discussed in a later section on spontaneous imbibition.

With the methodology provided, the first application of the results is on capillary pressure function calibration. As the shape of the composite saturation profile around the shock front depends upon the capillary pressure function, in principle we can calibrate the capillary pressure function if the saturation profile is determined experimentally. The measurement can be done using electrical resistivity measurements (Terwilliger et al. 1951), gamma attenuation measurements or X-Ray CT (Nicholls and Heaviside 1988; Wellington and Vinegar 1987). As a demonstration, we will analyze Terwilliger's published experimental data to infer the capillary pressure function and compare it with the conventionally measure capillary pressure curve report in the original paper. This analysis will also help infer the characteristics of the relative permeability by capturing the concave envelope of the fractional flow. One thing to mention is that the original experiment is strictly vertical with downwards flow at a fixed rate. In this case, the outer solution will have a self-similar solution based upon a fractional gas flow which includes the effect of gravity.

Another problem in which capillary corrections arise is at the outlet of a laboratory coreflood (Heaviside and Black 1983). The physical discontinuity at the core outlet or at the wellbore has led to the discontinuity in capillary pressure at the outlet-face, and it further caused a capillary force to persist in the porous-media system. This phenomenon tends to build up a saturation bank for the preferentially wetting phase at the efflux end (Hadley and Handy 1956). The outlet boundary condition, capillary pressure equals zero, here follows from phase pressure continuity for each of the two phases. With the inclusion of capillarity in the description, we changed the previously moving boundary layer problem into a stationary boundary layer problem at a finite length. Unlike the moving boundary layer problem, there is no need for a mass balance constraint to close the equations. We can evaluate the impact the end effect on the lab determination of relative permeability using the unsteady state JBN method (Johnson et al. 1959). There are variations of the JBN method, and one of the alternatives is a graphical interpretation of the unsteady state experiments' data proposed by Jones and Roszelle (1978). However, both the original JBN calculation and its variations neglect the existence of capillary pressure, or in this context, capillary end effect. Our analysis indicates that the end effect has no impact on the outlet fractional flow itself, but as the outlet saturation is determined from the average saturation, it does include the impact of capillarity. The mobility function is determined from the outlet pressure gradient which itself is determined from the total pressure drop across the core, and is impacted by capillarity. Based on the asymptotic analysis, we expect the error introduced into the inferred outlet pressure gradient to be

larger than that introduced into the outlet saturation, leading to an overall suppression of the total mobility.

As we have already discussed the limitation of the JBN method in determining relative permeability information which is based on the Buckley-Leverett theory without capillarity, we have extended the application of the derived analytic solution to improve the estimation of relative permeability from laboratory displacement experiments. The main disadvantage of applying the traditional JBN method is the requirement of high flow rate, which in turn would require the experiments to be conducted at flow rates higher than the true reservoir conditions. These high flow rates might also cause instability in the displacement as well as fines migration problems (Chuoke et al. 1959; Qadeer et al. 1988). In the literature, many attempts have been made to address this issue. Sigmund and McCaffery (1979) have used non-linear regression to match experimental data using power-law modeled relative permeability. Similar work has been done by Batycky et al. (1981), Kerig and Watson (1986) and Richmond and Watsons (1990).

We have used the derived analytic model to calculate accurate relative permeability by matching experimental pressure drop and production responses. (Deng and King 2016). The data used is cited from Richmond and Watsons (1990) and the comparison between our analytic inversion and the original numerical simulation-based inversion results is presented.

1.2.2 Spontaneous Imbibition

Spontaneous imbibition is a very important recovery mechanism that was widely discussed in the fractured carbonate reservoir literature. Unlike forced imbibition where the injection flow rate is imposed, for spontaneous imbibition, the injection rate is a consequence of the physical properties of the medium. The spontaneous imbibition is a mechanism that is more capillary dominated while the forced imbibition is more viscous dominated. As we have introduced, the work by McWhorter and Sunada (1990) and the references therein have provided an exact solution to a fractional flow boundary value problem in the form of an iterative integral equation, and this derivation has become a benchmark in the literature to analytically calculate the self-similar solution to two-phase spontaneous imbibition. The later work by Schmid and Geiger (2012) has proved that the problem solved by McWhorter and Sunada satisfies the correct boundary conditions for spontaneous imbibition.

However, the assumption inherent in the self-similar solution that the ratio between the outlet hydrocarbon flux and the total inlet flux must remain constant has placed another constraint on the applicability. This constraint is not natural unless the system is infinite or only one end of the system is open to flow. This drawback of not being able to properly characterize the behavior of transient imbibition process is first discussed by Nooruddin and Blunt (2016) where they considered a finite length problem. But their derivation still uses the self-similar solution as the basis, making the solution and assumption being contradictory. In this part of the research, we first introduced an average normalized water flux to present the analytic solution to the transient problem without any unnecessary

constraints. Later, we introduced the application of the transient solution to constant outlet flux boundary condition. Furthermore, we have extended the transient imbibition solution to the Two-Ends-Open (TEO) free spontaneous imbibition, which is the same experimental configuration as discussed by Nooruddin and Blunt (Deng and King 2018c).

Two-Ends-Open (TEO) free spontaneous imbibition, is a laboratory scale experiment from which, in principle, capillary pressure and relative permeability information may be obtained. It is essentially a one-dimensional flow experiment in which one end face of a core is exposed to the wetting phase and the other end exposed to the non-wetting phase. This leads to a system with non-wetting phase produced both co-currently and counter-currently. This spontaneous imbibition test configuration has been used in the literature to infer capillary pressure and relative permeability. However, most techniques require either unnecessary assumptions for the analytic solution such as piston-like displacement (Haugen et al. 2014; Ferno et al. 2015), or require numerical simulation to predict the flow behavior (Ruth et al. 2015). The experiments also allow the interpretation of capillary back pressure at the water-wetted face which caused the cessation of counter-current oil flow at later period of the experiment (Haugen et al. 2014). However, the capillary back pressure is not within the scope of this study.

The solution strategy is a back-ward finite differencing technique that is similar to the approach proposed by Schmid et al. (2016). The difference in our research is that we have used an improved finite difference scenario that changed from the previous finite difference of one PDEs to a set of finite difference for three linear ODEs. This application will reveal more fundamentals about the underlying physics behind the solution itself and

will help explain the instability the previous researchers have experienced. Some other techniques originally developed to be applied for the McWhorter and Sunada equations include the original iterative approximation or its improved form (Fucik et al. 2007), the pseudospectral approach (Bjornara and Mathias 2013), etc. The finite difference approach is a lot more straightforward and easier to implement.

We have also introduced another target injection rate at the inlet to study the transition from spontaneous to forced imbibition. As the earlier stage, the water imbibition rate is infinite, and water will be sucked into the core at a rate a lot higher than the target rate. During this stage, it is the capillary pressure that prevails and spontaneous imbibition dominates. But as the imbibition rate drops, the water flux at the inlet will drop to the target rate and then the viscous pressure drop will dominate and keep the inlet water flux constant. Thus, the overall flow mechanism enters forced imbibition by a prescribed flux.

The main output of this part is a stability envelope outside which the flow is not stable. For any point above the formed envelope, the flow is unstable due to capillarity and will be pushed back onto the envelope. For all points on the envelope, it is at spontaneous imbibition state. And for all points below the envelope, it is stable and at forced imbibition state. This envelope is universal as it does not depend on the prescribed outlet flux. Also, the vertical axis of the stability envelope is the dimensionless parameter ε_D which we have already discussed in the previous work. Here our method has again shown that this parameter is a result of the intrinsic properties of the rock and fluid system, and it is applicable in both capillary dominated and viscous dominated flow conditions. (Deng and King 2018a).

1.2.3 Application in Unconventional Reservoirs

Spontaneous imbibition is not only important for fractured reservoirs. As for unconventional reservoirs like shale oil or shale gas, the decreasing permeability has made the capillarity more and more important, spontaneous imbibition is also important. In this part of the research, the application of the spontaneous and forced imbibition in unconventional reservoirs will be studied. Specifically, the process of hydraulic fracturing and the shut-in time thereafter until production will be analyzed (Deng and King 2018b).

One specific context for the analysis is the "water blocking" effect. During a hydraulic fracturing process, a great amount of fracturing fluid is injected to create fractures so that the contact area of the wellbore with the reservoir can be significantly increased (Cheng 2012). However, after the fracturing process, only small amount of the fracturing fluid is recovered as flowback and a significant amount of the injected fluid is lost to the formation (Longoria et al. 2017). With the water left inside the formation, mainly literature has studied the damage caused for hydrocarbon production. These concerns include but not limited to permeability damage and relative permeability damage caused by water invasion and gathering in the vicinity of the fracture surface (Tannich 1975; Holditch 1979; Abrams and Vinegar 1985; Bostrom et al 2014; Das et al. 2014). Our focus in this part of the research is going to be focused on the water blocking effect in terms of hydrocarbon relative permeability reduction and its impact on production.

From the relative permeability point of view, minimizing the water invasion into the matrix is very desirable as higher water saturation would lead to lower relative

permeability for the hydrocarbon phase (Longoria et al. 2015). However, in many cases with little fracturing fluid flowing back, the production seems to be not affected or even enhanced with long shut-in well soaking for up to months, especially for gas shale plays like Marcellus (Shaoul et al 2011; Cheng 2012; Dutta et al. 2012; Bertoncello et al. 2014). Thus, there lies a direct contradiction between the mobility reduction theory and the field observations. In this research, we would like to investigate the water invasion mechanisms and to reconcile the contradiction between water blocking theory and well soaking operations for shale gas reservoirs.

On the mechanisms controlling water loss after the fracturing process, some studies suggest trapping of water in unconnected secondary fractures (Fan et al. 2010), incomplete drainage in induced fractures due to adverse mobility ratio and gravity segregation (Kuru et al. 2013; Parmar et al. 2014) or liquid loading in the lower part of the propped fracture (Agrawal and Sharma 2013). But there are more researches focused on the imbibition theory associated with capillary pressure and its role in sucking the water into the matrix and causing a large amount of water leaking into the formation (Roychaudhuri et al. 2011; Odusina et al. 2011; Makhanov et al. 2014). One important upside of the imbibition is the counter-current gas flow it will create and the associated release of gas from the tight pores (Dehghanpour et al. 2012; Agrawal and Sharma 2013). Most spontaneous imbibition theory predicts high initial flow rate at the early period of time, and the ultralow permeability in these shale gas reservoirs would even have longer and faster early flow rate due to high capillarity. This is important as if the counter-current gas flow is really more impactful comparing with the water blocking damage the imbibed

water is generating, then maybe the imbibition mechanism could be treated as a production mechanism instead of a blocking mechanism.

To properly model the fluid exchange between the matrix and the fracture during the soaking period, we have extended our previous methodology of the analytic solution for spontaneous imbibition to include two more controlling factors. The first added component to the self-similar McWhorter and Sunada's solution is the water adsorption effect for sub-irreducible initial water saturation conditions. Some researchers report in some gas shales like Marcellus and Haynesville, the water saturation is well below irreducible (Bennion and Thomas 2005; Wang and Reed 2009; McWhorter 2017). At the interval between initial water saturation and irreducible water saturation, the water is theoretically not able to flow but is being controlled by adsorption due to the presence of clay minerals. In this research, we try to combine the spontaneous imbibition and water adsorption below irreducible water saturation together at the continuum scale to extend the analytic solution's applicability. The second component is the gravity segregation inside the fracture (Cheng 2012; Agrawal and Sharma 2013). The gravity segregation and resulting flowing area reduction in the fracture will cause the higher decline of the imbibition rate compared with a 1D self-similar solution. In the current scope of this research, the gravity effect is considered to be instantaneous to obtain the analytic solution of the coupled phenomenon.

CHAPTER II

CAPILLARY CORRECTIONS TO BUCKLEY-LEVERETT FLOW[*†]

2.1 Introduction

At the reservoir scale, multiphase fluid flow is well characterized by the Buckley-Leverett flow equations, neglecting capillarity. However, as we extend our studies in higher resolution using multiscale calculations, or evaluate tighter or higher contrast heterogeneous or fractured reservoirs, capillarity becomes increasingly important. To improve the understanding of these situations, we have extended the analytic solution of the Buckley-Leverett equations to include capillarity for the forced imbibition co-current flow case. Specifically, we have solved the incompressible waterflood flow equations along a streamtube or streamline with an arbitrary cross-section for a heterogeneous porous media with variable injection water rate, including capillarity. The methodology is an application of a singular perturbation expansion with matched asymptotic solutions. The outer solution is identical to the continuous portion of the Buckley-Leverett saturation profile while the inner solution is the stabilized front solution first noted by Terwilliger experimentally. The two solutions match at the Buckley-Leverett shock saturation and all

[*] Part of this chapter is reprinted with permission from "Capillary Corrections to Buckley-Leverett Flow" by Deng and King, 2015. Paper SPE-175150-MS presented at the SPE Annual Technical Conference and Exhibition, Houston, 28-30 September. Copyright 2015, Society of Petroleum Engineers. Further reproduction prohibited without permission.

[†] Part of this chapter is reprinted with permission from "Estimation of Relative Permeability from Laboratory Displacement Experiments Application of the Analytic Solution with Capillary Corrections" by Deng and King, 2016. Paper SPE-183139-MS presented at the SPE Abu Dhabi International Petroleum Exhibition and Conference, Abu Dhabi, 7-10 November. Copyright 2016, Society of Petroleum Engineers. Further reproduction prohibited without permission.

solutions can be expressed in a closed form. This solution is presented in the context where the co-current flow is present where we will show that capillarity can be treated as a correction. The result of this analytical solution is tested against high-resolution flow simulation to verify its validity. This analysis is also applied to the calculation of capillary end effects in laboratory core floods, where the length scale of the saturation correction can be predicted. We also demonstrate, as the shape of the saturation profile near the front depends upon the capillary pressure function, that this analytical solution can be used to interpret experimental data and derive and calibrate the capillary pressure function. To be noted, due to specific boundary condition we are analyzing in this chapter, the solution applies to the cases where the flow is still viscous dominated (i.e. drainage or forced imbibition). This means the capillarity is, to some extent, small and can be treated as a correction to the viscous flow. The flow condition where the capillarity dominates will be examined in the next chapter.

2.2 Methodology

We will begin the discussion of the analytic solution with a description of incompressible fractional flow theory. This will allow us to review its application along streamlines, which are equivalent to streamtubes with variable flow geometry, and to define notations for the analytic solutions.

For incompressible waterflood in three dimensions:

$$\phi \frac{\partial S_w}{\partial t} + \nabla \cdot \vec{u}_w = 0 \tag{2.1}$$

$$\nabla \cdot \vec{u} = 0 \tag{2.2}$$

$$\vec{u}_w = F_w \vec{u} + \frac{1}{\mu_o} \lambda_D F_w F_o \vec{\vec{k}} \cdot \left(\nabla p_c + \Delta \rho g D \right) \tag{2.3}$$

Here, F_w and F_o are the fractional mobility functions for water and oil phases respectively, and λ_D is the dimensionless total mobility (normalized to the mobility of the oil phase).

$$\begin{aligned} F_w(S) &= \frac{k_{rw}(S)/\mu_w}{k_{rw}(S)/\mu_w + k_{ro}(S)/\mu_o} \qquad F_o(S) = \frac{k_{ro}(S)/\mu_o}{k_{rw}(S)/\mu_w + k_{ro}(S)/\mu_o} \\ \lambda_D(S) &= k_{ro}(S) + \frac{\mu_o}{\mu_w} k_{rw}(S) \qquad\qquad S = \frac{S_w - S_{wirr}}{1 - S_{orw} - S_{wirr}} \end{aligned} \tag{2.4}$$

A permeability tensor is used to express any permeability anisotropy. We may determine the effective cross-sectional area along a streamline in terms of the steady state flux, q, and the local velocity, $\vec{u}(x)$.

$$\vec{u}(x) = x\, q / A(x) \tag{2.5}$$

Here x is the distance coordinate along the streamline. This allows us to express the three-dimensional waterflood equation as a one-dimensional equation along the streamline.

$$\phi \frac{\partial S_w}{\partial t} + \frac{1}{A(x)} \frac{\partial q_w}{\partial x} = 0 \tag{2.6}$$

$$q_w = A(x)\, x \bullet \vec{u}_w = F_w q(t) + \frac{A(x)}{\mu_o} F_w F_o \lambda_D\, x \bullet \vec{\vec{k}} \bullet \left(x \frac{\partial p_c}{\partial x} + \Delta\rho g D \right) \tag{2.7}$$

The total flux, $q(t) = x \cdot \vec{u}$, may now vary with time. In three-dimensional streamline simulation, flux coupling between streamlines is included using operator splitting techniques. These cross-flux terms are neglected in the current treatment, but the use of an equivalent one-dimensional streamtube model with an arbitrary cross-sectional area allows us to treat various geometries (linear, radial, radial line source, etc.) in a consistent fashion. The permeability tensor can be expressed along the direction of the streamline and in terms of a dip angle.

$$k = x \bullet \vec{\vec{k}} \bullet x \quad x \bullet \vec{\vec{k}} \bullet D = k_z\, x \bullet D \tag{2.8}$$

We may define the fractional flow as the flux of water normalized to the total flux.

$$f_w = \frac{q_w}{q(t)} = F_w + \frac{A(x)}{\mu_o q(t)} F_w F_o \lambda_D \left(k \frac{\partial p_c}{\partial x} + k_z \Delta\rho g\, x \bullet D \right) \tag{2.9}$$

It is convenient to introduce the cumulative mobile pore volume along the streamtube as a spatial variable and the cumulative volume injected as a time variable.

$$X(x) = (1 - S_{orw} - S_{wirr}) \int_0 A(x) \phi(x)\, dx \tag{2.10}$$

$$T(t) = \int_0 q(t)\, dt \tag{2.11}$$

Finally, we obtain the waterflood equations in terms of the fractional flow.

$$\frac{\partial S}{\partial T}+\frac{\partial f_w}{\partial X}=0 \tag{2.12}$$

$$f_w=F_w(S)+\frac{A(x)}{\mu_o q(t)}F_w(S)F_o(S)\lambda_D(S)\left(k(x)\frac{\partial p_C}{\partial x}+k_z(x)\Delta\rho g x\bullet D(x)\right) \tag{2.13}$$

Here we utilize the normalized water saturation, $S=(S_w-S_{wiirr})/(1-S_{orw}-S_{wirr})$. The capillary pressure function will be assumed to follow a Leverett J-function.

$$p_c=\sigma\sqrt{\frac{\phi(x)}{k(x)}}J(S) \tag{2.14}$$

The functional dependence of each term is shown to emphasize the reservoir heterogeneity (functions of x) and the non-linear functions of saturation, S_w.

With the inclusion of capillarity, the resulting equation is a degenerate parabolic differential equation, for which the solutions must be continuous and differentiable. The exceptions are at the specific saturation $S=0,1$, where $F_w\cdot F_o=0$, and where the saturation must be uniform and continuous, but not necessarily the slope, $\partial S/\partial x$. All of the solutions being considered have the initial saturation equal to the irreducible water saturation for which F_w vanishes: $S=0$, $F_w(0)=0$. We define the "foot" as the location at which $S=0$ and $f_w=0$. We will show that the foot may be at infinity or at a finite location, depending upon the scaling of $\frac{F_w}{S}\frac{dp_c}{dS}$ as $S\to 0$. In the absence of capillarity, these equations support weak solutions with discontinuities that propagate with a shock speed given by $[f_w]/[S]$. Here $[Q]=Q_{left}-Q_{right}$ signifies the discontinuity of a property,

Q, across the shock. For instance, for the Buckley-Leverett solution, the shock location is at the foot of the saturation profile.

An analysis of the continuity requirements of these equations is important to understand the impact of heterogeneity and to correctly specify the boundary conditions. For instance, if the porosity or permeability were discontinuous, as may arise when abutted several cores in a laboratory core flood, Eq (2.9) implies that the capillary pressure must be continuous at the discontinuity. In other words, the saturation, governed by the J-function, will be discontinuous, but in such a way as to maintain capillary continuity. If phase pressures are continuous on the boundary of the system in a laboratory, then capillary pressure continuity requires that $p_c = 0$ on the boundary, and the saturation is fixed. This gives rise to the capillary end effect seen in laboratory core floods.

2.2.1 Buckley-Leverett Solution Review

Let us now consider the solution to Eq (2.7) for waterflood in a horizontal system in the absence of capillarity, and with a uniform initial saturation at the irreducible water saturation, $S = 0$. This equation has a well-known continuous solution which describes a saturation profile for saturations above a shock saturation, $S > S^*$.

$$\left(\frac{\partial X}{\partial T}\right)_S = \frac{dF_w}{dS} = F_w'(S) \quad or \quad X = T \cdot F_w'(S) \tag{2.15}$$

The differential equation also supports discontinuous ("weak") solutions. Consistency with the continuous solution determines the shock saturation, S^*, and shock speed, $c\left(S^*\right)$.

$$F_w'(S^*) = \frac{\left[F_w(S)\right]}{[S]} = \frac{F_w(S^*)}{S^*} \equiv c(S^*) \quad or \quad 0 = \frac{d}{dS^*}\left(\frac{F_w(S^*)}{S^*}\right) = \frac{dc(S^*)}{dS^*} \tag{2.16}$$

In addition to this shock construction, there is an Entropy condition which selects among multiple possible shock solutions (Bell and Shubin 1985; Osher 1984). In our context, both constructions are equivalent to obtaining the shock saturation S^*, which maximizes the shock speed, $c(S^*)$. This result may also be summarized as a concave envelope fractional flow relationship.

$$f_w = \begin{cases} cS & S < S^* \\ F_w(S) & S > S^* \end{cases} \tag{2.17}$$

This is Welge's graphical construction and the self-similar Buckley-Leverett solution. The solution satisfies the flux boundary condition at the water injector, $f_w = 1$, and the initial condition, $S = 0$.

Still neglecting capillarity, if we consider the fractional flow relationship with gravity, we find that the fractional flow needs no longer be simply a function of saturation, as it has an additional term given by $\frac{A(x)}{q(t)}\frac{k_z}{\mu_o}F_w F_o \lambda_D \Delta\rho g\, x\cdot D$. Even for a homogeneous medium, the dip angle, $x\cdot D$, and the cross-sectional area, $A(x)$, may depend upon location, and the flux may depend upon time. In this case, the Buckley-Leverett equations may still be formulated and solved, but there will not be a self-similar solution which depends solely upon the dimensionless ratio $X(x)/T(t)$. The exception is for strictly vertical or horizontal geometries that may arise in laboratory measurements or in

mechanistic models, in which case the solution technique is identical to the above but with a modified fractional flow. In the next sections of the capillary corrections methodology part, we will neglect gravity and focus on capillarity.

2.2.2 Capillary Corrections Solution with Matched Asymptotic Expansions

Following the solution of King and Dunayevsky (1989), we will now analyze the flow equations using the methodology of matched asymptotic expansions. The resulting solutions are as general as the Buckley-Leverett solutions in their treatment of flow rate, geometry, and heterogeneity. We can formally obtain the Buckley-Leverett equations from the fractional flow, Eq (2.12) and Eq (2.13), in the limit of small capillarity, $\sigma \to 0$. However, when we do so, we reduce the order of the differential equation from second order to first, in what is known as a singular perturbation. In our application, the rapid change occurs at the location of the Buckley-Leverett shock. We separate the two scale problem into an "outer" solution which is valid away from the shock and an "inner" solution which is valid in the vicinity of the shock. The two are combined into a composite solution which is valid at both scales using the approach of matched asymptotic expansions.

The following figures show the workflow steps in the construction of the composite saturation profile, and the inner, outer, and composite saturation profiles from an example calculation.

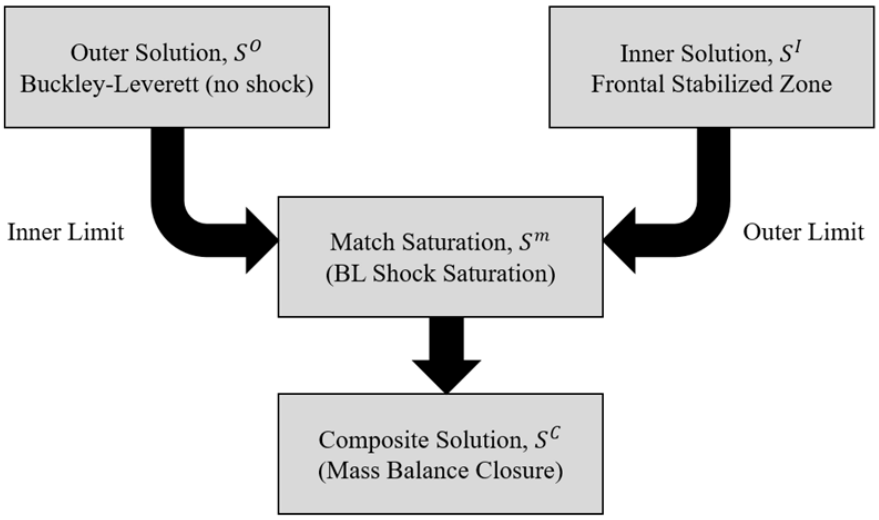

Figure 2.1 Workflow steps for calculating the composite saturation profile

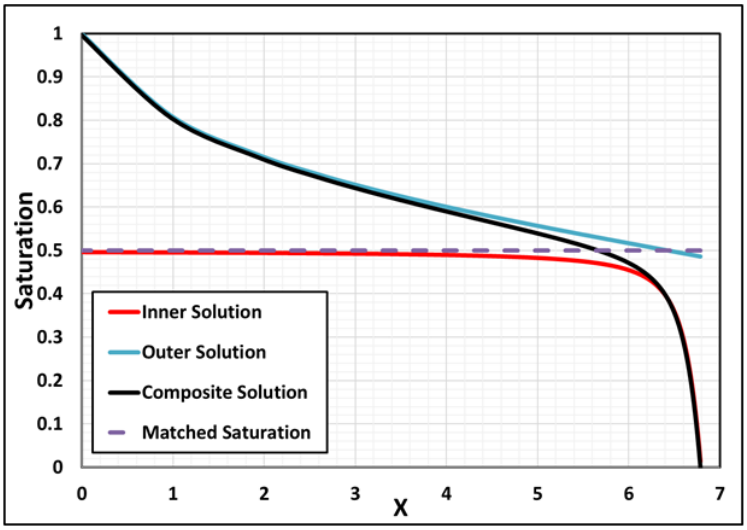

Figure 2.2 Example composite saturation profile from matched asymptotic

The outer solution is identical to the continuous portion of the Buckley-Leverett solution, without the shock. The inner solution is the stabilized front solution first observed by Terwilliger. The match of these two asymptotic solutions will occur at the Buckley-Leverett shock saturation. Some authors have commented that although the

method of matched asymptotic expansions is a standard approach for solving multi-scale problems, that the physical origin of the integrals in the solutions is hard to interpret (Babchin et al. 2008). In our case, we find a clear relationship between these mathematical solutions and previously developed self-similar solutions. As noted by Chen (1988), and attributed to Barenblatt (1952), it is expected that physically complex and complete solutions often have a relationship to self-similar solutions, and we will see that this is the case here. Although the composite solution is not itself self-similar, both the inner and outer solutions are individually self-similar solutions.

For the outer solution, we can formally obtain the outer equations from the fractional flow, Eq (2.12) and Eq (2.13), in the limit of small capillarity, $\sigma \to 0$, $f_w \to F_w(S)$. This is recognized as being identical to the Buckley-Leverett equation, with the solution given by Eq (2.15).

$$X = T \cdot F_w'(S^O) \tag{2.18}$$

This is the outer solution, S^O, which is a function of X/T, and is shown in Figure 2.2. It satisfies the inlet boundary condition: $f_w = F_w\left(S^O\right) = 1$ at $S^O = 1$. Unlike the Buckley-Leverett solution, the outer solution has no shock. Instead, the initial saturation will be reached through the inner solution.

As for the inner solution, we can consistently neglect the capillary pressure terms in Eq (2.13) to obtain the Buckley-Leverett solution except at the shock itself. Irrespective of the strength (or weakness) of capillarity, at the shock, $\partial S/\partial x \to -\infty$, and the capillary

contributions to the fractional flow become significant. From the expression of the capillary pressure in terms of the Leverett J-function, we have:

$$\frac{\partial p_c}{\partial x} = \sigma\sqrt{\frac{\phi}{k}}\left[\left(\frac{d}{dx}\ln\sqrt{\frac{\phi}{k}}\right)J(S) + J'(S)\frac{\partial S}{\partial x}\right] \approx \sigma\sqrt{\frac{\phi}{k}}J'(S)\frac{\partial S}{\partial x} = \sigma\sqrt{\frac{\phi}{k}}J'(S)\frac{dX}{dx}\frac{\partial S}{\partial X} \tag{2.19}$$

We have assumed that the heterogeneity in the porosity and permeability is sufficiently smooth that the saturation gradients dominate in this derivative, at least in the vicinity of the shock. (If not, then the problem needs to be divided into two domains with continuous capillary pressure across the jump in the porosity-permeability.) This allows us to express the fractional flow as a non-linear convection-diffusion problem:

$$f_w = F_w(S) - \frac{\varepsilon(x)}{q(t)}G(S)\frac{\partial S}{\partial X} \tag{2.20}$$

$$\varepsilon(x) = \frac{\sigma}{\mu_o}A(x)\frac{dX}{dx}(x)\sqrt{k(x)\phi(x)} \tag{2.21}$$

$$G(S) = -\lambda_D(S)F_w(S)F_o(S)J'(S) \tag{2.22}$$

Here, $\varepsilon(x)/q(t)$ is a characteristic volume, which is small in a sense to be determined as part of the solution of these equations as $\sigma \to 0$, and $G(S)$ is a dimensionless non-linear diffusion coefficient. This flux expression is very general as it includes variations in flow rate, heterogeneity in porosity and permeability, and the variation of cross-sectional area. As special cases, it includes linear flow $A = Const$, radial flow $A(x) = 2\pi xh$, or with a finite wellbore radius, $A(x) = 2\pi(x + r_w)h$.

We are interested in solutions to these equations for capillary corrections, in which the impact of capillarity is, in some sense, local. In the absence of capillarity, these fractional flow solutions will have a saturation shock. Away from the shock, capillarity may be neglected in a consistent fashion. However, at the shock, where $\partial S/\partial X \to -\infty$ and hence $\partial p_c/\partial X \to \infty$, the capillary pressure is not negligible. Eq (2.20) is in the form where the highest order spatial derivative has a small coefficient, and can be neglected except within the vicinity of a shock. This kind of singularly perturbed differential equations have solutions that change rapidly in a narrow region and can be analyzed using the method of matched asymptotic expansions.

To obtain the governing equations in the vicinity of the shock, we expand the length scale through the following change of variables, $(x,t) \to (\xi, T)$ where:

$$\xi = \frac{X - L(T)}{\sigma} \tag{2.23}$$

The function $L(T)$ is to be determined. The functions $X(x)$ and $T(t)$ were defined as part of the Buckley-Leverett construction. In these moving coordinates the space and time derivatives are as follows:

$$\frac{\partial}{\partial X} = \frac{1}{\sigma}\frac{\partial}{\partial \xi} \tag{2.24}$$

$$\frac{\partial}{\partial t} = q\frac{\partial}{\partial T} - \frac{1}{\sigma}\frac{dL}{dT}q\frac{\partial}{\partial \xi} \to -\frac{1}{\sigma}\frac{dL}{dT}q\frac{\partial}{\partial \xi} \tag{2.25}$$

Here we have taken the limit $\sigma \to 0$. Eqs (2.6) and (2.20) may now be expressed in this limit.

$$0 = -\frac{dL}{dT}\frac{\partial S^I}{\partial \xi} + \frac{\partial f_w}{\partial \xi} = \frac{\partial}{\partial \xi}\left\{-\frac{dL}{dT}S^I + f_w\right\} \tag{2.26}$$

$$f_w = F_w\left(S^I\right) - \frac{\varepsilon\left(x(t)\right)}{\sigma}\frac{1}{q(t)}G\left(S^I\right)\frac{\partial S^I}{\partial \xi} = F_w\left(S^I\right) - \frac{\varepsilon\left(x(t)\right)}{q(t)}G\left(S^I\right)\frac{\partial S^I}{\partial X} \tag{2.27}$$

The fractional flow is now expressed in terms of the inner saturation. The spatial dependence of $\varepsilon(x)$ has become a function of time since $X(x) = L(T)$ in the limit $\sigma \to 0$. The convection-diffusion equation, Eq (2.26), is in the form where we may take a first integral, and utilize the boundary condition at the foot of the inner solution, $f_w = 0$ at $S = 0$. For convenience, we define $c(T) = dL/dT$.

$$cS^I = f_w = F_w\left(S^I\right) - \frac{\varepsilon\left(x(t)\right)}{q(t)}G\left(S^I\right)\frac{\partial S^I}{\partial X} \tag{2.28}$$

We see that the water flux increases linearly with saturation for the inner solution, just as in the concave envelope of Welge's graphical construction. We will also show that this linear increase will lead to the steady state saturation profile first noted experimentally by Terwilliger.

This equation can be integrated to obtain the inner saturation profile, which is also shown in Figure 2.2.

$$X = X_0(t) - \frac{\varepsilon\left(x(t)\right)}{q(t)}\int_{S=0}^{S^I}\frac{G(S)}{cS - F_w(S)}dS = X_0(t) - \frac{\varepsilon\left(x(t)\right)}{q(t)}H\left(S^I\right) \tag{2.29}$$

We have defined an implicit function for the inner solution, $H\left(S^I\right)$, in terms of the integral in Eq (2.29). We recognize this as Terwilliger's stabilized front solution. The

constant of integration, $X_0(t)$, is approximately at the location $X(x)=L(T)$, so this solution is moving with the Buckley-Leverett shock. Away from the shock, $X \ll X_0$, the integrand in $H(S)$ must diverge and so the inner saturation approaches a constant for which $c = F_w(S^I)/S^I$.

We have implicitly assumed that the integral converges as $S \to 0$ and that the foot of the profile will be at a finite location. This will be the case for all of the examples in the current study. The location for the foot and $X_0(t)$, will be obtained by a mass balance closure relationship based upon the composite solution.

The match saturation relates the inner and outer solutions. We have seen that the outer solution satisfies the inlet boundary condition, but not the saturation foot boundary condition. In contrast, the inner solution satisfies the saturation boundary condition at the foot, but not the inlet. These two profiles are related through the match saturation. At the matched asymptotes, the inner limit of the outer solution $(\sigma \to 0, X \to L(T), S^O \to S^m)$ must match the outer limit of the inner solution $(\sigma \to 0, \xi \to -\infty, S^I \to S^m)$.

$$S^m(T) = \lim_{x \to L(T)} S^O(X,T) = \lim_{\xi \to -\infty} S^I(\xi,T) \tag{2.30}$$

From Eq (2.18) we may take the inner limit of the outer solution $(\sigma \to 0, X \to L(T))$ to obtain:

$$L(T) = T \cdot F_w'(S^m) \tag{2.31}$$

The outer limit of the inner solution $(\sigma \to 0, \xi \to -\infty)$ can only be achieved if the integrand in Eq (2.29) diverges.

$$c = \frac{dL}{dT} = \frac{F_w(S^m)}{S^m} \tag{2.32}$$

Combining these two equations gives the match saturation as a function of T: $F_w(S^m) - S^m F_w'(S^m) = a/T$. Since this function of S^m is bounded, the constant a must vanish for the match at early time. As a result, the match saturation is the Buckley-Leverett shock saturation, $S^m = S^*$. Here, c is the shock speed and, $L(T) = cT$ is the shock location.

Knowing the match saturation, we may now construct the composite solution, Figure 2.2.

$$S^C(X,T) = S^O(X,T) + S^I(\xi,T) - S^* \tag{2.33}$$

The composite solution is continuous and does not itself experiences a shock. Away from the shock, $S^I \to S^*$ and the composite solution approaches the outer solution. Near the shock, $S^O \to S^*$ and the composite solution follows the inner solution. The composite solution smoothly interpolates between the two. We can also express the fractional flow as a composite. Away from the shock, $f_w \to F_w(S^O)$, while near the shock, $f_w \to cS^I$. We have recovered Welge's construction, Eq (2.17), in the limit $\sigma \to 0$. For

finite capillarity, a more accurate result is obtained from Eq (2.20), in terms of the composite saturation.

Also, as mentioned before, to complete the construction of the composite saturation profile, a mass balance relationship is required to close all the equations. The detailed derivation about the mass balance closure is discussed in Appendix A.

One important parameter derived from this methodology is the dimensionless variable ε_D which represents the strength of capillarity.

$$\varepsilon_D = \frac{\varepsilon}{qT} \tag{2.34}$$

The above parameter not only provides the characteristics of the strength of capillarity for a specific system, it also controls the validity of the perturbation expansion, which is further discussed in Appendix A as well.

2.2.3 Model Validation

In order to verify the validity of our analytical model, we compare the results of our model to high-resolution finite difference flow simulation. The high-resolution 1-D simulation was performed using Eclipse and the input parameters listed in Table 2.1. The total length of the system is 100 ft.

M	3	J_c	1	$\mu_w(cp)$	0.5
$\mu_o(cp)$	2	$\sigma(dync/cm)$	20	S_{orw}	0
S_{wi}	0	ϕ	0.2	$A(ft^2)$	1
$k(mD)$	200	S_c	1		

Table 2.1 Input parameters for capillary corrections to B-L flow example calculations

The following functional forms are used for the relative permeability and capillary pressure (Leverett J-function) for all example calculations in this section:

$$\frac{k_{ro}}{\mu_o} = \frac{(1-S)^2}{\mu_o} \tag{2.35}$$

$$\frac{k_{rw}}{\mu_w} = \frac{MS^2}{\mu_o} \tag{2.36}$$

$$J = -J_c \ln\left(\frac{S}{S_c}\right) \tag{2.37}$$

As indicated in the above three equations, the relative permeability is represented using a quadratic function and the capillary pressure relationship is characterized by a logarithmic Leverett-J function as functions of the normalized mobile water saturation fraction. In the analytical model both the capillary pressure function and relative permeability function are included within the derivation thus all derivatives and integrals can be performed analytically. For the finite difference simulator, these functions are

expressed in a tabulated form. Relative permeability and capillary pressure curves are shown in Figure 2.3a and Figure 2.3b.

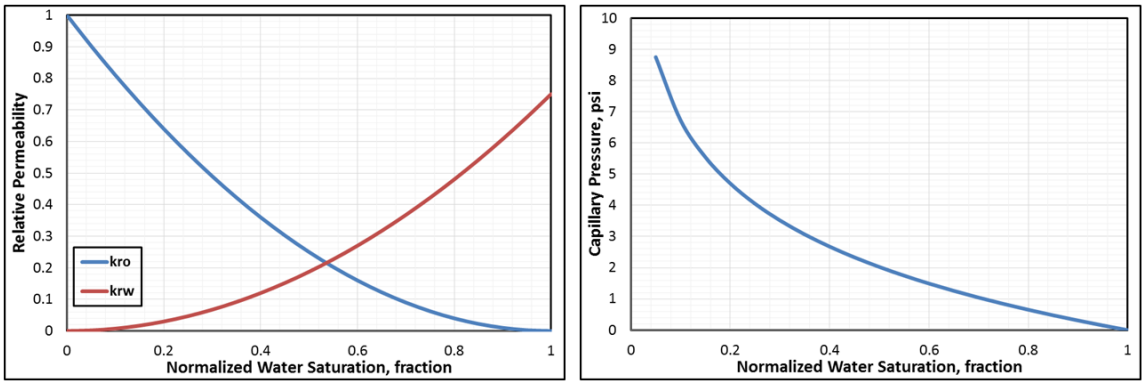

Figure 2.3 (a)-Model input of relative permeability; (b)-model input of capillary pressure

Both the analytical model and the flow simulation were tested under two different constant flow rates $q = 0.3\ RB/day$ and $q = 1\ RB/day$. Figure 2.4 and Figure 2.5 show the comparison results. The simulation results were obtained for N=10,000 grid blocks.

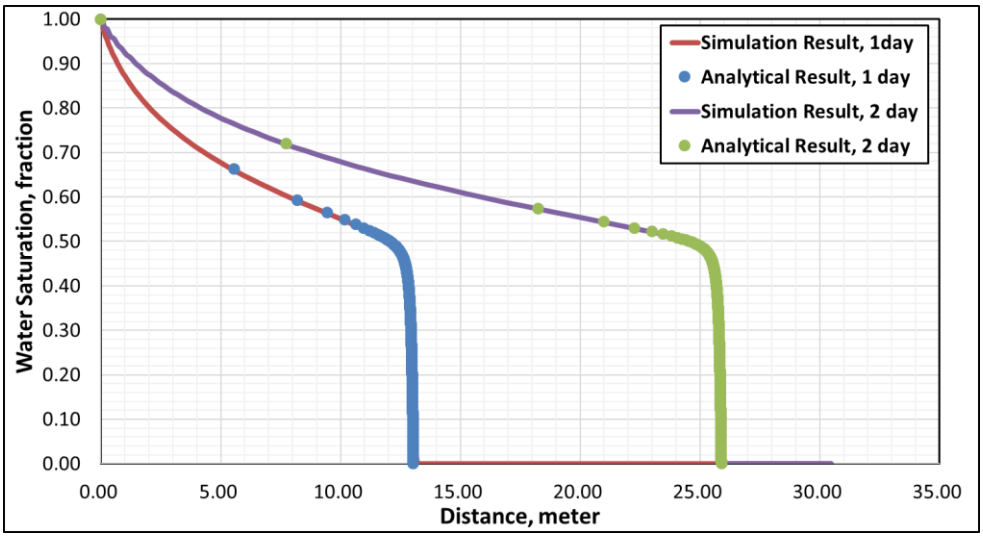

Figure 2.4 Analytical model and simulation (N=10,000) results comparison for q=1 RB/day

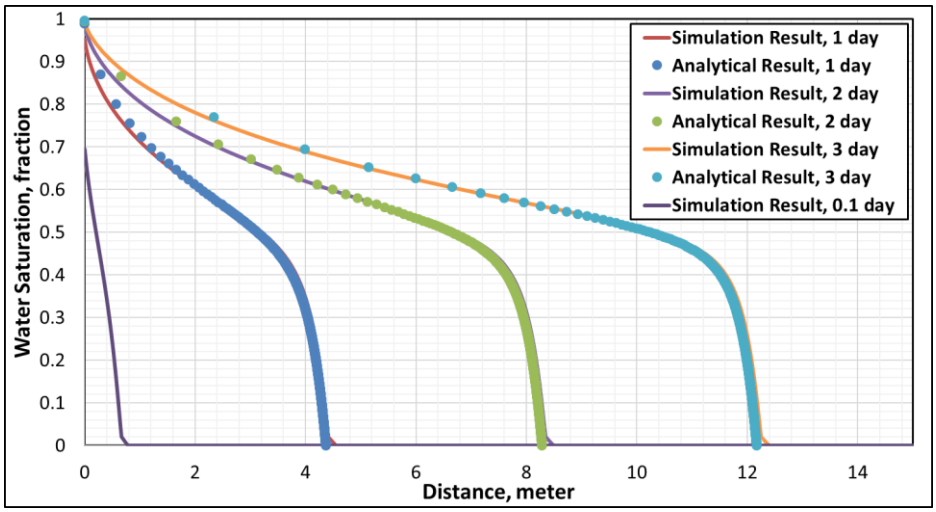

Figure 2.5 Analytical model and simulation (N=10,000) results comparison for q=0.3 RB/day

From the above graphs, it's clear that the results from the analytical model are in excellent agreement with the results from flow simulation. This verifies the validity of the analytical model. Another observation that can be made from the above comparison is that at the front of the saturation profile, the simulation results have a slight incremental spread compared to the analytical results. This is due to the numerical dispersion of the finite difference equation. One case of early time flow is shown as the purple curve in Figure 2.5, without an analytic solution. This corresponds to the case when the analytic solution would exceed the solution limits, as it is capillary dominated at early time. For this early time, the value of the dimensionless group is larger than the maximum value required in order to construct the asymptotic solutions. The details regarding the mass balance closure and monotonicity requirement are shown in Appendix A.

The above results with 10,000 grids have shown excellent agreement between the analytical solution and the numerical simulation. To better understand the accuracy of the analytical solution, we have performed a convergence calculation and compared the solution against coarser simulation models. Figure 2.6a shows the saturation profiles from different simulation grid sizes for the 2-day case in Figure 2.4, as well as our analytic solution and the B-L solution without capillarity. Figure 2.6b shows the corresponding convergence results represented by the root mean square of the error, with the reference case being the finest simulation result with 100,000 grid blocks. The results show first-order convergence for the simulation results. The RMS error shows that the matched asymptotic expansions solution has comparable accuracy to a simulation with slightly in excess of 1000 grid blocks. The error analysis also shows the improved accuracy compared to the B-L solution without capillarity.

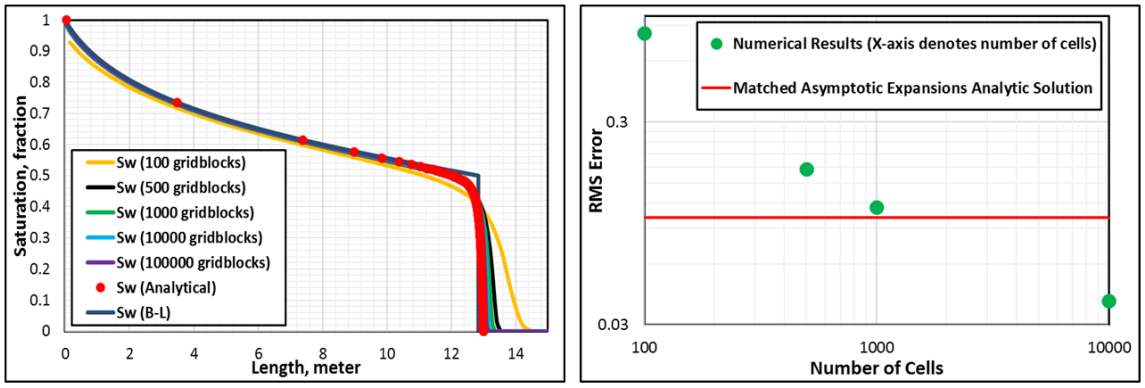

Figure 2.6 (a)-Comparison of the results from numerical simulations with different grid sizes with the result from the analytic solution and B-L solution; (b)-RMS error convergence result

2.3 Discussion

In this section, we will show some example calculations using our approach for simple geometries of linear and radial flow. The results from the example calculations as well as the related discussion will illustrate the subtlety of our approach, the dimensionless variable ε_D, and the corresponding physics behind them. The input parameters are the same as shown in Table 2.1.

2.3.1 Linear Flow Results

The first example we show is for linear flow. Figure 2.7a and Figure 2.7b show the resulting composite saturation profile and fractional flow relationships as functions of time. Table 2.2 summarizes the corresponding ε_D and ε calculations as functions of time (or T).

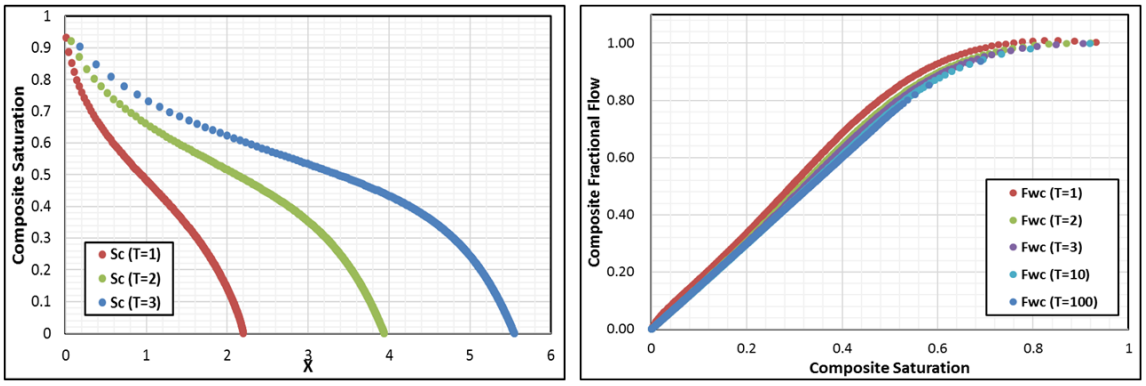

Figure 2.7 (a)-Composite saturation profile for linear flow; (b)-fractional flow plot for linear flow

	T	1	2	3	10	100
Linear Flow	ε_D	0.7796	0.3898	0.2599	0.0780	0.0078
	ε	0.7796	0.7796	0.7796	0.7796	0.7796

Table 2.2 Parameters calculated from the linear flow examples

We can see that for linear flow case with simple geometry, homogeneous properties, and fixed flow rate, that ε is independent of time, and the width of the capillary transition at the front remains constant. However, the dimensionless group $\varepsilon_D = \varepsilon\left(x(t)\right)/qT$ will decrease with time, implying that the saturation profile will approach the Buckley-Leverett solution at large time, irrespective of the strength of capillarity. This is also apparent in the fractional flow plot, where the concave envelope is obtained in the large time limit. We will return to this point after examining the radial flow solution.

2.3.2 Radial Flow Results

We now perform the identical calculation to the radial flow case. Figure 2.8a and Figure 2.8b show the resulting composite saturation profile and fractional flow relationships for radial flow test case at increasing times, again at a fixed injection rate. Table 2.3 summarizes the corresponding ε_D and ε calculations as functions of time (or T) for the radial flow case.

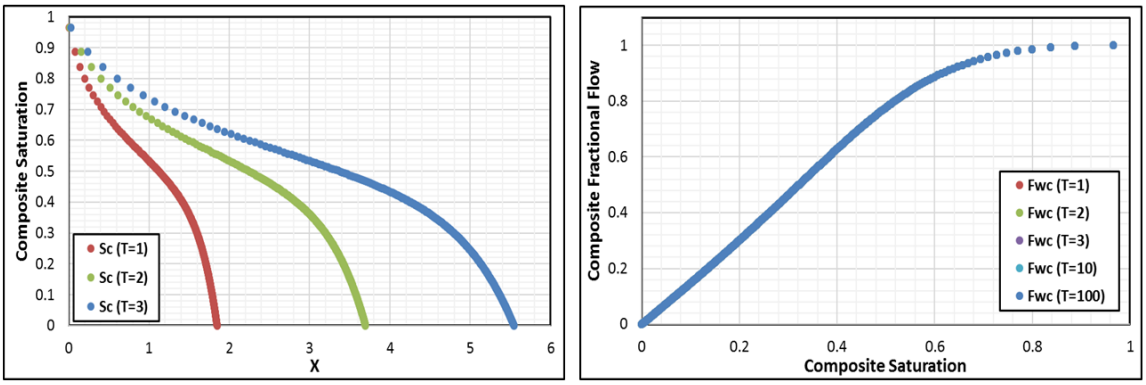

Figure 2.8 (a)-Composite saturation profile for radial flow; (b)-fractional flow plot for radial flow

	T	1	2	3	10	100
Radial Flow	ε_D	0.2589	0.2589	0.2589	0.2589	0.2589
	ε	0.2589	0.5178	0.7767	2.5890	25.8898

Table 2.3 Parameters calculated from the radial flow examples

In contrast from the result of linear flow, in the radial flow cases, ε increases linearly with X but the dimensionless group ε_D is now independent of T and the width of the capillary transition zone increases with time. Additionally, the fractional flow does not change with time, i.e., it does not converge to the concave envelope at large time.

2.3.3 Dimensionless Capillary Group

Notice that, for both cases shown above, the composite saturation profile now experiences a smooth transition at the front compared to the shock front constructed from the traditional Buckley-Leverett method. The length scale of the solution in the vicinity of the shock and its change with time is characterized by the small parameter ε or its

dimensionless form ε_D. The change of these two parameters along with time for both linear and radial flows are shown in Table 2.2 and Table 2.3.

The results imply that the dimensionless group ε_D, scales inversely with injected volume for linear flow and thus the composite solution reduces to the Buckley-Leverett solution at late time, irrespective of the strength of capillarity. For linear flow at early time, the dimensionless group will increase beyond the range for which the capillary correction solution is possible, indicating capillary dominance. In contrast, for radial flow, the dimensionless group does not depend upon time and the impact of capillarity does not change with time. Figure 2.9 shows the relationship of the composite saturation profile vs. X/T for both linear flow cases and radial flow cases.

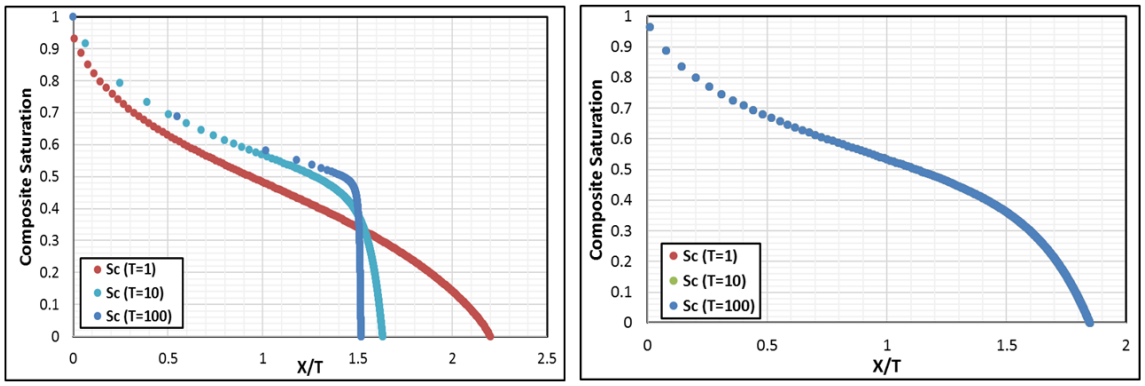

Figure 2.9 (a)-Composite saturation profile vs. X/T plots for linear flow; (b)-composite saturation profile vs. X/T plots for radial flow

The saturation profiles from Fig. 7 display the impact of the dimensionless group ε_D. For linear flow the dimensionless group scales inversely with injected volume so the saturation front shrinks when T increases. On the contrary, for radial flow, ε_D does not depend on the volume injected and thus the saturation profile does not change with time.

Unlike the capillary number which describes the relative magnitude of these forces at the pore scale (Steigemeir 1977), our dimensionless group describes this quantity at the field scale. We will return to the use of an identical dimensionless group when discussing spontaneous imbibition. Another well-known scaling group is given by Rapoport and Leas (1953). They defined a scaling group of $lu_T\mu_w$ where l denotes the total length of the system. Thus, this is more related to the negligibility of capillary end effect when we are performing unsteady state experiments. The comparison with Rapoport and Leas scaling group will be further discussed in the capillary end effect section.

2.4 Application

2.4.1 Capillary End Effect

Another problem in which capillary corrections arise is at the outlet of a laboratory coreflood (Heaviside and Black 1983). The outlet boundary condition, $p_c(S)=0$, follows from phase pressure continuity for each of the two phases. If capillarity is neglected, then no additional boundary condition arises. However, with the inclusion of capillarity in the description, the outlet saturation is fixed to a value $S=S_c$ for which $p_c(S_c)=0$. Instead of a moving shock, we now have a stationary boundary layer at the outlet, $X=L$.

$$\xi=\frac{X-L}{\sigma} \tag{2.38}$$

The development of the solution is similar to the above, although simplified now since $c=0$. The inner limit of the outer solution is the Buckley-Leverett saturation at the

outlet: $L = T \cdot F_w'\left(S^m\right)$, so now the match saturation is a function of T. The first integral of the inner solution must match the water phase influx.

$$f_w = F_w\left(S^I\right) - \frac{\varepsilon}{\sigma q} G\left(S^I\right)\frac{\partial S^I}{\partial \xi} = F_w\left(S^I\right) - \frac{\varepsilon}{q} G\left(S^I\right)\frac{\partial S^I}{\partial X} = F_w\left(S^m\right) \tag{2.39}$$

$$L - X = \left(\frac{\varepsilon(l)}{q}\right) \cdot \int_{S_c}^{S^I} \frac{G(S)}{F_w\left(S^m\right) - F_w(S)} dS \tag{2.40}$$

Unlike the moving boundary layer problem, there is no need for a mass balance constraint to close the equations.

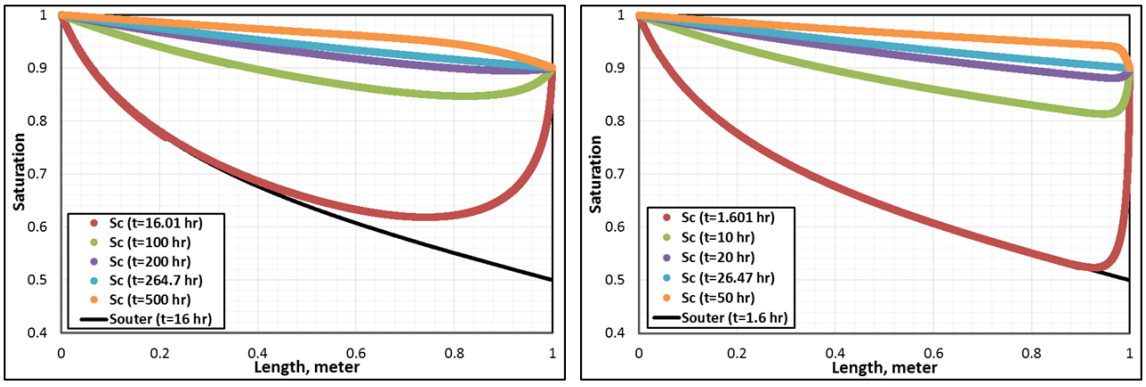

Figure 2.10 (a)-Capillary end effect for flow rate of 1PV/day; (b)-capillary end effect for flow rate of 10PV/day

The results are shown in Figure 2.10 for two different flow rates. The input parameters are the same as we have in Table 2.1, with the exception that $S_c = 0.9$. For reference, the Buckley-Leverett solution at the time of water breakthrough is shown. In both cases, a water bank arises at the core outlet. As the Buckley-Leverett outlet saturation increases, it will match and eventually exceed the outlet saturation. At high saturations, an

oil bank is retained within the core. The relative magnitudes of these two banks depend upon the wettability of the core.

The integrand of Eq (2.40) has a simple pole at $S = S^m$ which leads to a logarithmic saturation solution. Inverted as a profile this indicates that the inner saturation correction decays exponentially with distance away from the outlet, with a length scale inversely proportional to the flow rate. This is apparent when contrasting the solutions in Figure 2.10a and Figure 2.10b. If we apply this analysis at the field scale near a producing well, the flow rate is large over a small cross-sectional area, leading to a small dimensionless capillary parameter. Although there may be a saturation "bank" due to the reservoir wettability, the length over which this bank will form will be negligible. The mass balance integrand corresponding to Eq (2.40) has no pole, which indicates that the correction to the average saturation is $O\left(\frac{\varepsilon}{qL}\right)$, instead of the larger correction of $O\left(\frac{\varepsilon}{qT}\ln\frac{\varepsilon}{qT}\right)$ when the shock is still within the core.

We can evaluate the impact of the end effect on the laboratory determination of relative permeability using the unsteady state JBN method (Johnson et al. 1959). This analysis determines the relative permeabilities using the fractional flow, the saturation, and the pressure gradient, all referenced to the core outlet. Our analysis indicates that the end effect has no impact on the outlet fractional flow itself since $f_w = F_w\left(S^m\right)$ for the inner solution. However, the outlet saturation is determined from the average saturation, which does include the impact of capillarity. The mobility function is determined from the

outlet pressure gradient which itself is determined from the total pressure drop across the core, and is impacted by capillarity. Based on the asymptotic analysis, we expect the error introduced into the inferred outlet pressure gradient to be larger than that introduced into the outlet saturation, leading to an overall suppression of the total mobility.

The neglect of the capillary end effect has placed limitations on the displacement experiments' configurations. One major limitation is the requirement of high flow rates during the experiment. This means that in order to use the JBN method, the displacement experiments, more than likely, have to be conducted at flow rates higher than the true reservoir conditions. These high flow rates might also cause instability in the displacement itself as well as fines migration problems (Chuoke et al. 1959; Qadeer et al. 1988). Unsteady state laboratory procedures often involve a "high speed bump" at the end of a laboratory test to reduce the length of the core which is impacted by capillarity, where an increase in flow rate by a factor of 10 decreases the length scale of the capillary correction by a corresponding amount.

To quantify this limitation, Rapoport and Leas (1953), as well as Kyte and Rapoport (1958), have used a scaling coefficient $lu_T\mu_w$ to develop criteria for neglecting capillary end effect. This scaling group is the quantity required to reach stabilized flooding behavior. But they also indicated that a more general scaling factor should be the dimensionless group $kp_T/lu_T\mu_w$, where p_T is the pre-factor $\sigma\sqrt{\phi/k}$ in the Leverett-J function. So, their general dimensionless group is very close to $\varepsilon(l)/qL$ in our approach, except for the representation of the viscosity term. This means the overall analysis is

consistent with each other. We consider the critical value of the scaling coefficient $lu_T\mu_w$ to be around 0.5 to 3.5 $\mathrm{cm}^2 \cdot \mathrm{cp}/\mathrm{min}$ according to the values reported by Rapoport and Leas (1953) and the parameters in Table 2.1 being used. This corresponds $\varepsilon_D = \varepsilon(l)/qL$ equals 0.17 to 1.19. Further consider the dimensionless parameter $\varepsilon(l)G(S^*)/qL$, the critical values for it would be in the range of 0.06 to 0.45. One important difference lies in the time-dependence of the capillarity's impact. If we consider the moving boundary problem, the time-dependence lies in $\varepsilon(L(T))$, thus the current dimensionless parameter captures variations in rate. This is shown in the analysis of the dimensionless parameter above. For the stationary boundary problem (capillary end effect), the time-dependence lies in the integral of Eq (2.40) which is actually the matched saturation's change with time.

To further investigate the application of the derived analytical solution with capillary end effect, we have applied the method to interpret relative permeability curves from unsteady state experiment data. The determination of relative permeability is down through matching the production and pressure data from the experiment with the analytic model's prediction. The information of capillarity is assumed to be known, as the determination of capillary pressure is not within the scope of this research. The experiment data of the unsteady state experiment used here was cited from Richmond and Watsons (1990). The experiment is water displacing oil in an oil-wet core sample, thus it is a drainage process. The core is 7.13 cm in length and the cross-sectional area is 11.3 cm^2.

The porosity is 26.2% with a permeability of 9.6 mD. All other parameters associated with the experiment can be found in the original paper. The actual experimental data of pressure drop and production were provided from the lab and the original paper had used numerical simulation and inversion to calculate the capillary pressure and relative permeability simultaneously. As the first step of our analysis, we have used the Leverett-J function as shown in the following to match the capillary pressure data given in the paper. The resulting parameter values for the Leverett-J function is shown in Eq (2.42) and Figure 2.11 shows the match between the modeled capillary pressure and the data provided.

$$p_c = \sigma\sqrt{\frac{\phi}{k}} * J \tag{2.41}$$

$$J = -0.02544 * \exp(4.011S) + 0.02544 \tag{2.42}$$

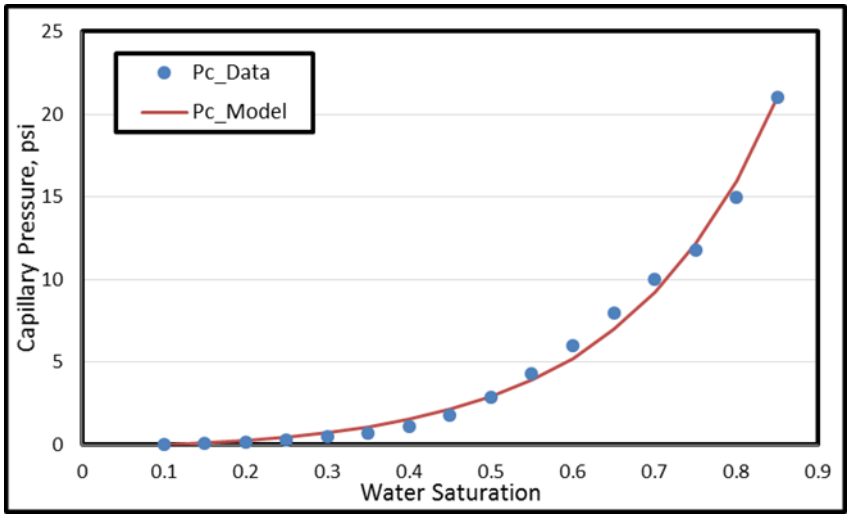

Figure 2.11 Capillary pressure match between the analytic model and the data

After getting the functional form for the capillary pressure, we would then assume the functional form for the relative permeability that will be applied to the analytic solution.

The equations for both the oil and water phases are shown in the following two equations, respectively.

$$\frac{k_{ro}}{\mu_o} = \frac{(1-S)^m}{\mu_o} \tag{2.43}$$

$$\frac{k_{rw}}{\mu_w} = \frac{MS^n}{\mu_o} \tag{2.44}$$

The initial guesses for M, n and m are all 2 and the match of pressure and production data is done through non-linear regression. The objective function for the regression is shown as the following:

$$\min \quad O = \frac{\text{norm}(p_{predict} - p_{data})}{\text{std}(p_{data})} + \frac{\text{norm}(N_{predict} - N_{data})}{\text{std}(N_{data})} \tag{2.45}$$

The converged M, n and m values are 2.5159, 3.9746 and 2.8501, respectively. Figure 2.12a and Figure 2.12b show the results after the regression for the pressure and production match between model prediction and the data. From the two figures of the matching results we can see that the overall match is pretty good for both the pressure drop and oil production.

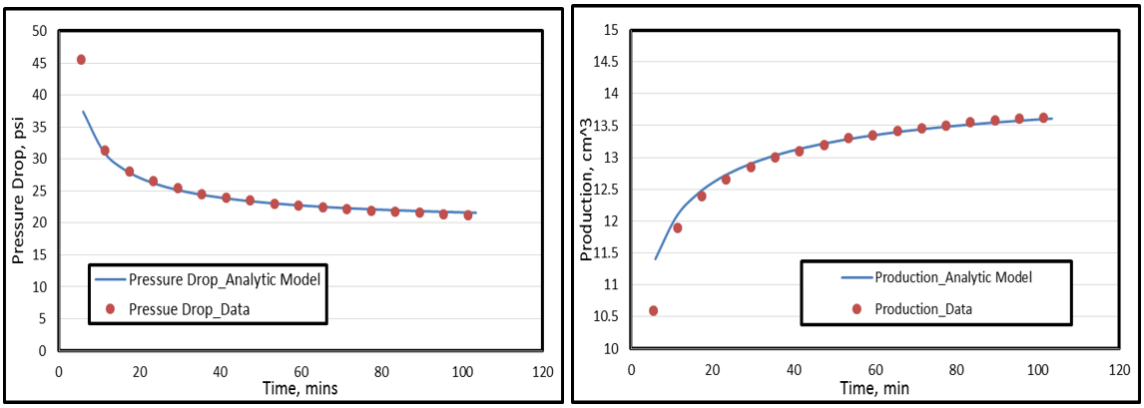

Figure 2.12 (a)-Pressure drop match between the model prediction after inversion and the data provided;(b)-production match between the model prediction after inversion and the data provided

By plugging in the M, n and m values into the corresponding defined functional forms, we will get the resulting relative permeability curves from the inversion. These curves are compared against the traditional calculation from JBN method as well as the data provided in the original paper as shown in Figure 2.13. The results showed that the relative permeability calculated from the inversion of our analytic model is in close agreement with the numerical inversion result given in the paper. The result also showed that the relative permeability calculated from JBN method deviated from the "actual" value. This is obvious if we focus on the water phase relative permeability as the JBN calculation is lower than both the analytic model's inversion and numerical inversion from the paper.

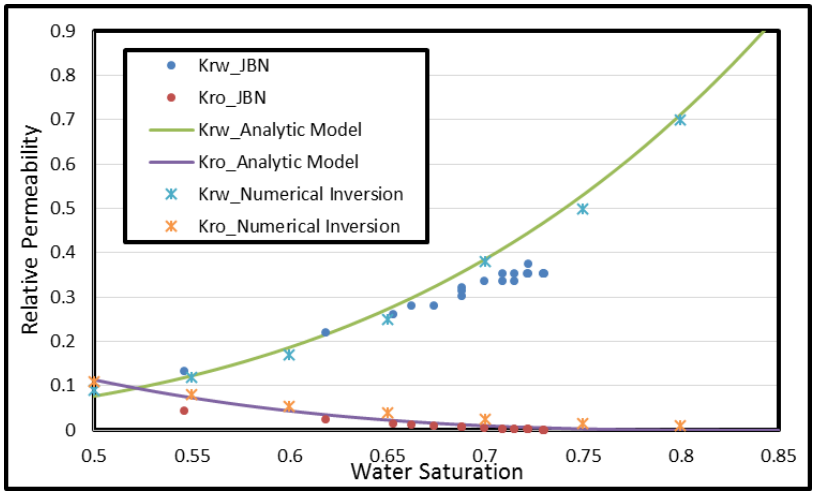

Figure 2.13 Relative permeability comparison between analytic inversion, JBN calculation and data given (numerical inversion)

To better show the comparison result, we have plotted the total mobility from the analytic solution's inversion with the JBN calculation, as shown in Figure 2.14a. From Figure 2.14a, we observe an overall compression of the total mobility due to the existence of capillary end effect. Also, in Figure 2.14b, we have shown the outlet fractional flow calculated using JBN method along with the fractional water mobility. It shows that in the context of ignoring capillarity, the JBN methods gives a different representation of the water phase fractional flow. Again, in this case study, we have used a pre-determined functional form of relative permeability, but it is not required to use this specific form.

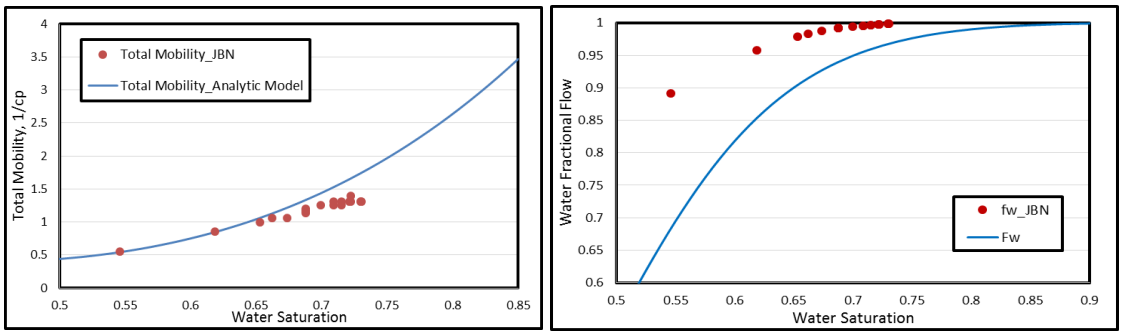

Figure 2.14 (a)-Total mobility comparison between analytic inversion and JBN calculation; (b)-comparison of fractional flow calculated from JBN method with fractional water mobility

2.4.2 Capillary Pressure and Relative Permeability Calibration before Water Breakthrough

Another application of the methodology is the estimation of capillary pressure and relative permeability information from saturation profiles before water breakthrough. The shape of the composite saturation profile around the shock front depends upon the capillary pressure function, so in principle we can calibrate the capillary pressure function if the saturation profile is determined experimentally. We have already cited the early work by Terwilliger et al. (1951) in which electrical resistivity measurements were used to determine the saturation profile in a sand column for gas displacing brine. More recent researchers have introduced other core flood saturation monitoring techniques, most notably gamma attenuation measurements and X-Ray CT (Nicholls and Heaviside 1988; Wellington and Vinegar 1987).

As a demonstration, we will analyze Terwilliger's published experimental data to infer the capillary pressure and relative permeability functions and compare them with the

data reported by Terwilliger. Some of the key parameters for these experiments are summarized in the following table:

μ_w(cp)	0.826	k(mD)	2700	ϕ	0.33
ρ_w(g/cm^3)	1.006	S_{gi}	0	S_{wrg}	0.18

Table 2.4 Input parameters for capillary pressure function calibration (following Terwilliger et.al. 1951)

The flow direction in the experiment of Terwilliger is strictly vertical with downwards flow at a fixed flow rate. In this case the outer solution will have a self-similar solution based upon a fractional gas flow which includes the effect of gravity.

$$F_g(S) = \frac{\lambda_g}{\lambda_T} - \frac{A\Delta\rho g}{q}\frac{\lambda_g\lambda_w}{\lambda_T} \tag{2.46}$$

In this application, the ultimate goal for the calibration is to match the composite saturation profiles with the experimental data. However, since the matched asymptotic expansion method was used, and saturation correction at the inlet was introduced to obtain the mass balance closure, there may exist some deviation of the saturation profile away from the shock comparing with its original B-L solution. In order to capture both the behavior of composite saturation profile (combined impact from capillary pressure and relative permeability) and B-L profile away from the shock (impact from relative permeability), we would like to use a Pareto-based approach for multiobjective optimization. In this typical case, we have chosen to use multiobjective genetic algorithm as the tool for optimization.

The outer solution determines the bulk of the saturation profile away from the saturation shock and is controlled by gravity and viscous forces. The capillary force only

impacts the solution in the vicinity of the saturation shock, and leads to a steady state solution. Thus, a time-lapse saturation profile, or equivalently the speed of saturation evolution, would essentially be represented by the concave envelope of the fractional flow curve. So we will construct our first objective to be the mismatch between time-lapse model prediction and the time-lapse saturation profile data from the experiment. Due to the steady state behavior of the inner solution in the vicinity of the shock, the time-lapse calculation will essentially exclude the impact from capillarity and can be totally represented by the outer solution.

And the second objective here will be the mismatch between model predicted composite saturation profile and one recorded saturation data. This objective function is controlled by both capillary pressure and relative permeability, but is subject to the inlet saturation correction we have introduced with our analytic solution. And the chosen saturation profile data is the one with larger injection time due to the limit of the analytic solutions' applicability for small capillary effect.

For this calculation, we will utilize simple relative permeability and capillary pressure functions with a few parameters.

$$\frac{k_{rw}}{\mu_w} = \frac{(1-S)^n}{\mu_w} \tag{2.47}$$

$$\frac{k_{rg}}{\mu_g} = \frac{MS^m}{\mu_w} \tag{2.48}$$

$$p_c = \sigma\sqrt{\frac{\phi}{k}}J(S) \; and \; \frac{dJ}{dS} = J_c(1-S)^{\beta} \tag{2.49}$$

In the above equations, the unknowns that are subject to change during the matching process include exponents n and m for the relative permeability function and J_c and β for capillary pressure derivatives. The two-phase mobility ratio M is kept as a constant as normally we would know this value from the experiments. The M value is inferred from the experimental data to be 23.58 according to the viscosity ratio of the two phases as well as the end-point characteristics of the relative permeability. So, we will be using $M = 23.58$ for our analysis here.

We will use one set of experimental data from Terwilliger's paper to demonstrate the application of this analytic model. The data we chose has a liquid flow rate of $1.538\ \mathrm{cm}^3/\mathrm{min}$. This is the largest flow rate reported in the original paper where the stabilized zone can be seen within the length of the experimental core. For a gravity-stable displacement, the shock saturations are normally high and there is relatively little Buckley-Leverett transition, which further reduces the sensitivity compared to horizontal flow. And this effect becomes larger when the flow rate is smaller. And this is the reason why we chose the largest flow rate case in our analysis.

Before going into the analysis, one other piece of information we need is the effective injected time. As only the relative times and injected volumes are provided in Terwilliger et.al (1951), and so a mass balance closure has been used to infer the volumes of fluid injected and the effective injected time to be used in our analysis. The resulting values are $t_{eff1} = 4.8894$ hr and $t_{eff2} = 8.2987$ hr.

To initialize the multiobjective genetic algorithm, we are using Latin Hypercube Sampling method to sample the initial population. The ranges for the four tuning parameters are shown in the following table. The population size we used here is 100, and the maximum generation number is 30.

Parameters	n	m	J_c	β
Minimum	1.5	1	0.00001	-1
Maximum	5	10	1	-10

Table 2.5 Parameters' range used for calibration

After 30 generations of multiobjective genetic algorithm, the last population's scores as well as the rank 1 to rank 3 Pareto front points are shown in the following figure.

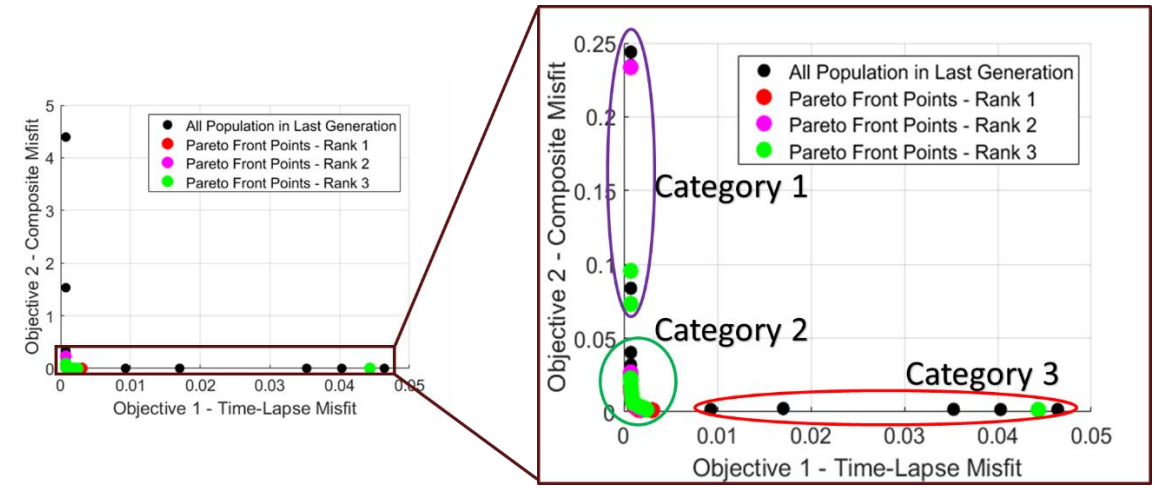

Figure 2.15 Calculated objective functions' values and Pareto front points

From the above figure, we could calculate the Pareto front points as shown in red, magnet and green based on different ranks. For the rank 1 to rank 3 Pareto front points, they could be grouped into three different groups as circled with different colors shown in the above figure as well. The point circled in magnet, to be referred to as Category 1, is the case where there exists the least misfit in the time-lapse profile matching. The points circled in green, to be referred to as Category 2, represents the optimal trade-off points between the two objective functions. The points circled in red, to be referred to as Category 3, are the ones with least misfit in composite profile matching. In the following part, we will show a detailed discussion about each one of these three categories.

We are using the blue dot as shown in the following figure as an example for the Category 1 Pareto front point (from rank 2).

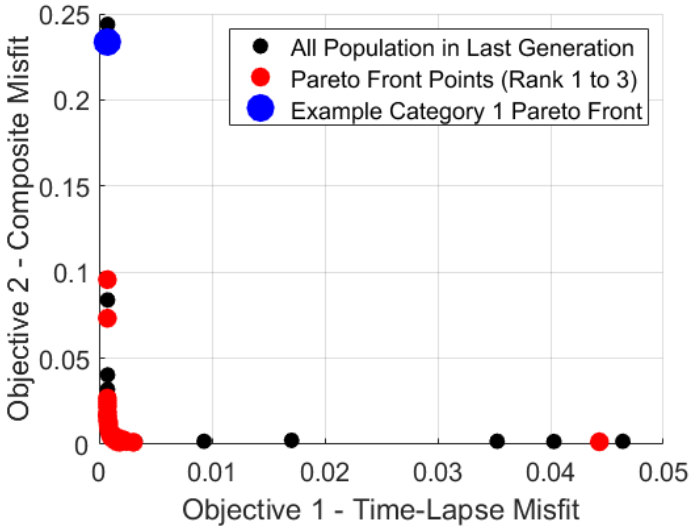

Figure 2.16 Example Pareto front point – Category 1

The tuning parameters associated with this Pareto front point are $n = 3.0309$, $m = 7.9794$, $J_c = 0.4050$ and $\beta = -6.0418$. The following figures show both the composite saturation profile and time-lapse saturation profile given by the analytic solution by using this parameters combination.

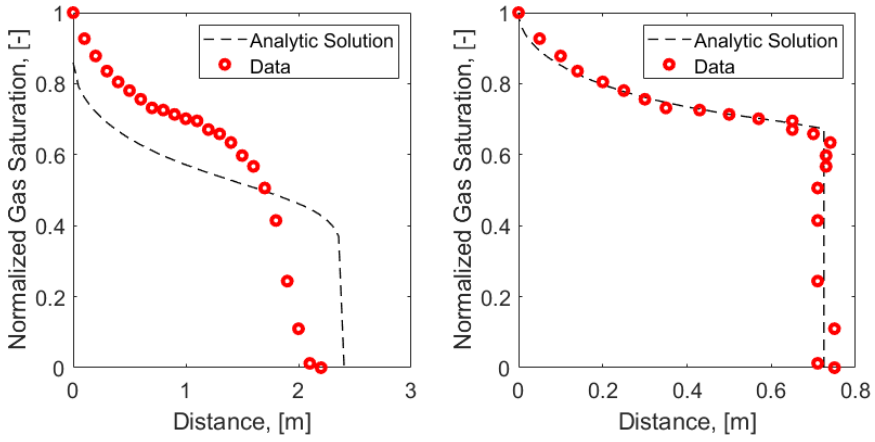

Figure 2.17 (a)-Composite saturation profile match using selected Category 1 parameter combinations; (b)-time-lapse saturation profile match using selected Category 1 parameter combinations

As we can see from the above figure, the time-lapse saturation profile has been fitted nicely, but the composite saturation profile still has a large mismatch comparing with the experimental data. We can further compare the F_g given by the relative permeability and capillary pressure, its corresponding concave envelope, and the F_g concave envelope given by the experimental data.

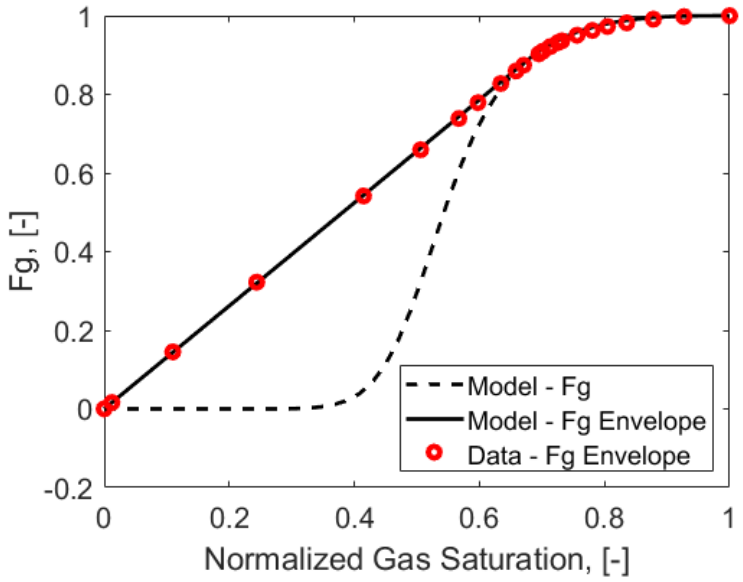

Figure 2.18 Fractional flow, its concave envelope and data derived concave envelope match using parameter combinations from Category 1

As a result of the good match between the time-lapsed model prediction and data, the F_g envelope is nicely captured. For this category of Pareto front points, the information from fractional flow envelope is nicely captured through the time-lapse match. However, since the composite saturation profile is not matched, the capillary pressure information is not very well represented, and it will, in turn, affect the interpreted relative

permeability information as they interact with each other. And also, this type of solutions will not show if we were focused only on the objective function of the composite saturation profile match.

The next category we are analyzing here is Category 2. We are using the blue dot showing in the following figure as an example for the Category 2 Pareto front points (from rank 1).

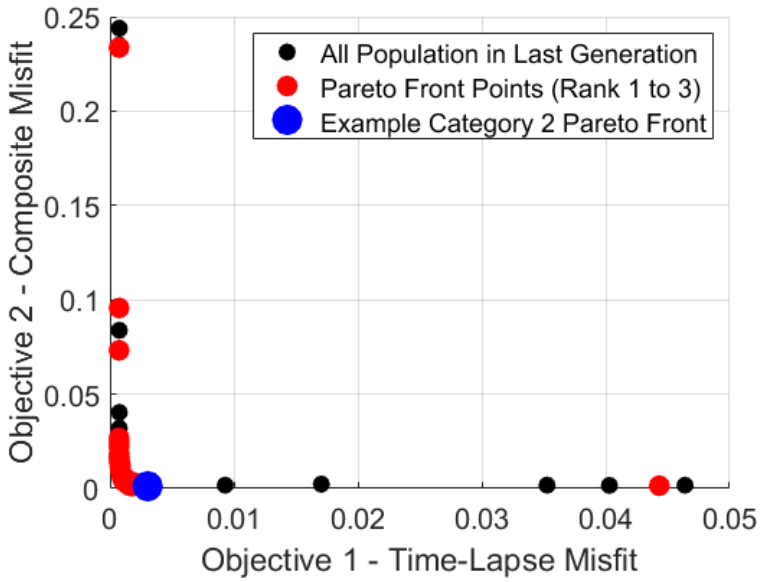

Figure 2.19 Example Pareto front point – Category 2

The tuning parameters associated with this Pareto front point are $n = 2.8417$, $m = 2.6979$, $J_c = 0.0498$ and $\beta = -1.5585$. The following figures show both the composite saturation profile and time-lapse saturation profile given by the analytic solution by using this parameters combination.

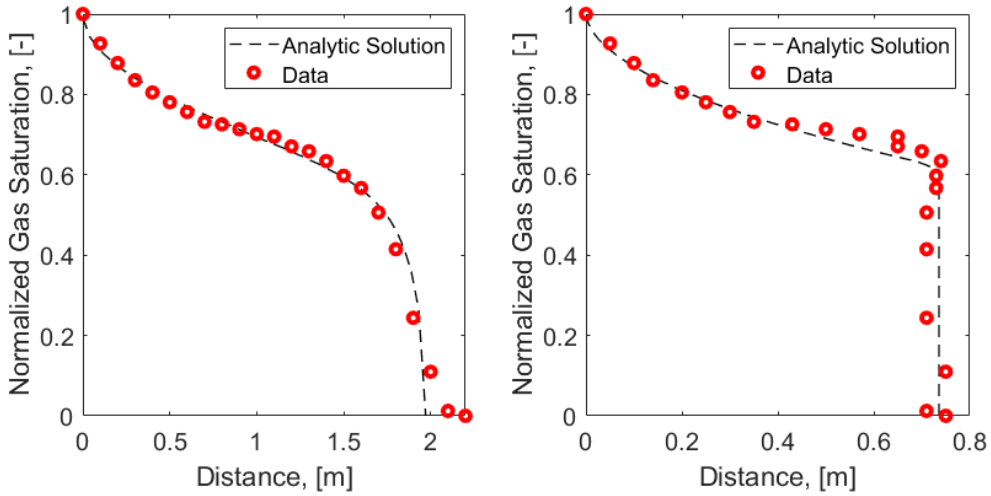

Figure 2.20 (a)-Composite saturation profile match using selected Category 2 parameter combinations; (b)-time-lapse saturation profile match using selected Category 2 parameter combinations

From the above Figure 2.20, we can observe that both composite saturation profile and time-lapse saturation profile are relatively nicely captured by the analytic model's prediction. And the following figure will also show that the concave envelope of the fractional flow is relatively well represented.

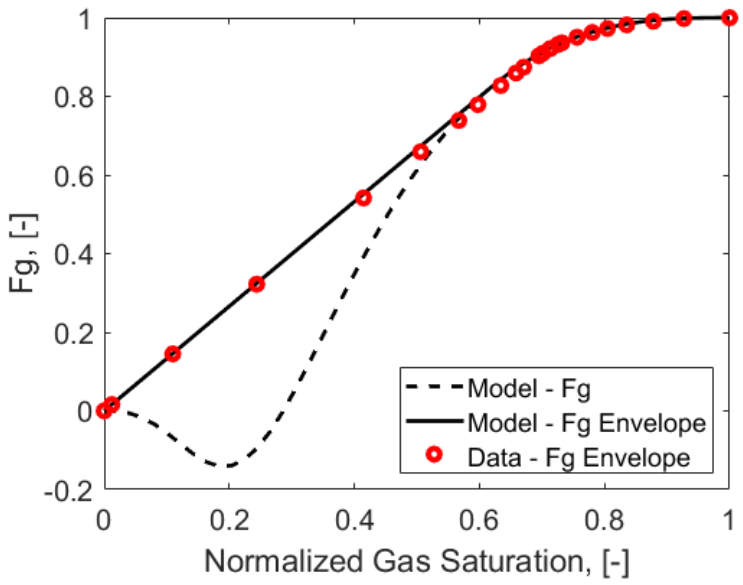

Figure 2.21 Fractional flow, its concave envelope and data derived concave envelope match using parameter combinations from Category 2

For this Category 2 Pareto front points, as both the fractional flow concave envelope and the shape of the saturation profile in the vicinity of the shock are well represented, the resulting combination of relative permeability and capillary pressure information should be closer to the actual displacement condition.

The last type of Pareto front points is Category 3. The example Pareto front point chosen for illustration is shown in the following figure (from rank 3).

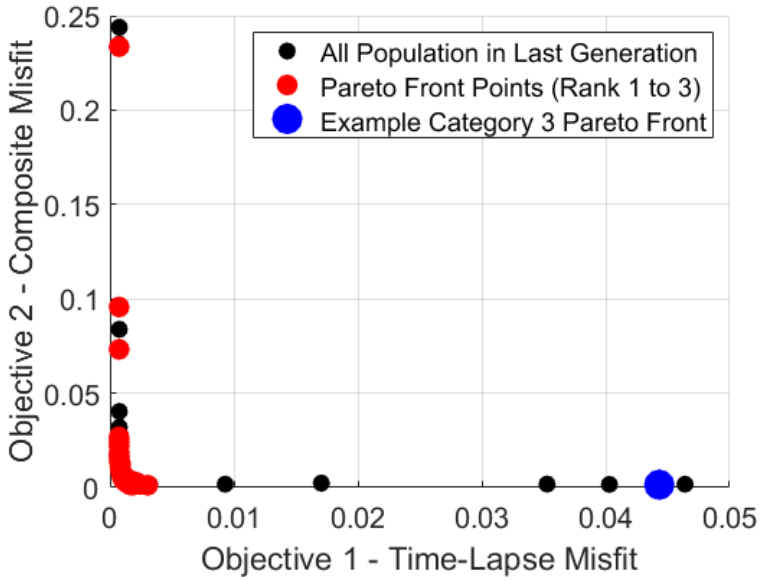

Figure 2.22 Example Pareto front point – Category 3

The tuning parameters associated with this Pareto front point are $n = 1.8805$, $m = 4.7353$, $J_c = 0.0388$ and $\beta = -3.2703$.

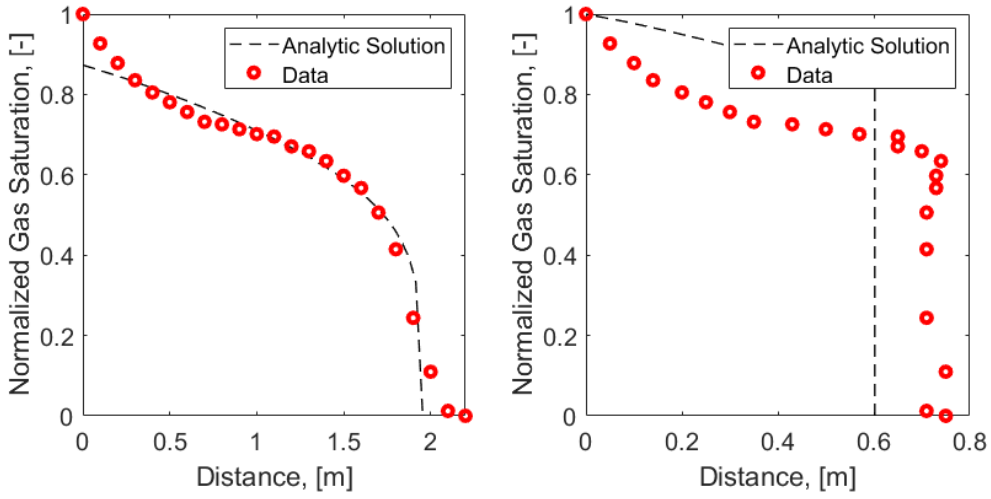

Figure 2.23 (a)-Composite saturation profile match using selected Category 3 parameter combinations; (b)-time-lapse saturation profile match using selected Category 3 parameter combinations

The above figure shows both composite saturation profile match and time-lapsed profile match from the Category 3 Pareto front point. We noticed that the parameters from this category, although stilling giving us a good match on the composite saturation profile, is not capturing the time-lapsed saturation profile's behavior. As a result of the bad match between the time-lapse model prediction and data, the fractional flow envelope is not captured at all.

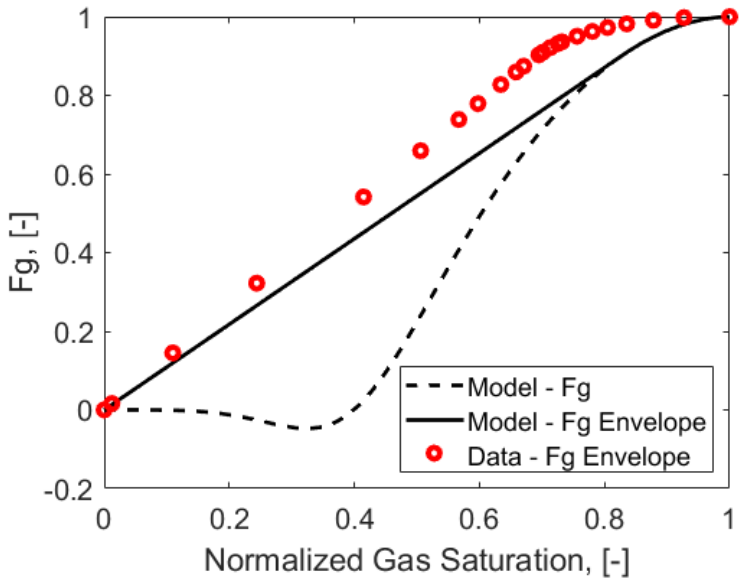

Figure 2.24 Fractional flow, its concave envelope and data derived concave envelope match using parameter combinations from Category 3

From the above results, we find that if we only use and calibrate from the composite saturation profiles, we may get results as shown in Category 3 where the fractional flow is off, and so will be the capillary pressure curves. The reason behind Category 3 is that the inlet saturation correction we are making for the mass balance closure. This will shift the portion of composite saturation profile away from the shock

down from the original B-L solution, and it will be severe once the dimensionless capillary group is larger. However, Category 1 will not show up as results as the composite saturation profiles are not matched. So, depending upon initial guesses, we may end up with a solution either in Category 2 or Category 3. But Category 2 is closer to the true solution respect to relative permeability and capillary pressure calibration. The following figure shows the comparison of capillary pressure from the Pareto front points' models and experimental data provided by Terwilliger et al. (1951). To be noted, since our analytic model only uses the derivative of capillary pressure when calculating the saturation profiles, all capillary pressure shown here are normalized such that the endpoint has zero capillary pressure.

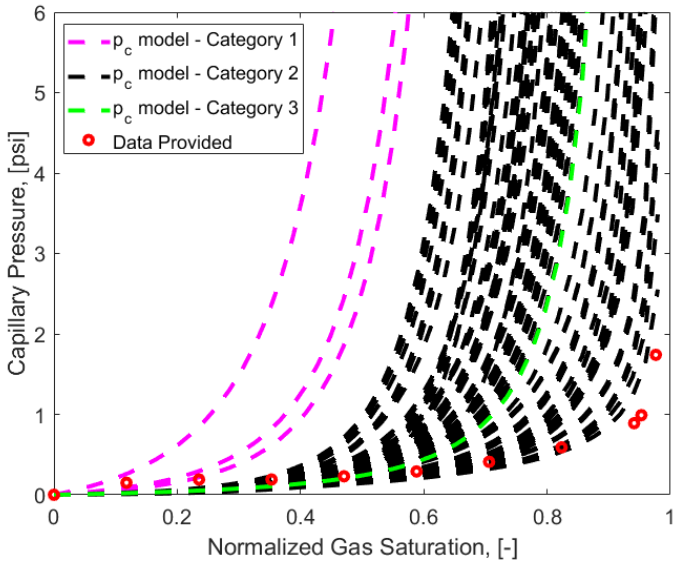

Figure 2.25 Capillary pressure comparison between different categories of Pareto front points and data provided by Terwilliger

As we can see from the above figure, the Category 2 Pareto front points result in a large range for the capillary pressure curves. But they did cover the capillary pressure data

provided in the original paper. For the other two categories, the capillary pressure calibration results seem to be a little far away from the given data points. We could further see the resulting relative permeability models given by the calibration process:

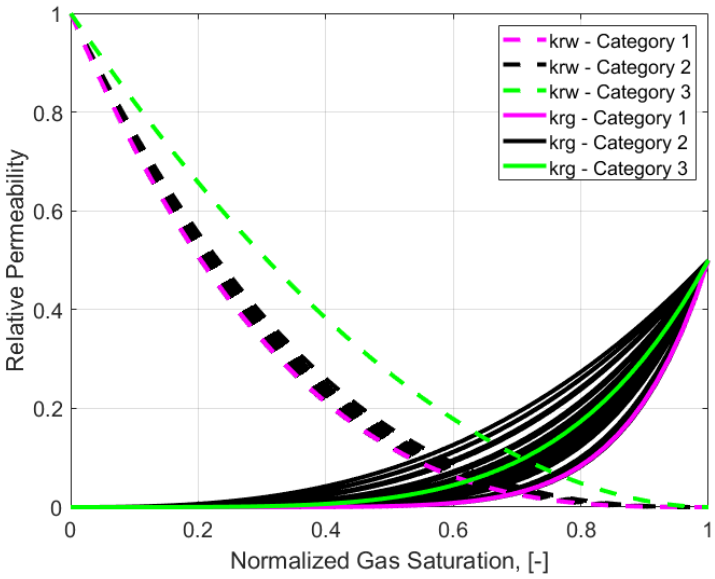

Figure 2.26 Relative permeability comparison between different categories of Pareto front points

From the above figure, we can still see that the calibration, even based only on Category 2, yields large uncertainty for the calibration results.

The last discussion for the Pareto-based optimization part is for the performance assessment of the multiobjective optimizers. The performance metric we are showing here is the dominated space which is a measure of how much of the objective space is weakly dominated by a given non-dominated set A (Lee et al. 2005). The following figure illustrates the calculation of dominated space:

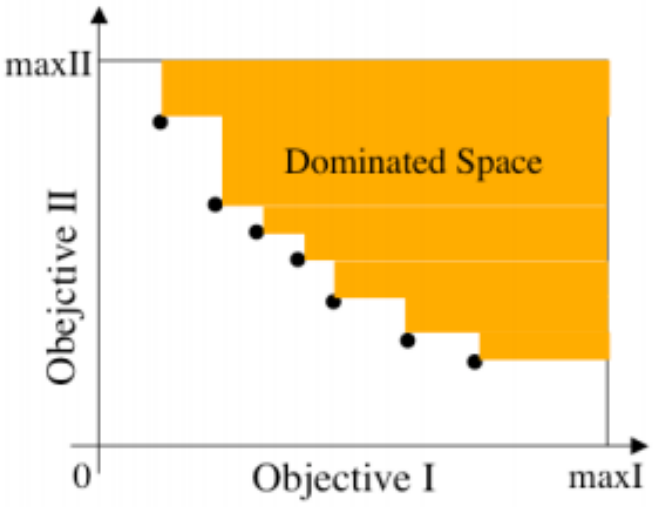

Figure 2.27 Dominated space (colored in orange) by a given Pareto set when two objectives are minimized (reprinted from Lee et al., 2005).

Basically, the dominated space should increase with increasing generation number as the algorithm exploring more Pareto spaces. The maxI and maxII shown in the above figure represent the reasonable maximum value for each objective. In our application, we have used the maximum values ever shown in all Pareto front points in all generations for each axis as the corresponding reference point. And the following figure shows the dominated space's change with respect to generations for our case.

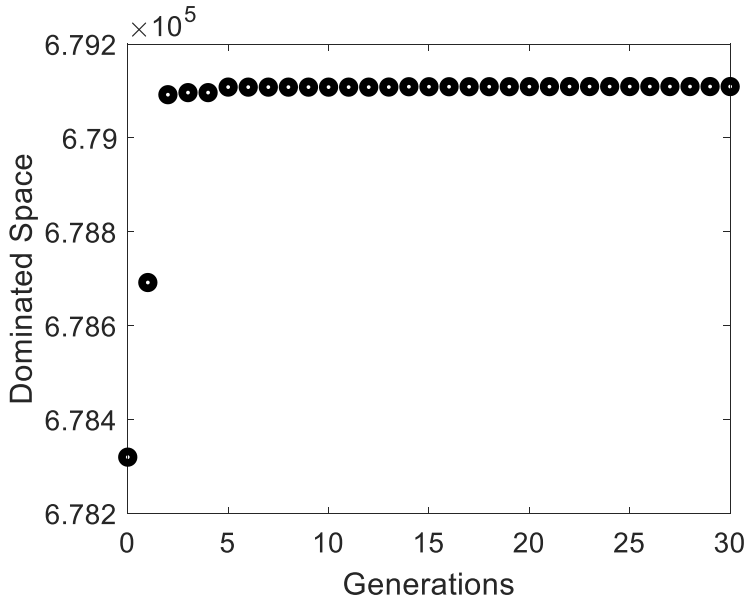

Figure 2.28 Dominated space behavior for multiobjective genetic algorithm

As we can see from the above result, the dominated space value stays fairly flat after the 6th generation. Thus, we argue that the 30 generation number is enough to quantify the correct Pareto front points, and the results from the last generation is a converged result considering the algorithm we are using here.

Instead of the above Pareto based approach, an alternative approach of calibrating the relative permeability and capillary pressure information is through a two-step calibration method. In this approach, we will first use the time-lapse saturation profile and the outer solution only to calibrate for the relative permeability information, and then use the calibrated relative permeability to match the composite saturation profiles by perturbing the parameters associated with capillary pressure. In the following section, we will show the example of this approach with the same dataset as we have just described.

First, we will perform the time-lapse saturation profile match. The following figure shows the root mean square error between the model predicted time-lapse saturation and the recorded data for the range of n and m values.

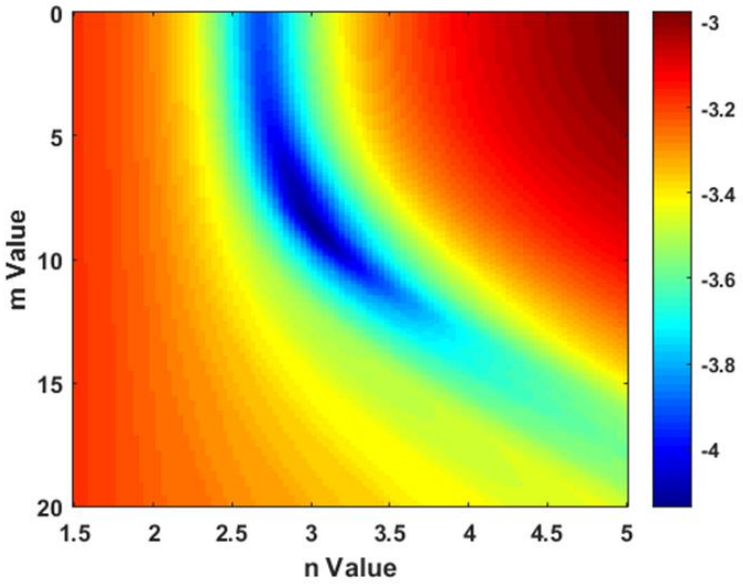

Figure 2.29 log10(RMS Error) plot between time-lapse model prediction and data for a range of m and n values

In the above figure, the lower the value represents the closer the fit is between the model prediction and data provided for a specific combination of n and m values. We can see that there are multiple combinations of the exponents that would yield identical time lapse saturation profile or Buckley-Leverett speed. We set the cutoff or tolerance value for the root mean square error at one standard deviation of the data $\log_{10}\left(\text{std}\left(X_{data}\right)\right) = -3.8258$. For all possible combinations of parameters that have an error less than this value, the m value is always less or equal to 12. So in the following analysis, we sampled 12 best-fit parameters for m from 1 to 12. The values of the

corresponding n and m values, time lapse saturation profile match and the fractional flow match plots are shown in Figure 2.30.

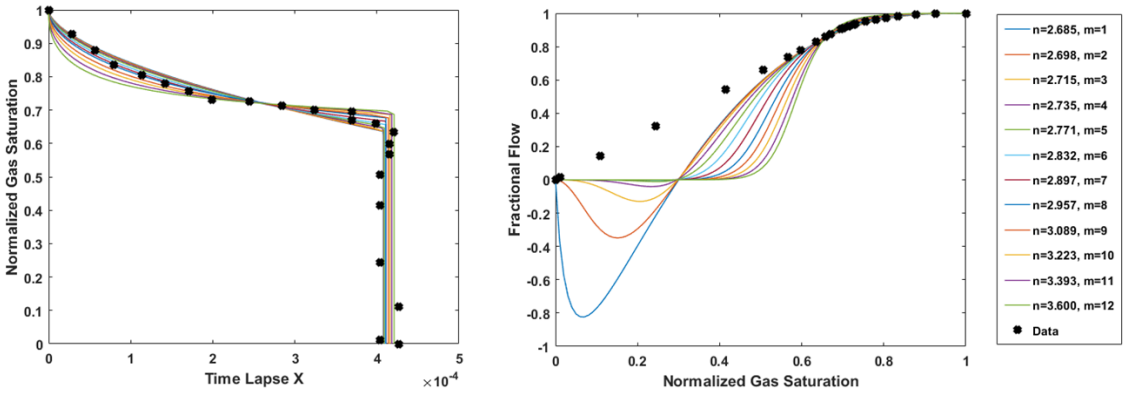

Figure 2.30 (a)-Time-lapse saturation profile match; (b)-fractional flow match

From the above figure, we can see that the time-lapse analysis here is to match the concave down envelope of the fractional flow curve and the resulting time-lapse profiles are very identical.

After determining the possible outer solutions from the time-lapse analysis, the inner solution including the effects of capillarity is used to determine the capillary pressure function by matching the experimental saturation profile with our composite solution. Here only the J_c and β parameters are the unknown variables since all other parameters are given by the experimental settings. We have first used a relatively wider range of J_c and β values and paired them with the previously determined relative permeability parameters and calculated the root mean square error as we did in the previous section. This results in 1188 different combinations and the following figure shows the root mean square contours.

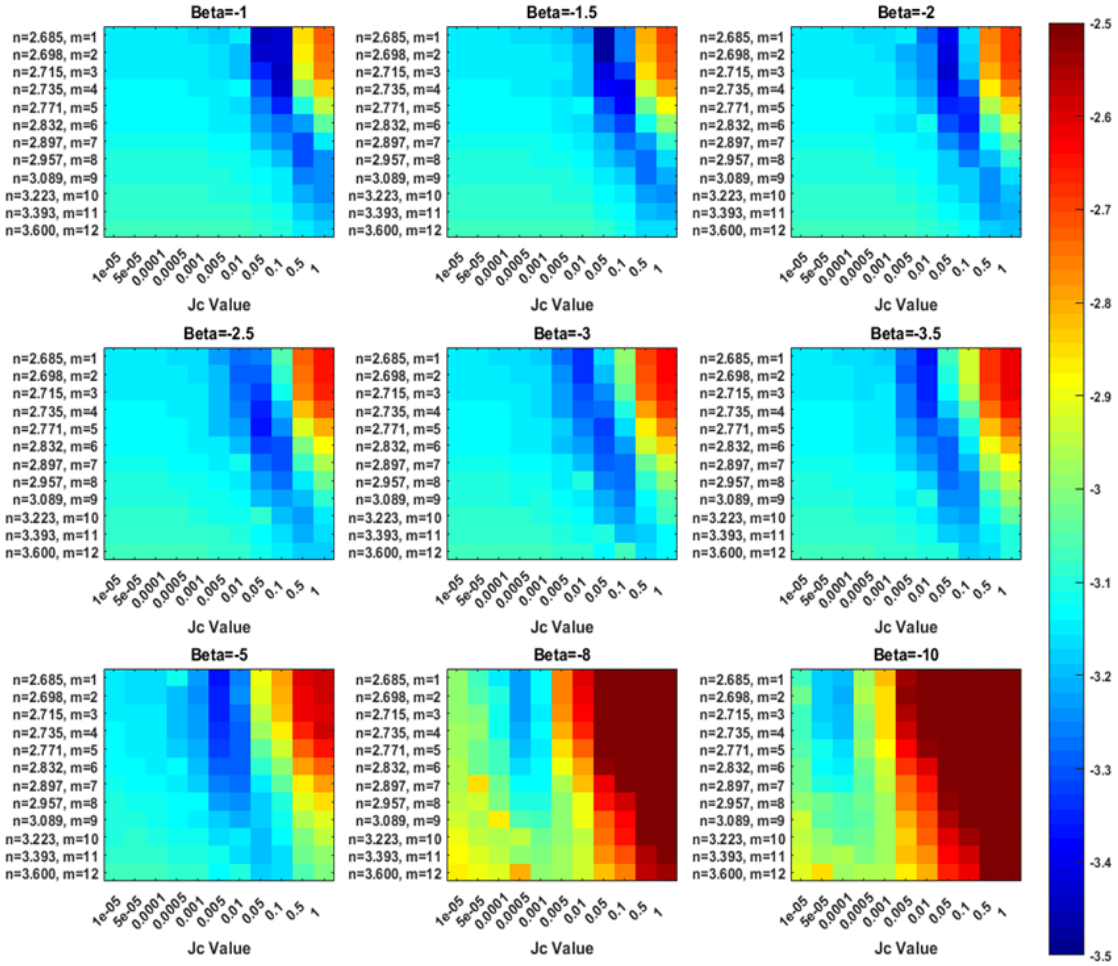

Figure 2.31 log10(RMS Error) plot between composite saturation model prediction and experimental data

The cut off value is again set up by examining the standard deviation of the data itself. The standard deviation is 3.8578E-4, thus the based ten log of this value is -3.4137. For all 1188 combinations, only 3 pairs of parameters meet this criterion and they are listed in the following table.

β	m	n	J_c
-1.0	3	2.714720	0.10
-1.5	1	2.685244	0.05
-1.5	2	2.698449	0.05

Table 2.6 Combinations of parameters yielding acceptable root mean square error

As these values are too sparse to represent the estimated range of the capillary pressure, the next step is to fine tuning on the existing parameter range. As our focus here is for the capillary pressure calibration, we will only tune in on the capillary pressure parameters J_c and β. But before going into the fine-tuning part, one thing we noticed here is that the composite saturation match actually back constrained the suitable parameters' range for relative permeability. From Figure 2.31, it is shown that no matter how the parameters from capillary pressure change, the only pairs of parameters from relative permeability (fractional flow) that yield acceptable errors are the ones with m value less than 4. This means that there is additional information for relative permeability from the saturation profiles that is not reflected in the time-lapse data. This is readily explained through our previous Pareto based approach as this additional piece of information would come from ruling out the points from Category 1 Pareto front points. Although we didn't test all the possible parameters with $m < 4$, it is still reasonable to argue that this is a good estimate range combined with Figure 2.29. Figure 2.32a is showing the range of parameters that combined both time-lapse data analysis and composite match analysis. And Figure 2.32b is showing the resulting range for the fractional flow curves.

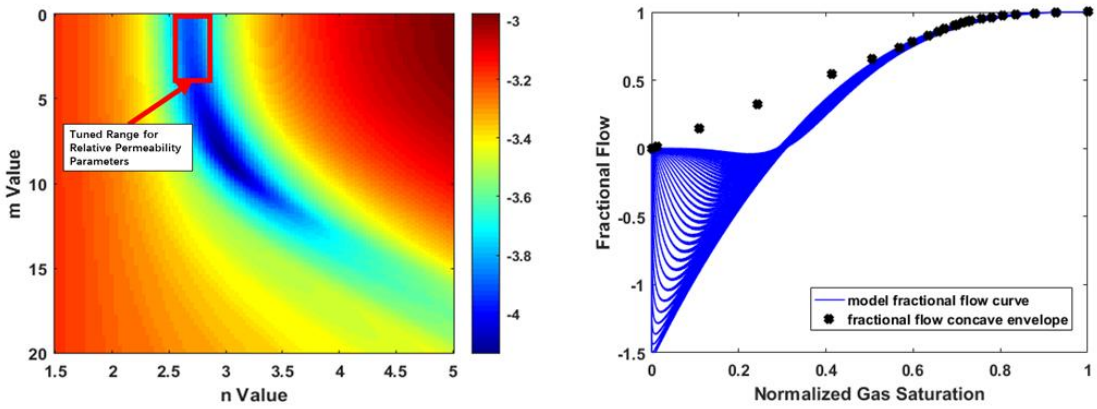

Figure 2.32 (a)-Range for relative permeability parameters constrained by both time-lapse data and composite saturation; (b)-corresponding fractional flow curves' range

We now expand the resolution for $-1.6 < \beta < -1$ and $0.01 < J_c < 0.15$. And we use only the relative permeability parameter pairs with $m < 4$ to calculate the root mean square again. The results are shown in the following figure.

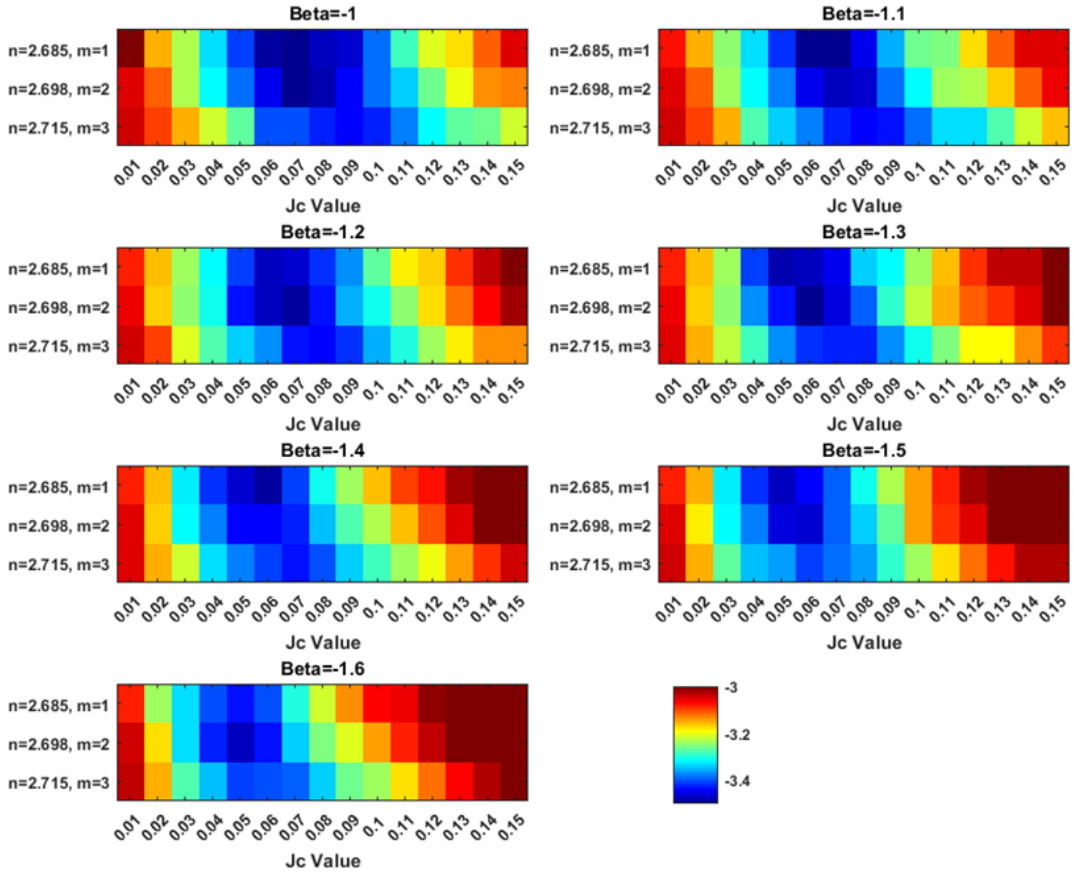

Figure 2.33 log10(RMS Error) plot between composite saturation model prediction and experimental data (finer resolution)

Now there are 47 pairs of parameters that meet the standard deviation criterion. Figure 2.34 shows the saturation profiles predicted using these parameters as well as the resulting capillary pressure curves.

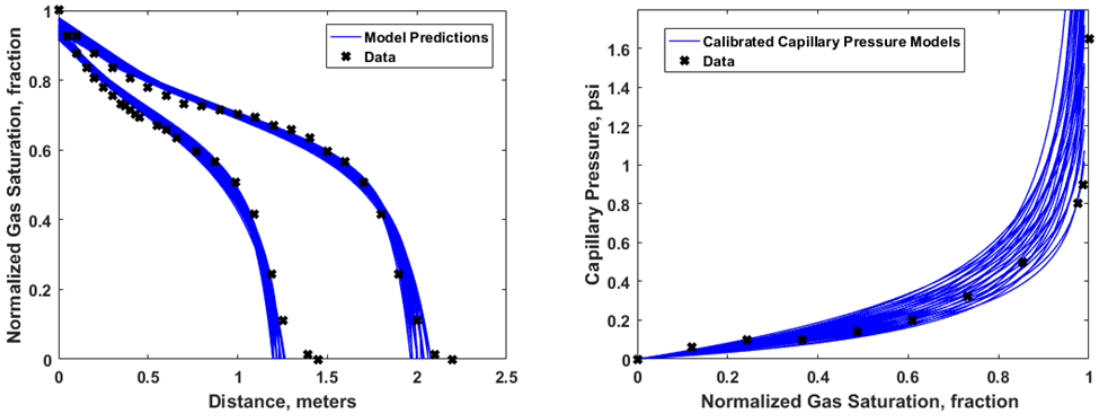

Figure 2.34 (a)-Composite saturation profiles predicted and experimental data; (b)-resulting capillary pressure curves

The above results show that the calibration of the capillary pressure curve is successful with a reasonable error bar.

Overall, the above results show that the analytical model is capable of calibrating the capillary pressure function as well as the concave envelope of the fractional flow from experimental saturation profiles.

2.5 Conclusions

We have provided an extension of the Buckley-Leverett solution for multiphase co-current forced imbibition or drainage flow to include capillary pressure corrections. It is within the context that the capillary pressure is relatively small thus the overall flow is still viscous dominated. The form of the solution is expressed in terms of pore volume coordinates which captures linear, radial or more general flow geometries. The solution is expressed as a composite of outer and inner solutions. The outer solution consists of the

smooth portion of the Buckley-Leverett profile while the inner solution consists of the "stabilized zone" steady state solution of Terwilliger. The two solutions match at the Buckley-Leverett shock saturation. The composite solution is a continuous solution which smoothly transitions across the Buckley-Leverett shock. The solution has been validated using numerical finite difference simulation.

As part of the analysis, we have introduced a new dimensionless group that describes the relative magnitude of capillary and viscous forces at the macroscopic scale. It differs from the capillary number which describes the relative magnitude of these forces at the pore scale (Steigemeir 1977) and is more akin to field scale dimensionless groups studied by other authors (Rashid et al. 2012). It is interesting to note that the current treatment which describes capillarity as a correction to viscous dominated flow cannot be implemented if the capillary number is too large. The range of solutions for which capillarity can be treated as a correction requires that $F_w''\left(S_{foot}^O\right) < 0$, where S_{foot}^O is the outer solution at the foot of the saturation profile. In a reservoir context, this is usually the case, with the notable exception of counter-current flow in fractured reservoirs, where this dimensionless group can be quite large due to small total velocities.

The methodology has also been applied to two laboratory-scale examples. The first has been to the prediction and analysis of the capillary end effect as seen in core flood measurements. It was further extended to estimate the relative permeability information from unsteady state experiments. The second has been to the use of the experimental saturation profile data to infer capillary pressure and fractional flow (relative permeability) information before water breakthrough.

CHAPTER III

SPONTANEOUS IMBIBITION‡

3.1 Introduction

Spontaneous imbibition is another important multiphase flow mechanism in porous media, and it is dominated by capillary pressure. Unlike the drainage or forced imbibition phenomenon discussed in the previous chapter where flow rates are imposed while the overall flow is viscous dominated, the flow rate from spontaneous imbibition is a natural consequence of the intrinsic properties of the fluid and rock system.

The spontaneous imbibition is recognized as important recovery mechanisms in naturally fractured reservoirs as the capillary force controls the movement of the fluid between the matrix and the fracture. For unconventional reservoirs, imbibition is also important as the capillary pressure is more dominant in these tighter formations. The theoretical understanding of the flow mechanism for the imbibition process will benefit the understanding of important multiphase flow phenomenon like water blocking.

In this chapter, a thorough theoretical investigation of the spontaneous imbibition mechanism is carried out, with the focus on the development of the semi-analytic solution for the transient spontaneous imbibition process. Unlike the self-similar solutions studied

---

‡ Part of this chapter is reprinted with permission from "Theoretical Investigation of the Transition from Spontaneous to Forced Imbibition" by Deng and King, 2018. *SPE Journal*, 24(01), 215-229. Copyright 2019, Society of Petroleum Engineers. Further reproduction prohibited without permission.

in the literature, the transient imbibition solution has yet been developed using the Lagrangian approach. However, the transient imbibition process represents more physical configurations such as constant flux at the outlet or ambient pressure at the outlet, while the only physically achievable condition with the self-similar solution is pure counter-current flow. The developed solution has been applied to both conditions to solve for the normalized water flux as well as the saturation profile.

Also, from the developed methodology, a novel stability envelope for spontaneous imbibition is also proposed to study the transition from spontaneous to forced imbibition by imposing a target injection rate at the inlet. Initially, the counter-current spontaneous imbibition at the inlet dominates, especially when the displacement front has only advanced a short distance. As flow front propagates, co-current flow gradually prevails and forced imbibition is achieved when the imbibition rate drops to the target injection rate.

3.2 Methodology

The methodology part will again start with the introduction of the mathematical formulation and some fundamentals of this two-phase flow problem. In all of the subsequent derivations in this section, the two phases are oil and water. The flow is assumed to be immiscible, incompressible, and the mass balance to both phases will hold. Following the derivation shown in the early part of the previous chapter, Eq (2.6) and Eq

(2.7) will still hold. To simplify the subsequent derivation, now we consider only one-dimensional problem. Thus, Eq (2.7) could be expressed as:

$$q_w = qF_w + \frac{Ak}{\mu_o}\lambda_D F_w F_o \frac{\partial p_c}{\partial x} \tag{3.1}$$

Eq (2.6) and Eq (3.1) combined still represents the governing equation for this two-phase flow problem. The solution strategy used in this chapter is an analog to the Buckley-Leverett problem where the fractional flow concept is still applied. However, in the Buckley-Leverett problem which is uni-directional, the largest positive flux is the total flux q. Thus, the fractional flow is normalized to this value in those types of problems. In the spontaneous imbibition literature, as counter-current flow is often happening, and sometimes even dominating, the largest flux is the water flux at the inlet q_{w0}. So, the fractional flow, which we are referring to as normalized water flux f_w^{Im}, should really be normalized to this water inlet flux to remain finite. For example, in the purely counter-current flow case, the traditional fractional flow will be infinite as total flux is zero, while the normalized water flux will always remain less than or equal to one. By applying the normalized water flux concept, Eq (3.1) could be rearranged as:

$$f_w^{\text{Im}} \equiv \frac{q_w}{q_{w0}} = \frac{q}{q_{w0}}F_w + \frac{Ak}{q_{w0}\mu_o}\lambda_D F_w F_o \frac{dp_c}{dS_w}\frac{\partial S_w}{\partial x} \tag{3.2}$$

The spatial and temporal variable can also be re-written for the porous media where $X^{\text{Im}} = \int_0 A\phi dx$, representing pore volume along the streamtube, and $T^{\text{Im}} = \int_0 q_{w0} dt$, representing the total imbibed water volume. Since in this chapter, the water saturation is not normalized to the mobile fraction, the rescaled spatial variable is slightly different

from what we had in the previous chapter. Also, here the rescaled temporal variable is with respect to inlet water flux, which is in consistency with the water flux normalization. Including some other variable changes such as $R = q/q_{w0}$ and $\xi^{\mathrm{Im}} = X^{\mathrm{Im}}/T^{\mathrm{Im}}$, Eq (3.2) could be further reduced to the following equation:

$$f_w^{\mathrm{Im}} = RF_w - \varepsilon_D^{\mathrm{Im}} G(S_w) \frac{\partial S_w}{\partial \xi^{\mathrm{Im}}} \tag{3.3}$$

In the above equation, the term $\varepsilon_D^{\mathrm{Im}} G(S_w)$ is simply another form of the capillary dispersion coefficient. The dimensionless non-linear diffusion coefficient G has the same definition as shown in Eq (2.22) after representing the capillary pressure using Leverett J-function: $p_c = \sigma\sqrt{\phi/k}\, J(S_w)$. However, for the capillary dimensionless group, the normalization is again with respect to the inlet water flux: $\varepsilon_D^{\mathrm{Im}} = \varepsilon/q_{w0}T^{\mathrm{Im}}$. The term ε follows the definition as shown in Eq (2.21). And for the one-dimensional case, we have:

$$\varepsilon = \frac{\sigma}{\mu_o}\sqrt{k\phi^3}A^2 \text{ and } \varepsilon_D^{\mathrm{Im}} = \frac{\varepsilon}{q_{w0}T^{\mathrm{Im}}} \tag{3.4}$$

As we will be showing some calculated results to illustrate the methodology, the following table listed all parameters used in this methodology part as input parameters.

Rock Properties		Water Relative Permeability and Fluid Properties		Oil Relative Permeability and Fluid Properties		Capillary Pressure	
$\boldsymbol{k}$	1.97E-13 m^2 (200 mD)	β_w	2	β_o	2	β_c	1
ϕ	0.2	S_{wirr}	0.2	S_{orw}	0.2	J_c	1
S_{wi}	0.2	μ_w	0.001 $Pa \cdot S$	μ_o	0.003 $Pa \cdot S$	S_{w0}	0.7
		$k_{rw}^{\max}$	0.6445	$k_{ro}^{\max}$	1	p_c^*	$\sigma\sqrt{\phi / k}$
						σ	0.05 N/m

Table 3.1 Model input parameters for example calculations of spontaneous imbibition

The S_{w0} is the saturation where capillary pressure equals zero. The relative permeability and capillary pressure (Leverett J-function) functional forms used in this methodology part are shown in the following three equations. The $k_{rw}^{\max}$ in our model is chosen such that $k_{rw}(S_w = 1) = k_{ro}(S_w = 0)$. For the relative permeability models, both the β_w and β_o needs to be greater or equal to 1. As for the J-function, β_c should be greater or equal to zero. When β_c equals zero, it gives the logarithmic form of the capillary pressure curve. All of these functional forms are continuous in the whole saturation range and differentiable. One thing to mention is that although here we have specified the functional forms, the methodology itself doesn't have the requirement of any specific functional form to be applicable.

$$k_{rw} = k_{rw}^{\max} \cdot \begin{cases} 0 & S_w \le S_{wirr} \\ \left(\dfrac{S_w - S_{wirr}}{1 - S_{orw} - S_{wirr}} \right)^{\beta_w} & S_{wirr} \le S_w \le 1 \end{cases}, \beta_w \ge 1 \tag{3.5}$$

$$k_{ro} = k_{ro}^{\max} \cdot \begin{cases} \left(\dfrac{1 - S_{orw}}{1 - S_{orw} - S_{wirr}} \right) \cdot \left(1 - \left(\dfrac{S_{wirr}}{1 - S_{orw}} \right) \cdot \left(\dfrac{S_w}{S_{wirr}} \right)^{\beta_o} \right) & S_w \le S_{wirr} \\ \left(\dfrac{1 - S_{orw} - S_w}{1 - S_{orw} - S_{wirr}} \right)^{\beta_o} & S_{wirr} \le S_w \le 1 - S_{orw} \\ 0 & S_w \ge 1 - S_{orw} \end{cases} \tag{3.6}$$

$$J\left(S_w\right) = J_c \cdot \begin{cases} \left(\dfrac{S_{w0} - S_{wirr}}{\beta_c} \right) \cdot \left(\left(\dfrac{S_w - S_{wirr}}{S_{w0} - S_{wirr}} \right)^{-\beta_c} - 1 \right) & S_{wirr} \le S_w \le S_{w0} \\ \left(\dfrac{1 - S_{orw} - S_{w0}}{\beta_c} \right) \cdot \left(1 - \left(\dfrac{1 - S_{orw} - S_w}{1 - S_{orw} - S_{w0}} \right)^{-\beta_c} \right) & S_{w0} \le S_w \le 1 - S_{orw} \end{cases} \tag{3.7}$$

The following figure shows the outcome relative permeability and Leverett J-function curves based on the above table parameters. One key information is that for this intermediate wet case, the capillary pressure curve has portions in both positive and negative value ranges. The S_{w0} is the saturation where capillary pressure equals zero, and the end-point saturation of the relative permeability curves is $1 - S_{orw}$ which is larger than S_{w0}. The irreducible water saturation S_{wirr} is consistent in both curves and is assumed to be the same as initial water saturation. This assumption is also in consistency with all previous analytical attempts in its class.

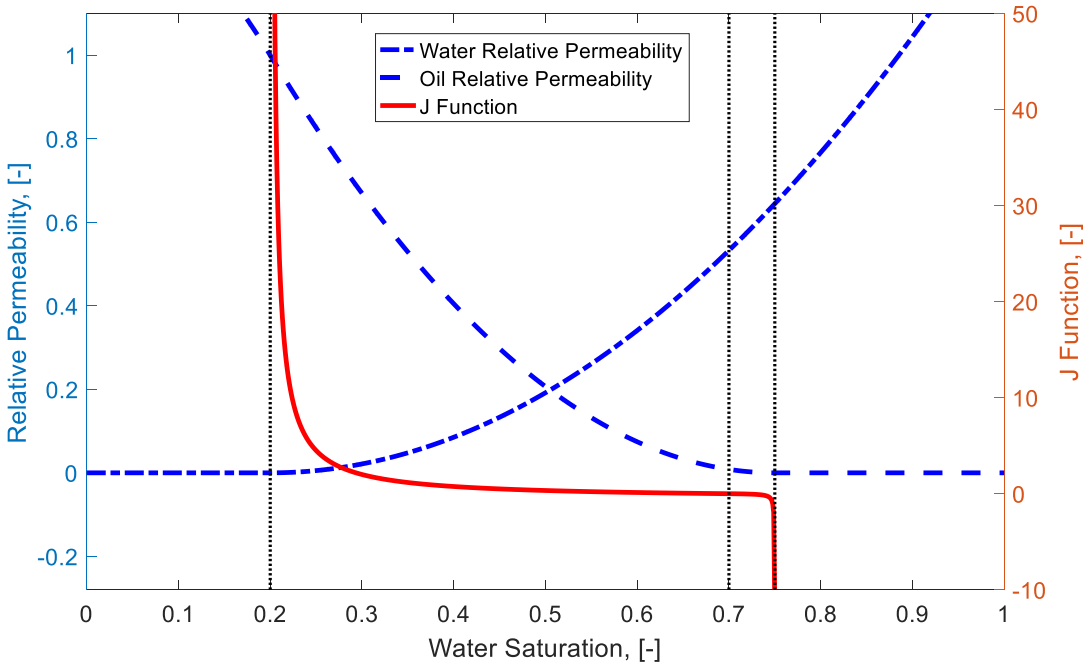

Figure 3.1 Relative permeability and capillary pressure (J-function) curves used for spontaneous imbibition methodology part

The above figure shows the relative permeability and Leverett J-function for the water saturation range between 0 and 1. For the saturation range below irreducible water saturation, the water relative permeability is constantly zero while oil phase relative permeability is gradually increasing with decreasing water saturation. For the saturation range above $1-S_{orw}$, the oil relative permeability stays zero while the water relative permeability increases with increasing water saturation. The saturation endpoints where phase relative permeability just turns zero should match the saturation at which the capillary pressure curve diverges (as shown in Figure 3.1). For the continuum scale two-

phase flow problems, normally we only consider the water saturation between S_{wirr} and $1-S_{orw}$, however, the above type of relative permeability curve has also been studied in the literature from percolation theory (Helba et al. 1992) or used to illustrate phase trapping problems where initial water saturation is below irreducible water saturation (Bennion and Thomas 2005). The extension to fluid flow below irreducible water saturation or above residual oil saturation is not within the scope of this chapter, but will be discussed in the next chapter.

For the study of imbibition mechanisms, it is important to distinguish between S_{w0} and end-point water saturation $1-S_{orw}$, and the underlying different boundary conditions due to different mechanisms. At the spontaneous imbibition phase, as the inlet boundary condition has capillary equal zero, only the part of the relative permeability and capillary pressure curves below S_{w0} will contribute. This phenomenon has fixed the inlet water saturation at a constant value S_{w0} and all saturation within the porous media afterward will not exceed this value. On the other hand, during the forced imbibition or drainage process, the inlet boundary is controlled by a determined fractional flow. Thus, there will be no constraint on the inlet saturation anymore and the portion above S_{w0} could very well be contributing.

In all our subsequent analysis, the major assumption is that the flow is immiscible and incompressible. We are also using only one set of relative permeability and capillary pressure curves in the derivation. Although the relative permeability and capillary pressure hysteresis will kick in when the saturation changes are in different directions, and it is easy

to happen when both co-current and counter-current flows are happening, it is not happening in the current scope as the water saturation is constantly increasing for the conditions we are studying here.

Also, the system is assumed to have constant initial water saturation that is the same as irreducible water saturation, and constant residual oil saturation to start with. This assumption is in consistency with the assumptions in all other analytical solution in this class. If we have a non-uniform distribution of initial saturation, there will be two different situations. The first one is when the initial water saturation distribution, although non-uniform, is consistently lower than the irreducible water saturation. This case will happen in some gas shales like Marcellus or Haynesville (Bennion and Thomas 2005; Wang and Reed 2009). At such condition, the water is not able to flow but is being controlled by adsorption due to the presence of clay minerals. The incorporation of this situation is analyzed in the next chapter. The second condition is the initial water saturation is above irreducible water saturation and non-uniformly distributed. For this situation, due to the existence of capillarity, the water saturation within the porous media is not at its equilibrium and will continue redistributing.

The above description and statements summarized the fundamentals of the spontaneous imbibition two-phase flow problem we are analyzing here. Now, we will start reviewing the self-similar solution and providing the details regarding the construction of the analytic solution for transient imbibition.

3.2.1 Self-similar Solution Review

According to the temporal and spatial variable change description provided at the beginning of this chapter, Eq (2.6) could be written as:

$$\frac{\partial S_w}{\partial T^{\mathrm{Im}}} + \frac{\partial f_w^{\mathrm{Im}}}{\partial X^{\mathrm{Im}}} = 0 \tag{3.8}$$

In order to construct the self-similar solution where both the saturation profile and the normalized water flux are only a function of ξ^{Im}, the term ξ^{Im} becomes the similarity variable and the following relationship will hold.

$$\begin{aligned} 0 &= \frac{\partial S_w}{\partial T^{\mathrm{Im}}} + \frac{\partial f_w^{\mathrm{Im}}}{\partial X^{\mathrm{Im}}} = -\frac{dS_w}{d\xi^{\mathrm{Im}}} + \frac{df_w^{\mathrm{Im}}}{d\xi^{\mathrm{Im}}}\frac{1}{T^{\mathrm{Im}}} \\ &= -\frac{dS_w}{d\xi^{\mathrm{Im}}}\frac{\xi^{\mathrm{Im}}}{T^{\mathrm{Im}}} + \frac{df_w^{\mathrm{Im}}}{dS_w}\frac{dS_w}{d\xi^{\mathrm{Im}}}\frac{1}{T^{\mathrm{Im}}} = \frac{1}{T^{\mathrm{Im}}}\left(\frac{dS_w}{d\xi^{\mathrm{Im}}}\right)\left(-\xi^{\mathrm{Im}} + \frac{df_w^{\mathrm{Im}}}{dS_w}\right) \end{aligned} \tag{3.9}$$

For the above equation to hold in the most general case, we will further have:

$$\xi^{\mathrm{Im}} = \frac{df_w^{\mathrm{Im}}}{dS_w} \tag{3.10}$$

We could also re-write Eq (3.3) as:

$$f_w^{\mathrm{Im}} = RF_w - \varepsilon_D{}^{\mathrm{Im}} G(S_w)\frac{dS_w}{d\xi^{\mathrm{Im}}} \text{ or } \frac{d\xi^{\mathrm{Im}}}{dS_w} = \frac{-\varepsilon_D G(S_w)}{f_w^{\mathrm{Im}} - RF_w} \tag{3.11}$$

By combining Eq (3.10) with Eq (3.11), we arrive at the governing equation for the self-similar solution. For a self-similar solution, each term within the definition of the normalized water flux may depend upon S_w, ξ^{Im} and derivatives, but they may not depend upon time. This imposes two constraints:

$$R \equiv \frac{q}{q_{w0}} \leq 1 \tag{3.12}$$

$$\frac{q_{w0} T^{\mathrm{Im}}}{A^2} = \frac{T^{\mathrm{Im}}}{A^2} \frac{dT^{\mathrm{Im}}}{dt} = Const. \tag{3.13}$$

From the second equation above, we arrive at the key observations for the self-similarity where:

$$\begin{aligned} &\text{Linear Flow: } q_{w0} = \frac{AC^{\mathrm{Im}}}{\sqrt{t}}, T^{\mathrm{Im}} = 2AC^{\mathrm{Im}}\sqrt{t} \text{ for some } C^{\mathrm{Im}} \\ &\text{Radial Flow: } q_{w0} = C^{\mathrm{Im},radial} \end{aligned} \tag{3.14}$$

In the original derivation by McWhorter and Sunada, the inlet water flux being proportional to the inverse of the square root of time was treated as a boundary condition, and the self-similar solution is derived under such condition. Here we have proved that the $q_{w0} \propto 1/\sqrt{t}$ condition is a natural consequence of the self-similarity, not the other way around. Also, the C^{Im} and $C^{\mathrm{Im},radial}$ factors are constants based on specific rock and fluid systems and cannot be chosen arbitrarily.

As we have introduced before, in the previous literature, the above described self-similar solution has been solved using different techniques. We have found that the finite difference method originally proposed by Schmid et al. (2016) is easy to implement. However, as they were only solving for the normalized water flux using a second order finite difference scheme, some of the fundamental physics behind the solution are hidden. In our approach, we have used an improved finite difference scheme to solve two first-order ODEs simultaneously, and we can actually see the behavior of both the normalized water flux and saturation profile as the same time. Once we discretize Eq (3.10) and Eq

(3.11) with respect to water saturation, we arrive at the following two discretized equations where i denotes the steps in water saturation:

$$\left[f_w^{\,\mathrm{Im}}\right]_i = \left[f_w^{\,\mathrm{Im}}\right]_{i-1} + \left(S_{w_i} - S_{w_{i-1}}\right)\left[\xi^{\mathrm{Im}}\right]_{i-1} \tag{3.15}$$

$$\left[\xi^{\mathrm{Im}}\right]_i = \left[\xi^{\mathrm{Im}}\right]_{i-1} - \frac{\left(S_{w_i} - S_{w_{i-1}}\right)\varepsilon_D^{\,\mathrm{Im}} G\left(S_{w_i}\right)}{\left[f_w^{\,\mathrm{Im}}\right]_i - RF_{w_i}} \tag{3.16}$$

The solution strategy is more akin to a shooting process for this two-point boundary value problem. At the inlet, we have the inlet boundary condition as $\left[f_w^{\,\mathrm{Im}}\right]_0 = 1$, $\left[\xi^{\mathrm{Im}}\right]_0 = 0$ and $S_{w_0} = S_{w0}$. Since R is a known constant, the only unknown is $\varepsilon_D^{\,\mathrm{Im}}$. The value of $\varepsilon_D^{\,\mathrm{Im}}$ is perturbed during the shooting process to converge to the correct foot boundary condition where $\left[f_w^{\,\mathrm{Im}}\right]_{end} = 0$, $\left[\xi^{\mathrm{Im}}\right]_{end} = finite$ and $S_{w_{end}} = S_{wirr}$.

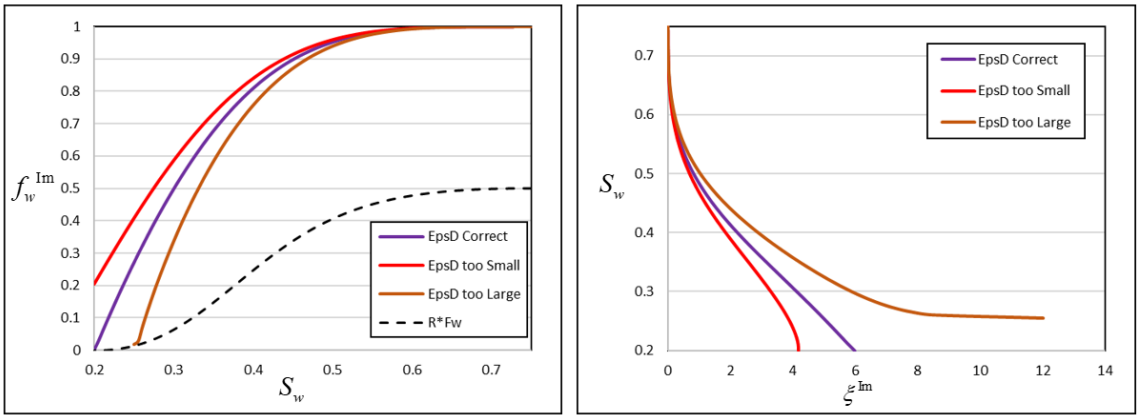

Figure 3.2 (a)-Normalized water flux behavior during shooting process for self-similar solution; (b)-saturation profile behavior during shooting process for self-similar solution

The above two figures graphically explain the shooting process for the self-similar solution to obtain the correct $\varepsilon_D^{\text{Im}}$ value. If $\varepsilon_D^{\text{Im}}$ is smaller than the correct value, the normalized water flux will terminate at $f_w^{\text{Im}}\left(S_{wirr}\right) > 0$, which is not physical. As the same time, the saturation profile will have an ill-posed mass balance. If the $\varepsilon_D^{\text{Im}}$ is large, the normalized water flux will intersect with RF_w curve and cause the equations to diverge. Also, the saturation profile will be shooting for infinity at the saturation where the equation diverged. There exists only one correct $\varepsilon_D^{\text{Im}}$ value that will match the correct foot boundary condition as shown in the purple curve above. And this $\varepsilon_D^{\text{Im}}$ value will help determine the C^{Im} value which is the pre-factor for the imbibition rate.

And also, as we change the value of R, there will be different calculated $\varepsilon_D^{\text{Im}}$ values. The relationship between $\varepsilon_D^{\text{Im}}$ and R is a natural consequence of the system itself and is also very important as it determines the correct imbibition rates. The following figure shows one typical example of the $\varepsilon_D^{\text{Im}}$ and R relationship from the self-similar solution:

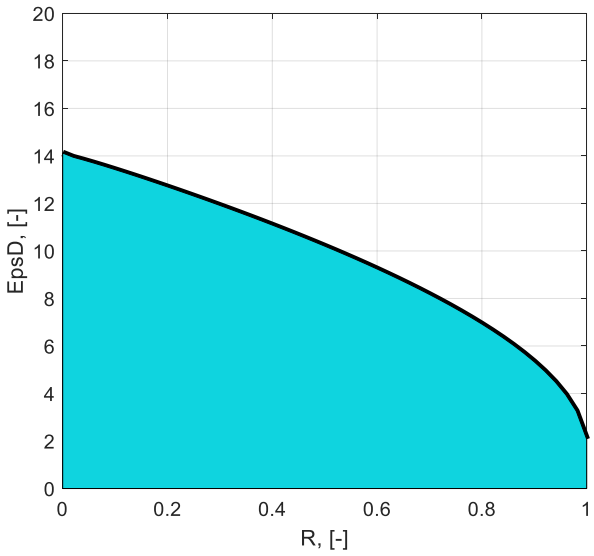

Figure 3.3 $\varepsilon_D^{\text{Im}}$ vs. R relationship example from self-similar solution

As the unique $\varepsilon_D^{\text{Im}}$ value will in turn determine the imbibition rate, the above curve also will represent the difference between a stable and an unstable imbibition process. If at any predetermined R, the $\varepsilon_D^{\text{Im}}$ value is too large will mean that the imbibition rate is too small. This situation is physically not achievable as the capillary pressure by itself will increase the rate to the rata prescribed by the above relationship. However, if the $\varepsilon_D^{\text{Im}}$ value is too small, the imbibition rate will be large than what is achievable from capillarity only. Thus, additional viscous pressure drop is needed to increase the imbibition rate. This is what we will refer to as forced imbibition. The details about the interaction between spontaneous and forced imbibition will be discussed in a later section of this chapter.

To be noted, all these self-similar solutions are possible mathematical solutions, however the relationship is not physically (energetically) feasible for a finite system unless $q = 0$, i.e., pure counter-current flow. All the laboratory experiments that exhibit self-similar behavior are of this nature. Alternatively, the solutions will not be purely self-similar, as in the current investigation.

3.2.2 Transient Solution

As for the transient imbibition problems, the main difference comparing with the self-similar solution is that the terms within the definition of the normalized water flux could now vary with time, i.e. $\xi^{\mathrm{Im}}\left(S_w, T^{\mathrm{Im}}(t)\right)$, $f_w{}^{\mathrm{Im}}\left(S_w, T^{\mathrm{Im}}(t)\right)$, $\varepsilon_D{}^{\mathrm{Im}}\left(T^{\mathrm{Im}}(t)\right)$ and $R\left(T^{\mathrm{Im}}(t)\right)$. We now start with the Eulerian form of the flow equations, Eq (2.6), and transform them into the Lagrangian form used in the solution of the spontaneous and transient imbibition problem. In the Eulerian formulation, the unknown functions $S_w(x,t)$ and $q_w(x,t)$ are expressed as functions of position and time as the independent variables. For the Lagrangian formulation, we instead determine the solutions as functions of saturation and time. This changes the interpretation of the time derivative to a co-moving derivative, as shown in the following. As part of this transformation we also introduce the rescaled position and time variables defined in terms of cumulative pore volume calculated from the inlet and the cumulative water imbibed.

We now introduce the change of independent variable from (x,t) to $\left(S_w, T^{\mathrm{Im}}\right)$:

$$\left(\frac{\partial}{\partial x}\right)_t = \left(\frac{\partial S_w}{\partial x}\right)_t \cdot \left(\frac{\partial}{\partial S_w}\right)_{T^{\mathrm{Im}}} + 0 \cdot \left(\frac{\partial}{\partial T^{\mathrm{Im}}}\right)_{S_w}$$
$$\left(\frac{\partial}{\partial t}\right)_x = \left(\frac{\partial S_w}{\partial t}\right)_x \cdot \left(\frac{\partial}{\partial S_w}\right)_{T^{\mathrm{Im}}} + \left(\frac{\partial T^{\mathrm{Im}}}{\partial t}\right)_x \cdot \left(\frac{\partial}{\partial T^{\mathrm{Im}}}\right)_{S_w} \tag{3.17}$$

Manipulating these relationships gives:

$$\left(\frac{\partial X^{\mathrm{Im}}}{\partial T^{\mathrm{Im}}}\right)_{S_w} = \frac{1}{q_{w0}}\left(\frac{\partial q_w}{\partial S_w}\right)_{T^{\mathrm{Im}}} \tag{3.18}$$

Here, both X^{Im} and t are functions of S_w and T^{Im}. In these expressions and for clarity, the variable kept fixed in the partial derivative is stated explicitly. For instance $\left(\frac{\partial}{\partial t}\right)_x$ is the time derivative at fixed position while $\left(\frac{\partial}{\partial T^{\mathrm{Im}}}\right)_{S_w}$ is the time derivative at fixed saturation. The latter is also known as the co-moving time derivative.

Two dimensionless variables naturally arise. The first is the normalized water flux, $f_w^{\mathrm{Im}} \equiv q_w / q_{w0}$. The second is the dimensionless ratio of X^{Im} and T^{Im}, $\xi^{\mathrm{Im}} = X^{\mathrm{Im}} / T^{\mathrm{Im}}$. From Eq (3.1) we have their relationship:

$$f_w^{\mathrm{Im}} = \frac{q}{q_{w0}} F_w + \frac{1}{q_{w0} \cdot T^{\mathrm{Im}}} \frac{A^2 k \phi}{\mu_o} \lambda_D F_w F_o \frac{dp_c}{dS_w} \left(\frac{d\xi^{\mathrm{Im}}}{dS_w}\right)^{-1} \tag{3.19}$$

This is what the literature has explored as the self-similar solution and we have in detailed reviewed it in previous chapters. If we now focus on the investigation of transient imbibition with the use of average normalized water flux $\overline{f_w^{\mathrm{Im}}}$, Eq (3.18) could now be expressed as:

$$\left(\frac{\partial X^{\mathrm{Im}}}{\partial T^{\mathrm{Im}}}\right)_{S_w} = \left(\frac{\partial f_w^{\mathrm{Im}}}{\partial S_w}\right)_{T^{\mathrm{Im}}} \tag{3.20}$$

The time dependent terms in the normalized water flux are $\left(q/q_{w0}\right)$ and $1/\left(q_{w0}\cdot T^{\mathrm{Im}}\right)$. They must be obtained as part of the solution of the equations.

Eq (3.20) and Eq (3.3) together represent the governing equation to the transient imbibition problem. We will re-write Eq. (3.3) into the following form:

$$\frac{\partial \xi^{\mathrm{Im}}}{\partial S_w} = \frac{-\varepsilon_D{}^{\mathrm{Im}} G(S_w)}{f_w{}^{\mathrm{Im}} - RF_w} \tag{3.21}$$

Unlike the self-similar case, there now exists a lack of connection between the normalized water flux and its change with respect to time. Thus, we have introduced an average normalized water flux to establish the connection.

$$\int f_w{}^{\mathrm{Im}} dT^{\mathrm{Im}} = T^{\mathrm{Im}} \cdot \overline{f_w{}^{\mathrm{Im}}} \tag{3.22}$$

$$f_w{}^{\mathrm{Im}} = \frac{d\left(T^{\mathrm{Im}} \cdot \overline{f_w{}^{\mathrm{Im}}}\right)}{dT^{\mathrm{Im}}} \tag{3.23}$$

Now, the original similarity variable, or equivalently the rescaled saturation profile could be written as:

$$\xi^{\mathrm{Im}} \equiv \frac{X^{\mathrm{Im}}}{T^{\mathrm{Im}}} = \frac{\partial \overline{f_w{}^{\mathrm{Im}}}}{\partial S_w} \tag{3.24}$$

Eq (3.24), Eq (3.23) and Eq (3.21) combined is the complete governing equation to the transient imbibition problem. The solution strategy is identical to what we have analyzed in the self-similar condition, with the change of including one more equation to be discretized. Because of the time dependence, the shooting process is accomplished at

every temporal step. Once the shooting processes are done for all temporal steps, the solution gives us the relationship between R, $\varepsilon_D^{\mathrm{Im}}$, saturation profiles and normalized water flux. Thus, the overall solution is also determined.

For each shooting process to calculate the correct $\varepsilon_D^{\mathrm{Im}}$ at every time step, the inlet boundary condition is still capillary pressure equals zero, which will force the inlet saturation to be constant S_{w0}. Also, at the inlet, $f_w^{\mathrm{Im}}=1$, $\overline{f_w^{\mathrm{Im}}}=1$ and $\xi^{\mathrm{Im}}=0$. At the foot of the saturation profile (the saturation front), the boundary conditions are $S_w=S_{wirr}$, $f_w^{\mathrm{Im}}=0$, $\overline{f_w^{\mathrm{Im}}}=0$ and ξ^{Im} remains finite. And to initialize the solution at the first time step, the $R=0$ self-similar solution is used as $f_w^{\mathrm{Im}}=\overline{f_w^{\mathrm{Im}}}$ for the first timestep.

As a consequence of the time dependence, the discretization needs to be done in both S_w and T^{Im}.

$$n=0:N_{T^{\mathrm{Im}}},\left[T^{\mathrm{Im}}\right]^n=n\cdot\Delta T^{\mathrm{Im}},\left[T^{\mathrm{Im}}\right]^{end}=N_T\cdot\Delta T^{\mathrm{Im}} \tag{3.25}$$

$$i=0:N_{S_w},S_{w_i}=S_{w0}+i\cdot\Delta S_w,\Delta S_w=\left(S_{wirr}-S_{w0}\right)\big/N_{S_w} \tag{3.26}$$

Here i is used to describe the saturation discretization and n is used for the temporal step notation. With the discretization scheme, Eq (3.24), Eq (3.23) and Eq (3.21) could be discretized as:

$$\left[\overline{f_w^{\,\mathrm{Im}}}\right]_i^n = \left[\overline{f_w^{\,\mathrm{Im}}}\right]_{i-1}^n + \Delta S_w \left[\xi^{\mathrm{Im}}\right]_{i-1}^n \tag{3.27}$$

$$\left[f_w^{\,\mathrm{Im}}\right]_i^n = \frac{\left[T^{\mathrm{Im}}\right]^n \cdot \left[\overline{f_w^{\,\mathrm{Im}}}\right]_i^n - \left[T^{\mathrm{Im}}\right]^{n-1} \cdot \left[\overline{f_w^{\,\mathrm{Im}}}\right]_i^{n-1}}{\Delta T^{\mathrm{Im}}} \tag{3.28}$$

$$\left[\xi^{\mathrm{Im}}\right]_i^n = \left[\xi^{\mathrm{Im}}\right]_{i-1}^n + \frac{\Delta S_w \cdot \left[\varepsilon_D^{\,\mathrm{Im}}\right]^n \cdot G\left(S_{w_i}\right)}{\left[f_w^{\,\mathrm{Im}}\right]_i^n - R^n \cdot F_{w_i}} \tag{3.29}$$

From the equations, we need another relationship between $\left[\varepsilon_D^{\,\mathrm{Im}}\right]^n$ and R^n to close all the equations. According to Eq (3.4), we will have:

$$\left[\varepsilon_D^{\,\mathrm{Im}}\right]^n = \frac{\varepsilon}{q_{w0}\left[T^{\mathrm{Im}}\right]^n} = \frac{\varepsilon R^n}{q\left[T^{\mathrm{Im}}\right]^n} \tag{3.30}$$

From the above equation, the additional boundary condition needed for the extra unknown could be resolved by either knowing R^n directly or knowing q. This additional relationship is derived from the outlet boundary condition of a given system. Once we obtain the additional boundary condition, the only unknown remains is still $\left[\varepsilon_D^{\,\mathrm{Im}}\right]^n$ and we will again perturb it to match the foot boundary condition. It is accomplished by minimizing the objective function as shown in the following equation and a typical shooting example is shown in Figure 3.4.

$$\min\ O = \left(S_w^{\ term} - S_{wirr}\right)^2 + \left(\left[f_w^{\ \mathrm{Im}}\right]^{term}\right)^2 \tag{3.31}$$

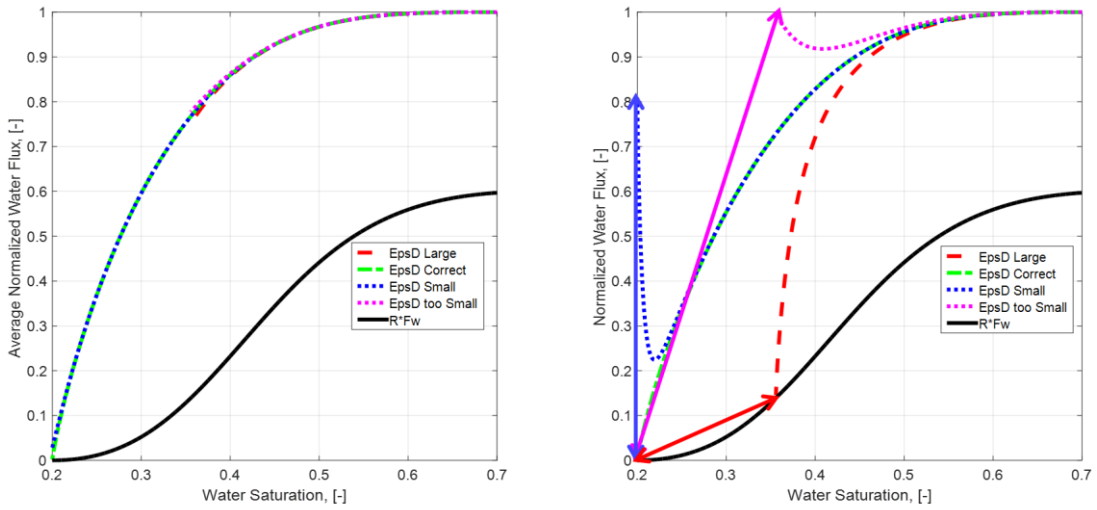

Figure 3.4 (a)-Average normalized water flux behavior for transient solution; (b)-Instantaneous normalized water flux behavior for transient solution;

The terms $S_w^{\ term}$ and $\left[f_w^{\ \mathrm{Im}}\right]^{term}$ represent the terminating values for water saturation and instantaneous normalized water flux during the shooting algorithm. The objective function represents the square of the length between the terminating point to the origin as shown in Figure 3.4b. As an initial guess for $\varepsilon_D^{\ \mathrm{Im}}$, it can be any value specified.

If the $\varepsilon_D^{\ \mathrm{Im}}$ is a lot smaller than the correct value, as shown in the magnet line in Figure 3.4b, we will be terminating the shooting of $f_w^{\ \mathrm{Im}}$ at 1. Thus, the $S_w^{\ term}$ will be larger than S_{wirr} and $\left[f_w^{\ \mathrm{Im}}\right]^{term}$ will be 1. As the value of $\varepsilon_D^{\ \mathrm{Im}}$ increases, before the terminating normalized water flux becomes always smaller than 1, the $\left[f_w^{\ \mathrm{Im}}\right]^{term}$ will not

change while the S_w^{term} will be closer to the irreducible water saturation. Thus, the value of the objective function is always decreasing in this case. When the terminating normalized water flux stays below 1 (as shown in the blue curve), the S_w^{term} will equal to S_{wirr} and $\left[f_w^{\mathrm{Im}} \right]^{term}$ will decrease until 0 with increasing $\varepsilon_D^{\mathrm{Im}}$. Thus, for all $\varepsilon_D^{\mathrm{Im}}$ below the correct value, the objective function value will always decrease with increasing $\varepsilon_D^{\mathrm{Im}}$.

If the $\varepsilon_D^{\mathrm{Im}}$ is larger than the correct value, the shooting trajectory of normalized water flux will terminate at $\left[f_w^{\mathrm{Im}} \right]^{term} = R \cdot F_w$. Again, as we can infer from monotonicity of the water fractional mobility curve as shown in black in Figure 3.4b, the S_w^{term} will be converging to S_{wirr} and the $\left[f_w^{\mathrm{Im}} \right]^{term}$ will be converging to 0 with decreasing $\varepsilon_D^{\mathrm{Im}}$. Thus, the objective function is constantly decreasing with decreasing $\varepsilon_D^{\mathrm{Im}}$ as well.

The above description concludes that there exists a unique $\varepsilon_D^{\mathrm{Im}}$ at every time step for the solution of normalized water flux, and objective function has a unique global solution with a smooth and concave shape. Thus, any type of optimization algorithm could be applied to solve this problem.

Also in Figure 3.4a, it is shown that when the estimated $\varepsilon_D^{\mathrm{Im}}$ is too small, the average normalized water flux at S_{wirr} will terminate at a value larger than zero. This means the normalized water flux is non-zero while the $G(S_w)$ is zero, and this situation is not physical. Also, we will observe an invalid mass balance. When $\varepsilon_D^{\mathrm{Im}}$ is too large,

the governing equation will diverge at some saturation when $\left[f_w^{\text{Im}} \right]^{term} = R \cdot F_w$ and causing the denominator to approach zero (shown in Figure 3.4b at the crossing of the red dash line and black solid line). This is also shown in Figure 3.5 where we can see the saturation at which the equation diverges will be shooting for infinity.

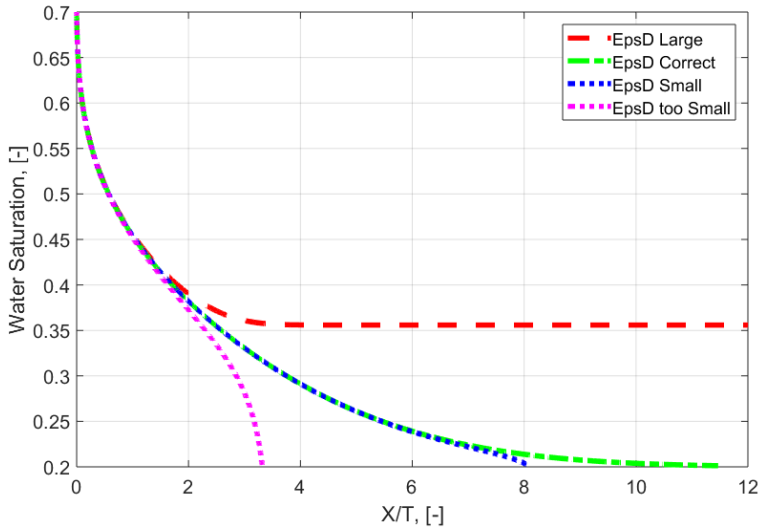

Figure 3.5 Saturation vs. ξ plot for transient imbibition problem

The convergence of our finite difference calculation for the transient imbibition problem is discussed in Appendix C.

This concludes the general derivation and solution strategies for the transient imbibition problem. However, until now, all derivation is done using T^{Im} as the independent variable. To obtain the relationship between all solutions and the physical time, the following relationship is used:

$$T^{\mathrm{Im}} = \int_0 q_{w0} dt \tag{3.32}$$

$$t = \int_0 \frac{1}{q_{w0}} dT^{\mathrm{Im}} = \int_0 \frac{\varepsilon_D{}^{\mathrm{Im}} T^{\mathrm{Im}}}{\varepsilon} dT^{\mathrm{Im}} \tag{3.33}$$

3.3 Application

3.3.1 Application of Analytic Solution with Physical Boundary Conditions

We will consider three physical configurations for this study and start to analyze the corresponding application of the analytic solutions to them.

3.3.1.1 Purely Counter-current Flow

If the porous media is semi-infinite or it only has one end open to flow, the R ratio will become zero as there will be no flux at the outlet. Thus, the overall flow condition becomes purely counter-current. Under such circumstance, the solution is reduced to the self-similar solution and the relationship of $\varepsilon_D{}^{\mathrm{Im}}(R)$ is simplified to a single point. As the self-similar solution is well documented in the literature, the detailed example calculation will not be illustrated here.

3.3.1.2 Constant Outlet Flux

The second physical condition is when the system has both ends open to flow. The inlet is constantly in contact with water, and oil is being produced at a constant rate at the

outlet. The system could still be semi-infinite, or the solution is only valid before the water breakthrough at the outlet for a finite length system. As the oil production at the outlet is a constant, and it will be equal to q under incompressible constraint, the additional boundary condition is directly given. The following figure shows the example calculation under such flow configuration.

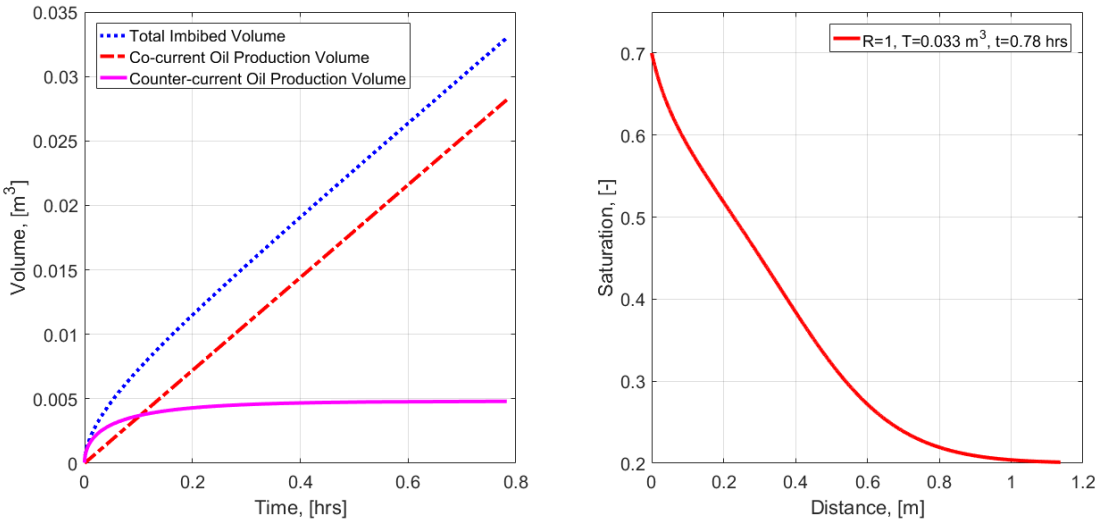

Figure 3.6 (a)-total imbibed volume, co-current and counter-current oil production volume changing with time for constant outlet flux transient imbibition; (b)-saturation profile at one time step for constant outlet flux transient imbibition

In Figure 3.6a, we can see the co-current oil production is increasing linearly with time, and this is in accordance with our model set-up, i.e. outlet boundary condition. From the comparison of the total imbibed volume, co-current and counter-current oil production, we can see that at early time, counter-current spontaneous imbibition is dominating, and it is driven by the capillary force. Until later time, the production is mainly due to the constant outlet oil withdrawal.

We further validated our analytic solution result with numerical simulation results. Traditional commercial simulators are built for well boundary conditions and are not designed to handle this type of capillary pressure boundary condition. Thus, an in-house simulator is built for this 1-D problem. The construction of the simulator is identical to the methods provided by Karimaie et al (2004), with the change on the outlet boundary condition to be a constant production rate. For the algorithm used in the simulator, IMPES method is applied.

For the numerical simulation, we have tested the simulator under five different cell sizes. The total length of the system is 1.6 meters, and it is divided into 20, 50, 200, 500 and 2000 cells, leading to cell sizes of 0.08, 0.032, 0.008, 0.0032 and 0.0008 meters per grid. The following figure shows the saturation profiles from both the analytic result as well as all five numerical simulations.

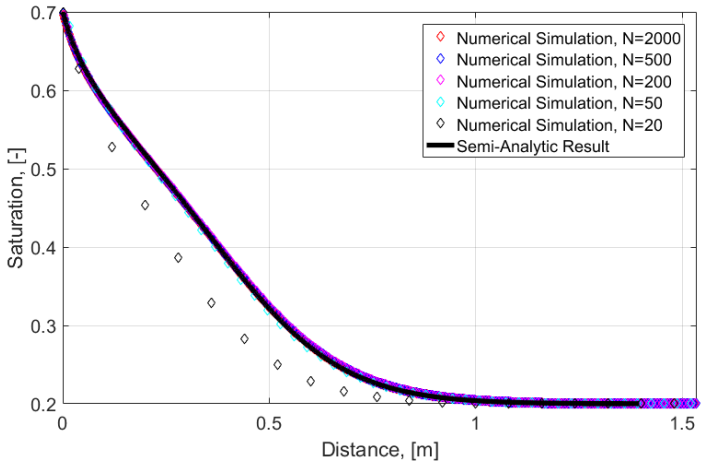

Figure 3.7 Saturation comparison between semi-analytic result and multiple numerical simulations for constant outlet flux transient imbibition

As we can see from the above figure, the semi-analytic result is in good agreement with numerical simulation results and is closer once the cell size is smaller in the simulation. This has validated our semi-analytic approach. We also computed the root mean square error (RMS error) using the most refined simulation result as the basis, and the convergence test result is shown in the next figure.

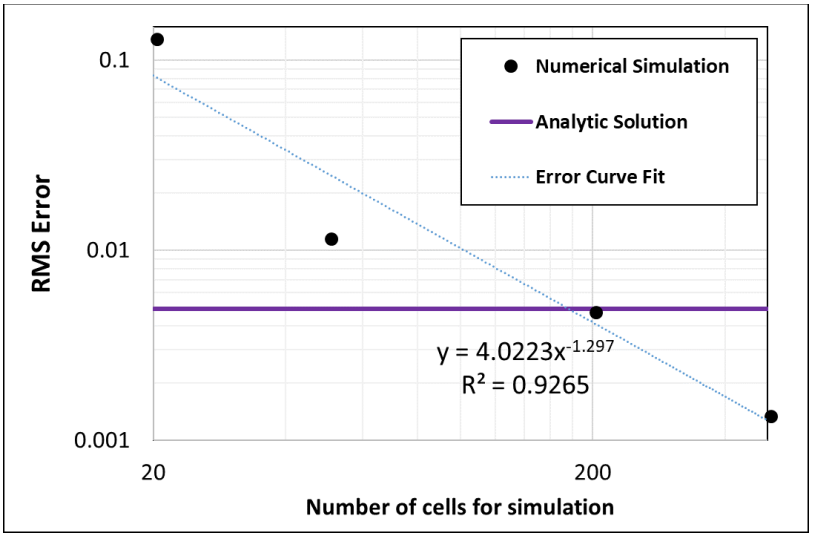

Figure 3.8 Semi-analytic solution and numerical simulation convergence analysis for constant outlet flux transient imbibition

From the convergence test comparing with simulation results, the simulation result shows a convergence rate close to 1.3. The semi-analytic result's accuracy is approximately about 200 cells for a 1.6-meter-long system, which is about 0.008 meters per cell. To be noted, this accuracy could be further improved once we increase the resolution when solving the semi-analytic solution using finite difference approach.

3.3.1.3 Two-Ends-Open (TEO) Free Spontaneous Imbibition

The Two-Ends-Open (TEO) free spontaneous imbibition, is a one-dimensional experimental configuration where the inlet of the core is in contact with water and the outlet is in contact with oil. The experimental configuration is shown in Figure 3.9. On both ends of the core, the two reservoirs containing water and oil are both at constant ambient pressure. Originally the water wet core is filled with oil that has the same property as the oil in the outlet reservoir. At the inlet, we have a capillary end effect that will set the capillary pressure to zero. At the core outlet, the pressure will also be at the ambient pressure due to the contact with the oil reservoir. Under such a configuration, the oil will be produced both co-currently (produced at the outlet) and counter-currently (produced at the inlet), and the strength of them will be constantly changing.

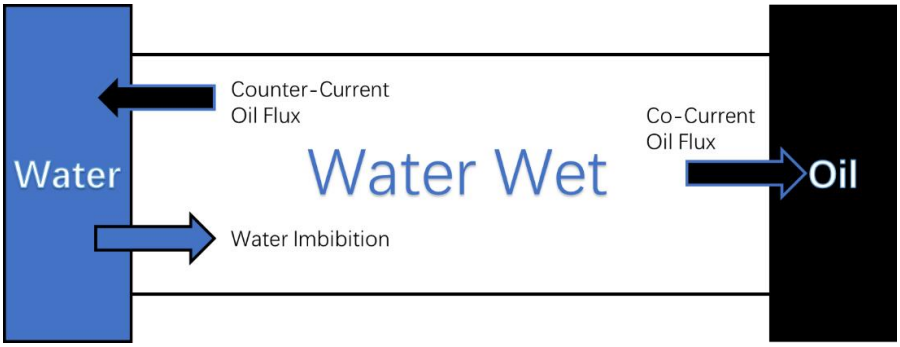

Figure 3.9 Illustration of Two-Ends-Open (TEO) free spontaneous imbibition configuration

To apply the transient solution for the TEO free spontaneous imbibition, we will have to take the physical boundary condition into consideration. The boundary condition

for this problem is the oil phase pressure on both ends being equal to ambient pressure as shown in the following figure.

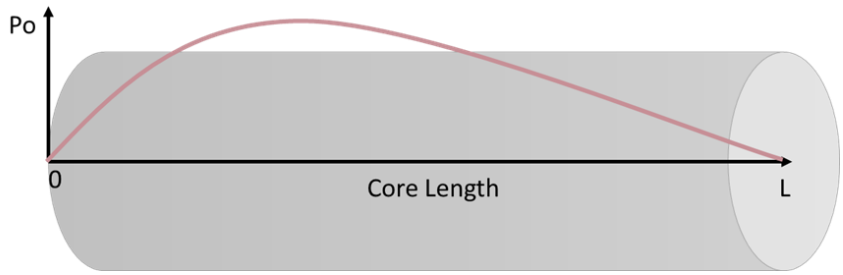

Figure 3.10 Oil phase pressure distribution for TEO free boundary condition

To obtain this boundary condition mathematically, we start with the Darcy's equation for the oil phase:

$$q_o = -\frac{k \cdot k_{ro}}{\mu_o}\frac{\partial p_o}{\partial x} \tag{3.34}$$

Thus, the oil phase pressure as a function of distance could be expressed as:

$$p_o(l) - p_o(0) = -\frac{\mu_o}{k}\int_0^l \frac{q_o(x)}{k_{ro}(x)}dx = -\frac{\mu_o}{k}\int_0^l \frac{q - q_w(x)}{k_{ro}(x)}dx \tag{3.35}$$

Also, as we know $R \equiv q/q_{w0}$ and $q_w = f_w^{\mathrm{Im}} \cdot q_{w0}$, and they are both not a function of distance, the above equation could be further expressed as:

$$p_o(l) - p_o(0) = -\frac{\mu_o q_{w0}}{k}\int_0^l \frac{R - f_w^{\mathrm{Im}}(x)}{k_{ro}(x)}dx \tag{3.36}$$

To include the boundary conditions where $p_o(l) = p_o(0)$, the mathematical expression for the outlet boundary condition should be:

$$\int_0^l \frac{R - f_w^{\text{Im}}(x)}{k_{ro}(x)} dx = 0 \tag{3.37}$$

$$R = \int_0^l \frac{f_w^{\text{Im}}(x)}{k_{ro}(x)} dx \Big/ \int_0^l \frac{1}{k_{ro}(x)} dx \tag{3.38}$$

The above equation gives a direct relationship between R value and the corresponding saturation profile. In order to apply the above boundary condition with the transient imbibition solution, we would use a strategy of using explicit R from the previous time step for the calculation of the saturation profile at the current time step. This would have removed the necessity of using iterative methods to calculate R^n implicitly. And furthermore, it will save a lot of computational time. Mathematically, Eq (3.29) will be changed to:

$$\left[\xi^{\text{Im}}\right]_i^n = \left[\xi^{\text{Im}}\right]_{i-1}^n + \frac{\Delta S_w \cdot \left[\varepsilon_D{}^{\text{Im}}\right]^n \cdot G\left(S_{w_i}\right)}{\left[f_w{}^{\text{Im}}\right]_i^n - R^{n-1} \cdot F_{w_i}} \tag{3.39}$$

And furthermore, R^n is calculated through Eq (3.38) using numerical integration techniques along with the $\left[\xi^{\text{Im}}\right]^n$ and $\left[f_w{}^{\text{Im}}\right]^n$ results from Eq (3.39). The calculated value will be used in the next time step to calculate the saturation profile.

We will show the calculation results using the model parameters as shown in Table 3.1. The results presented are at $T^{\text{Im}} = 0.2\ \text{m}^3$ and is validated with numerical simulation. Again, the bespoke simulator is used for the validation.

For the numerical simulation, we have tested the simulation under different scenarios with different cell sizes. The total length of the system is 20 meters, and has

been divided into 20, 50, 200, 500, 1000 cells, leading to cell sizes of 1, 0.4, 0.1, 0.04 and 0.02 meters per cell. The following figure shows the saturation profile from different simulations as well as the analytic solution:

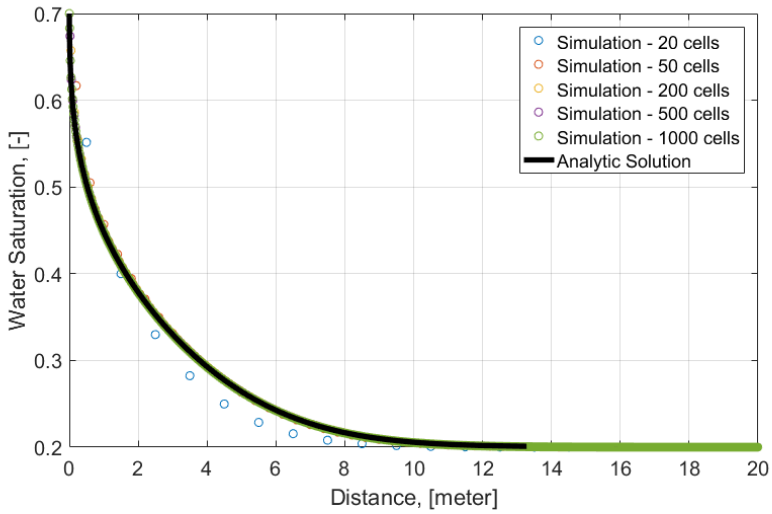

Figure 3.11 Saturation profile comparison between analytic solution and multiple numerical simulations for TEO free transient imbibition

As we can see from Figure 3.11, the analytic solution is in close agreement with the numerical simulation result at sufficiently high resolution. This has validated our analytical approach as the saturation profile is the final comprehensive result of the analytical evaluation. To show further validation of our methodology, the following figure shows the comparison of the pressure profile across the core between numerical simulation and the analytic solution:

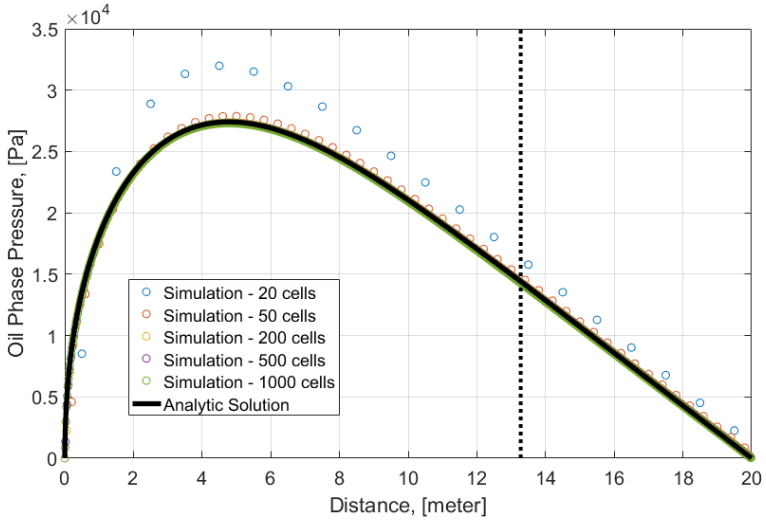

Figure 3.12 Oil phase pressure profile comparison between analytic solution and multiple numerical simulations for TEO free transient imbibition

From the above figure, it is also clear that both the numerical simulation and analytic solution have satisfied the boundary condition of the TEO free spontaneous imbibition experiment. The analytic solution's pressure profile is again in close agreement with the high-resolution simulation result. The vertical dotted line represents the location of the saturation front. As there is no mobile water to the right of this dotted line, the flow will be single phase oil flow between this location and the end of the core system, and the pressure profile will be a straight line.

To understand the actual comparison among different results, we have calculated the error (L1 norm) of all solutions between the imbibed volume given by the saturation profile and the true imbibed volume prescribed as an input. As we know the cumulative imbibed water volume is 0.2 cubic meters as an input, then we can estimate the imbibed volume from each saturation profile through numerical integration. The absolute

difference between these two values will give the error between each scenario and the true solution. The convergence test result is shown in the next figure:

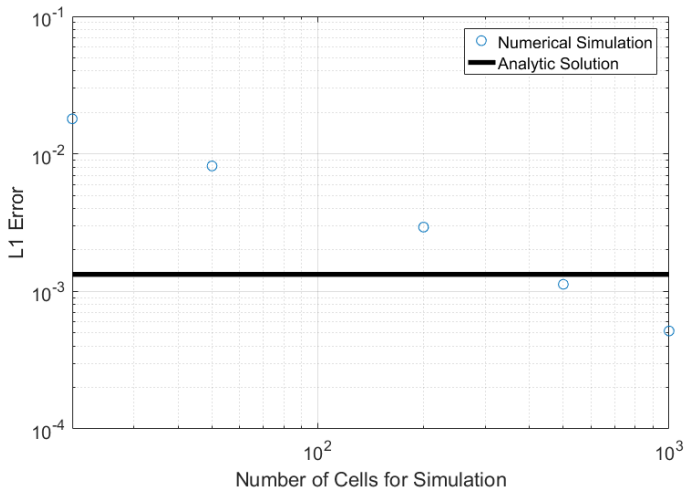

Figure 3.13 Analytic solution and numerical simulation results convergence analysis for TEO free transient imbibition

It can be observed from the above figure that the numerical simulation shows a first-order convergence rate. The analytic solution's accuracy, in this case, is approximately 450 cells for the 20-meter system, which is about 0.044 meter per cell. Ideally, this accuracy could be further improved once we increase the resolution when solving the analytic solution. The current analytic solution, which depends on finite difference method, has been discretized in T^{Im} for 50 intervals and in S_w for 500 intervals.

3.3.2 Transition from Spontaneous to Forced Imbibition and Spontaneous Imbibition Stability Envelope

Another important application of the study of spontaneous imbibition is to analyze the transition from spontaneous to forced imbibition. To better understand the transition

process, we can consider an illustrative core flood configuration as shown in the following figure:

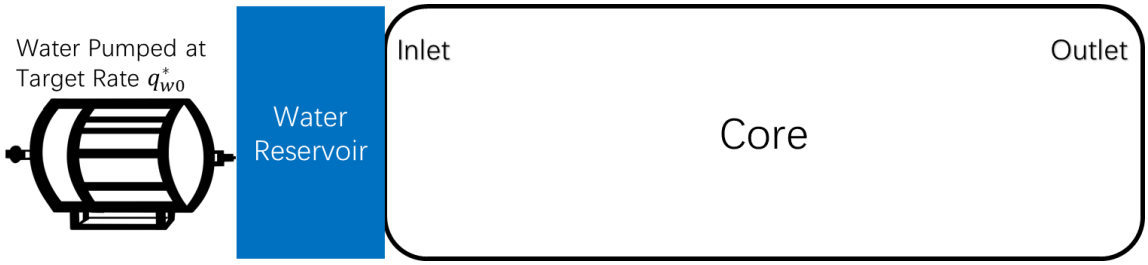

Figure 3.14 Illustration of core flood configuration to study the transition from spontaneous to forced imbibition

In this core flood example, we have a water-wet core that is constantly in contact with water at the inlet. To the left of the water reservoir at the inlet, water is also injected at a target rate q_{w0}^{*}. At the outlet, the boundary condition could be different based on the experimental set-up. Typical physical boundary conditions are discussed in the previous section. Based on the study of the imbibition solution, we know that initially the water imbibition rate is infinite. Thus, at the earlier stage, water will be sucked into the core at a rate higher than the target rate. During this state, it is the capillary pressure that prevails and mathematically the inlet boundary condition is capillary pressure equals zero. But as the imbibition rate drops, the water flux at the inlet will drop to the target rate and then the viscous pressure drop will dominate to keep the inlet water flux at the target injection rate. This process marks the transition from spontaneous to forced imbibition. This configuration describes a system where both the capillary and viscous forces are present and are constantly changing.

One important and universal relationship that applies to all spontaneous imbibition problem is the relationship between $\varepsilon_D^{\text{Im}}$ and R. For the self-similar solution, for every R value, there exists only one corresponding $\varepsilon_D^{\text{Im}}$ that matches all boundary conditions. For the transient solution, $\varepsilon_D^{\text{Im}}$ and R relationship arises as a natural consequence of the boundary conditions of the system. This characteristic relationship could be used to illustrate the behavior of the transition from spontaneous to forced imbibition. The following figure shows a typical $\varepsilon_D^{\text{Im}}$ vs. R relationship from the constant outlet flux transient imbibition problem, and it also illustrates the transition process on top of this relationship. As the value of $\varepsilon_D^{\text{Im}}$ is a natural consequence of the intrinsic properties and boundary conditions, the relationship also forms a stability envelope for spontaneous imbibition.

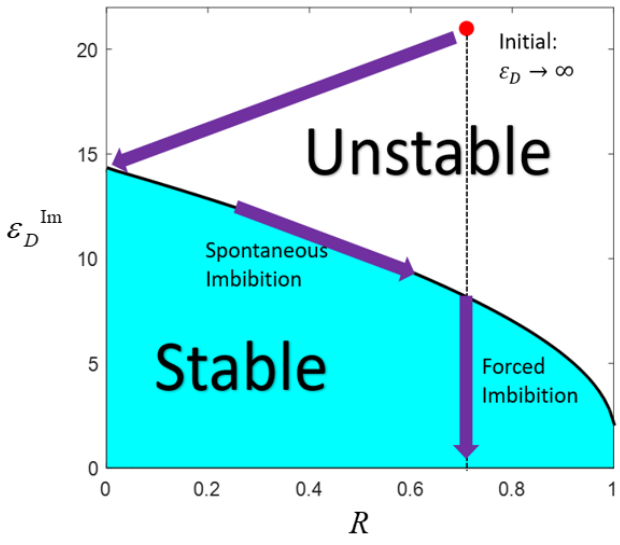

Figure 3.15 $\varepsilon_D^{\text{Im}}$ vs. R relationship (stability envelope) for constant outlet flux transient imbibition

At the initial state when we try to impose the target injection rate to the system, R will start at some finite value while $\varepsilon_D^{\text{Im}}$ will start with infinity as initially T^{Im} is very close to zero. However, this state is not stable as the capillary pressure is so high that will cause the imbibition water rate to be close to infinity, which is the same initial state as the conventional self-similar solutions. So, the $\varepsilon_D^{\text{Im}}$ will be pushed to some finite value that is determined by the rock and fluid system, and the R at the initial state will be zero due to an infinite q_{w0}. This part is represented by the first purple arrow in Figure 3.15. Then the flow will track the $\varepsilon_D^{\text{Im}}$ vs. R envelope due to spontaneous imbibition until the target injection rate q_{w0}^{*} is reached, represented by the second purple arrow in the above figure. After that the flow will be switched from spontaneous imbibition to forced imbibition once it deviates down from the $\varepsilon_D^{\text{Im}}$ vs. R envelope. During forced imbibition from the constant outlet flux transient imbibition case, R will be kept as a constant, meaning the flow is entering a steady state. But T^{Im} will continue increase, causing $\varepsilon_D^{\text{Im}}$ to decrease. This last forced imbibition state is represented by the third purple arrow in Figure 3.15.

As the above figure is only for the constant outlet flux condition, the following figure shows the comparison of the stability envelope between the three situations with physical boundary conditions as we have discussed before.

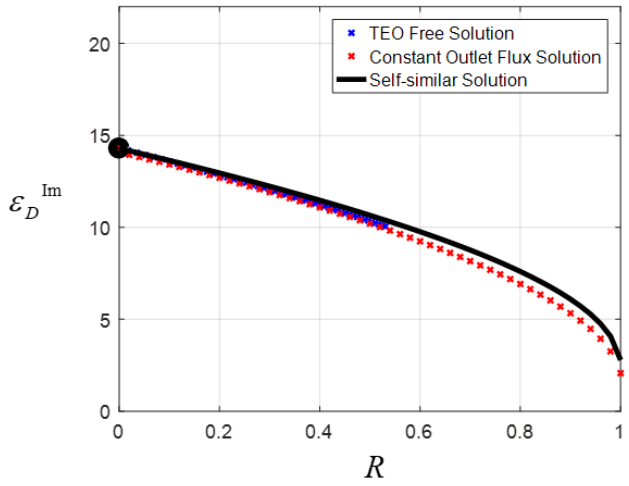

Figure 3.16 Comparison of $\varepsilon_D^{\mathrm{Im}}$ vs. R relationship between constant outlet flux transient imbibition, TEO free transient imbibition and self-similar spontaneous imbibition solutions

For the TEO free spontaneous imbibition case, the initial analysis will remain the same. Once the target injection rate is reached, the forced imbibition relationship will not stay at a constant R^*. Instead, the R value will gradually increase until 1.

As for the purely counter-current flow situation, the stability envelope reduces to a single point as we can see in Figure 3.16. For this single point, R value will remain as zero.

Another observation from Figure 3.16 is that the shape of stability envelope from all three different solutions remain identical. The stability envelope based upon the self-similar solution is a very good approximation to the more exact transient solutions. This again reminds us the statement that self-similar solution often include the essence of the more complete solutions.

Overall, in the $\varepsilon_D^{\text{Im}}$ vs. R relationship, any point above the formed envelope is unstable due to capillarity and will be pushed back onto the envelope. For all points on the envelope, it is at spontaneous imbibition state where the overall flow is capillary dominated. During this state, the solution to the system, including but not limited to the saturation profile calculation, can be obtained using the method described in this research. For all points below the envelope, it is stable and at forced imbibition state where the viscous force is more dominating. Mathematically, the major difference between the spontaneous and forced imbibition solutions lies in the inlet boundary condition. As we can see, the spontaneous imbibition has an inlet boundary condition that capillary pressure equals zero, leading to a constant saturation at the inlet. But for the forced imbibition, the closest analog would be conventional Buckley-Leverett analysis which will be achieved when $R=1$ and the inlet boundary condition will be fractional flow equals one.

3.3.3 Vertical Counter-current Spontaneous Imbibition – Analytic Solution with Gravity Effect

One of the terms we have consistently omitted in the analysis is the gravity term. Here in this section, we would like to investigate the impact of gravity for the developed analytic solution. More specifically, we will restrain our focus on the counter-current spontaneous imbibition that is performed vertically with water being imbibed from the bottom to the top. The following figure shows the illustrative configuration of the system we are going to analyze.

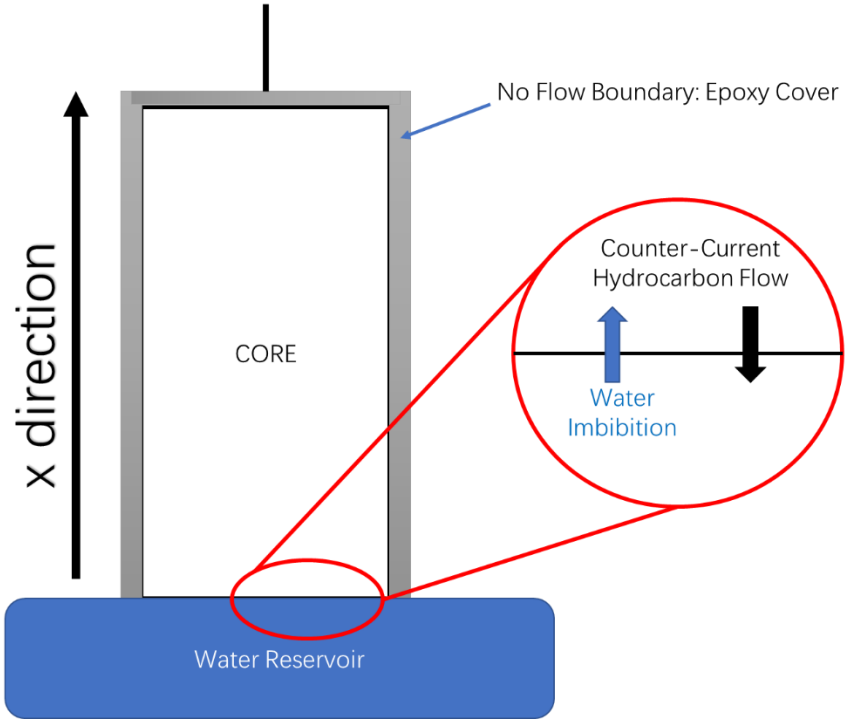

Figure 3.17 Configuration of vertical counter-current spontaneous imbibition

The above system has been reported and analyzed in the literature (Cai et al. 2012). If we consider the above system, the governing equation shown in Eq (3.3) will be changed to the following:

$$f_w^{\mathrm{Im}} = RF_w - \varepsilon_D^{\mathrm{Im}} G(S_w)\frac{\partial S_w}{\partial \xi^{\mathrm{Im}}} + \frac{\Delta\rho g A \lambda_D F_w F_o}{\mu_o q_{w0}} \tag{3.40}$$

For simplicity, we further represent the pre-factor of the gravity term with a new changed variable:

$$\delta = \frac{\Delta\rho g A \lambda_D F_w F_o}{\mu_o \varepsilon} \tag{3.41}$$

Thus, Eq (3.40) could be turned into:

$$f_w^{\mathrm{Im}} = RF_w - \varepsilon_D^{\mathrm{Im}} G(S_w) \frac{\partial S_w}{\partial \xi^{\mathrm{Im}}} + \delta \varepsilon_D^{\mathrm{Im}} T^{\mathrm{Im}} \tag{3.42}$$

From the above equation, we can see that even when R is constant (such as the purely counter-current flow case that we are going to analyze), the solution is not self-similar, and the normalized water flux will change with time. However, if we follow the strategy for the transient solution in discretizing the governing equations with respect to both T^{Im} and saturation, the solution is still well defined by finding the correct $\varepsilon_D^{\mathrm{Im}}$ for the two-point boundary value problem.

Here, we are going to show some calculation results of the purely counter-current flow case with the same parameters shown in Table 3.1. As for the gravity terms, $\Delta\rho = -200$ kg/m^3.

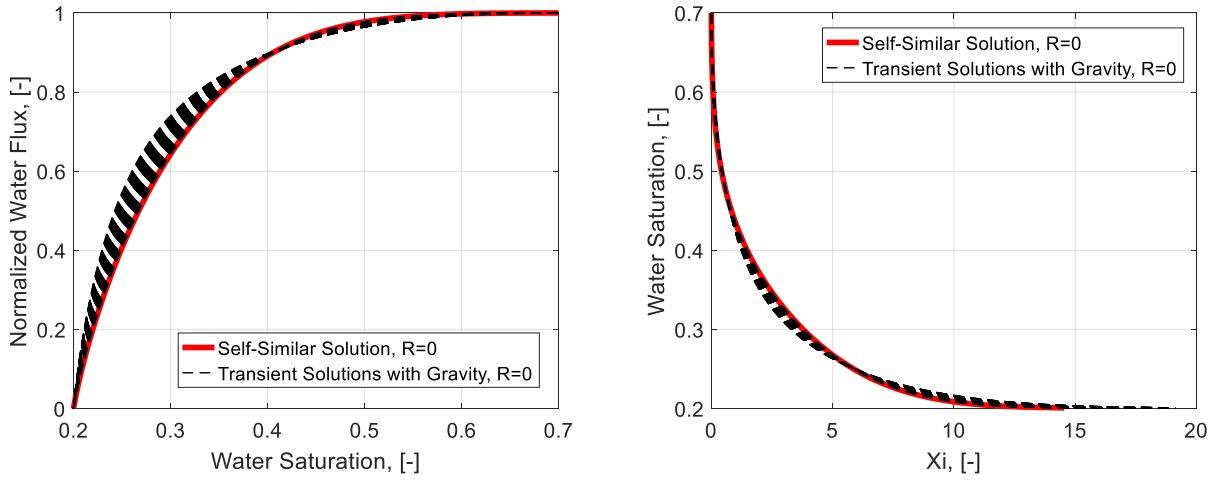

Figure 3.18 (a)-Normalized water flux comparison between the cases with and without gravity; (b)-ξ^{Im} comparison between the cases with and without gravity

The above two figures show the normalized water flux and dimensionless saturation profile at different time steps (dotted black line), and their comparison with the

results from self-similar solution neglecting gravity. Here, as δ is negative and R is zero, the denominator of the governing equation will not go to zero. So, there exists no issue with convergence in this case.

And furthermore, we are showing the saturation profiles from the cases with and without gravity at the same physical time:

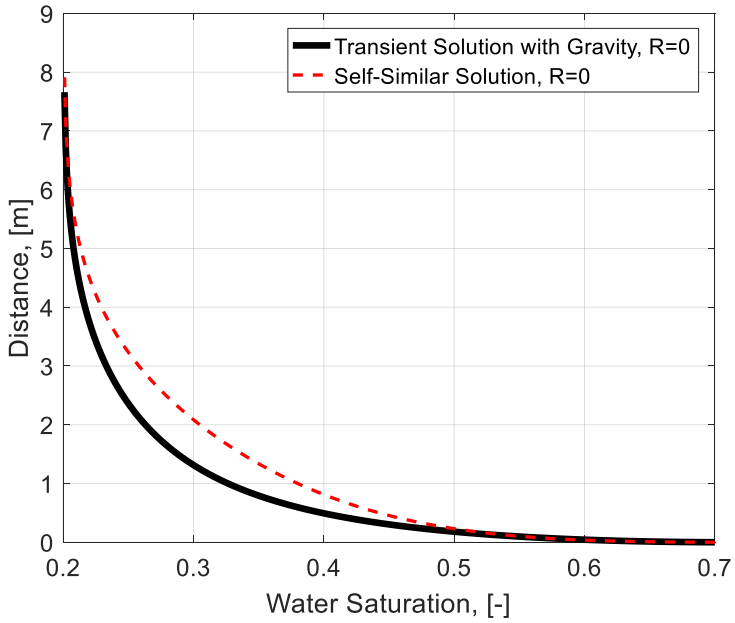

Figure 3.19 Saturation Profile comparison between the cases with and without gravity

As expected, the water imbibition will be slowed and retarded due to the gravitational force which is pointing at the opposite direction of the x axis. And we can also expect that not only the saturation profile, the produced volume and flux will all be slowed in the case with gravity. The following figure shows the comparison as well:

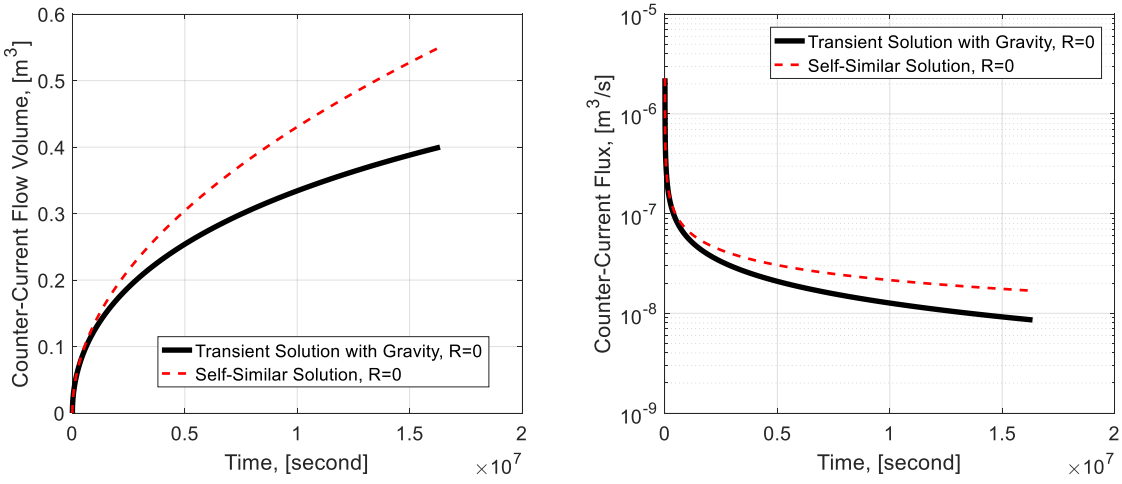

Figure 3.20 (a)-Cumulative counter-current production volume comparison between the cases with and without gravity; (b)-counter-current flux volume comparison between the cases with and without gravity

3.4 Conclusions

In this part of the research, we have reviewed the self-similar solution to spontaneous imbibition and presented a semi-analytic approach to solve the transient imbibition flow problem. The methodology of transient imbibition is the analog to the existing self-similar solution for spontaneous imbibition but is more general with less constraints and is applicable to more physical conditions. While for the self-similar solution, it only applies to the purely counter-current flow condition where either the system is semi-infinite, or the system only has one end open to flow.

On top of the analysis for the imbibition solution, by imposing a target injection rate on the inlet, the model set up made it possible to study the transition from spontaneous to forced imbibition. At initial state when capillary pressure dominates, the actual water

imbibition rate is higher than the imposed target injection rate. When the imbibition rate decreases to the target rate, the flow will enter a forced imbibition condition where the viscous pressure drop dominates. The methodology also provides a novel stability analysis to describe the transition from spontaneous to forced imbibition. The stability envelope provides a direct relationship between flow measurements and relative magnitude of capillary and viscous forces represented by a dimensionless parameter $\varepsilon_D^{\mathrm{Im}}$. This parameter is important in both viscous dominated and capillary dominated flow conditions and is a representation of the intrinsic properties of the system as well.

CHAPTER IV

SPONTANEOUS IMBIBITION IN UNCONVENTIONAL RESERVOIRS

4.1 Introduction

In the previous chapter, we have systematically studied the analytic solution to the spontaneous imbibition problems. In this chapter, we would like to apply and extend the solution we have reviewed in the previous chapter to the unconventional reservoirs with extremely low permeability.

In unconventional reservoirs, hydraulic fracturing will create a large cross-sectional area between the fracture and matrix. If the wettability is in favor of water imbibition, then the amount of water being imbibed is significant as a result of the large cross-sectional area. The following figure shows two planar hydraulic fractures and the matrix in between.

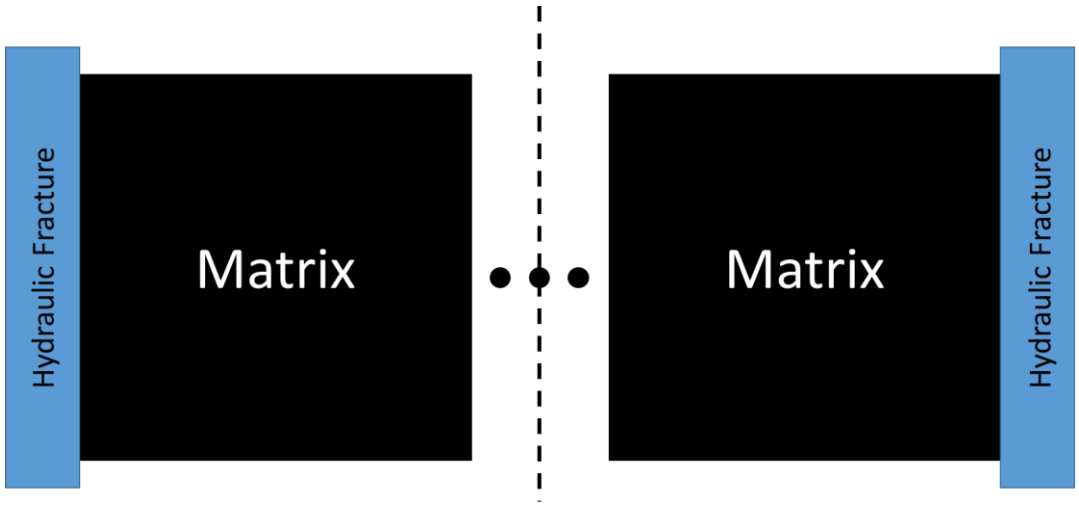

Figure 4.1 Illustration of two planar hydraulic fractures and matrix in between

If the system is homogeneous, and the two hydraulic fractures have identical properties, then the water imbibition from the fracture into the matrix will be symmetric. This phenomenon will result in a no-flow boundary at the half-length of the fracture spacing. Furthermore, the two ends will both have purely counter-current spontaneous imbibition, which is represented by the self-similar solution described in the previous chapter.

We applied the self-similar solution with some typical reservoir properties' values from a dry gas shale reservoir, and the parameters are showing in the following table. The relative permeability and Leverett J-function still follow the functional forms shown in Eq (3.5), Eq (3.6) and Eq (3.7).

Rock Properties		Water Relative Permeability and Fluid Properties		Gas Relative Permeability and Fluid Properties		Capillary Pressure	
$\boldsymbol{k}$	1.97E-19 m^2 (200 nD)	β_w	2	β_g	2	β_c	1
ϕ	0.1	S_{wirr}	0.2	S_{grw}	0.25	J_c	1
S_{wi}	0.2	μ_w	0.001 $Pa \cdot S$	μ_g	1.5E-5 $Pa \cdot S$	S_{w0}	0.7
		$k_{rw}^{\max}$	0.6445	$k_{ro}^{\max}$	1	p_c^*	$\sigma\sqrt{\phi/k}$
						σ	0.05 N/m

Table 4.1 Model input parameters for example calculations of spontaneous imbibition in unconventional reservoirs

As for the hydraulic fracture's design and geometry, the following table summarizes all the input parameters' values.

ϕ_{frac}	0.6	h_{frac}	60.96 m (200 ft)
x_f	152.4 m (500 ft)	D_{frac}	152.4 m (500 ft)
d_{frac}	0.0610 m (0.2 ft)		

Table 4.2 Input parameters for hydraulic fractures' design and geometry.

In the above table, ϕ_{frac} denotes the fracture porosity, h_{frac} denotes the fracture height, x_f denotes the fracture half-length, D_{frac} denotes fracture spacing and d_{frac} denotes the fracture aperture. If we assume one-dimensional counter-current spontaneous imbibition happens at the fracture-matrix interface, with the above illustrated properties, we can obtain the production result and water imbibition profile as shown in the following figure.

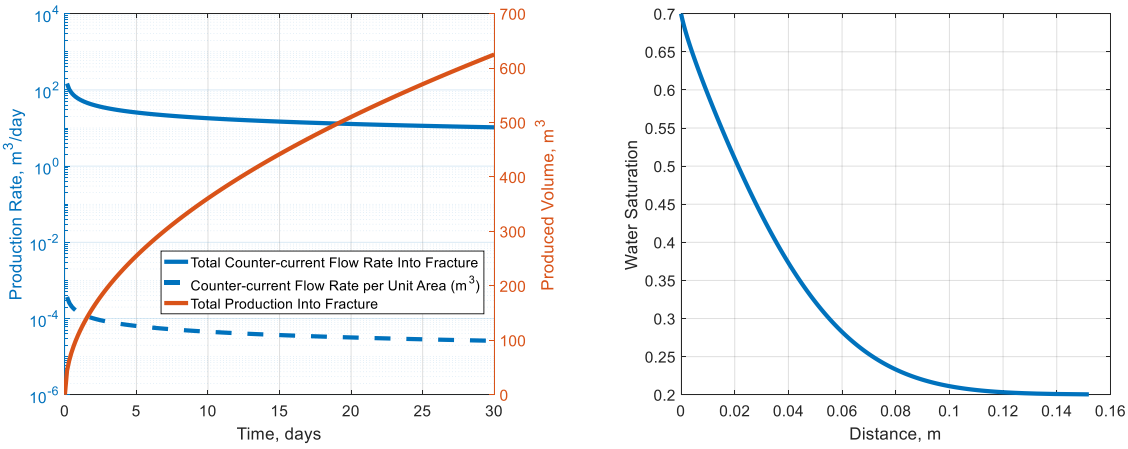

Figure 4.2 Example calculation of hydrocarbon production and water imbibition profile for unconventional reservoirs

When comparing the gas production rate and gas production rate per unit area in the above figure, our previous statement that the counter-current production rate is

significant due to the larger cross-sectional area is proved. And due to the low permeability for these unconventional reservoirs, such counter-current flow rate is much higher compared with what is achievable from viscous pressure drop, especially at the early time. Also, the saturation profile at 30 days is shown in the above figure as well. This figure shows that the water invasion is not significant as the water front only advanced 0.15 ft, which is less than 0.1% of the fracture spacing.

The above illustrative calculation has shown that the counter-current flow due to spontaneous imbibition in unconventional reservoirs may be beneficial for hydrocarbon production at the early time. And for the traditional "water blocking" concept, which states that the invaded water will lower the hydrocarbon phase mobility, it may not be significant considering the short water front distance. This has led us to think about the contradiction between the "water blocking" theory and the field operation convention where operators tend to soak their wells after hydraulic fracturing for better initial gas production. In the next section, we will theoretically analyze this problem and provide a quantitative evaluation of this trade-off.

4.2 Spontaneous Imbibition and Water Adsorption – Sub-irreducible Initial Water Saturation Condition

Before going into the detail about the investigation of "water blocking" effect, we noticed that there was literature discussing shale reservoirs exhibiting sub-irreducible initial water saturation conditions. At the interval between initial water saturation and

irreducible water saturation, the water is theoretically not able to flow but is being controlled by adsorption due to the presence of clay minerals. In this section, we would like to first try to combine the spontaneous imbibition and water adsorption below irreducible water saturation together at the continuum scale to extend the analytic solution's applicability.

In between the region between initial water saturation and irreducible water saturation, the water relative permeability remains zero and the gas relative permeability is still finite. From Eq (3.11), for the water saturation range $S_{wirr} \le S_w \le S_{w0}$, the differential equation is degenerate parabolic. While in the range $S_{wi} \le S_w \le S_{wirr}$, the equation turns into hyperbolic with $G(S_w)$ being constantly zero. This form of the equation supports the saturation shocks.

The system still has the original boundary conditions where $S_w = S_{w0}$, $\xi^{\mathrm{Im}} = 0$ and $f_w^{\mathrm{Im}} = 1$ for a specified S_{w0} at which the capillary pressure goes to zero at the inlet. At the foot of the saturation profile, we have $S_w = S_{wi}$, $f_w^{\mathrm{Im}} = 0$ at a location where $\xi^{\mathrm{Im}} = c$. The main change for the sub-irreducible initial saturation condition is that there exists another shock saturation S_w^* which will satisfy the continuity condition. Consider a discontinuity in the solution at $x = l(t)$ and the speed of this location is the same as the frontal speed c because of the shock construction. We can express the solution in terms of "left" and "right" solutions using the Heaviside function Θ.

$$S_w^{\,*}(x,t) = S_w^{\,left} \cdot \Theta\left(l(t) - x\right) + S_w^{\,right} \cdot \Theta\left(x - l(t)\right) \tag{4.1}$$

$$q_w(x,t) = q_w^{\,left} \cdot \Theta\left(l(t) - x\right) + q_w^{\,right} \cdot \Theta\left(x - l(t)\right) \tag{4.2}$$

The weak continuity condition is obtained at $x = l(t)$:

$$-\phi c\left[S_w\right] + \left[q_w\right] = 0 \tag{4.3}$$

Here the difference between the normalized water flux to the right and left of the discontinuity is $\left[f_w^{\,\mathrm{Im}}\right] = f_w^{\,\mathrm{Im},right} - f_w^{\,\mathrm{Im},left}$. If $\left[S_w\right] \to 0$ and $\phi c = \lim_{[S_w]\to 0} \left[q_w\right] / \left[S_w\right]$. The entropy condition states that if there are multiple possible shock solutions, the one with the fastest speed arises physically. In the current case with the capillary dominated flow, we will have the following differential equation as the continuity condition:

$$\phi c = \phi \frac{\partial x}{\partial t} = \frac{q_w\left(S_w^{\,*}\right)}{S_w^{\,*} - S_{wi}} = \frac{\partial q_w\left(S_w^{\,*}\right)}{\partial S_w^{\,*}} \tag{4.4}$$

$$\frac{\left[f_w^{\,\mathrm{Im}}\right]}{\left[S_w\right]} = \xi^{\mathrm{Im}} = \frac{df_w^{\,\mathrm{Im}}}{dS_w} \tag{4.5}$$

The above equation is indicating that straight line slope to the left of the shock saturation should be the same as the slope to the right of the shock saturation on the normalized water flux plot. The solution to the differential equation (in Lagrangian form) has $d\xi^{\mathrm{Im}} / dS_w = 0$ and $d^2 f_w^{\,\mathrm{Im}} / dS_w^{\,2} = 0$ below irreducible water saturation. Thus, the normalized water flux trajectory for the range of $S_{wi} \le S_w \le S_{wirr}$ will be a straight line and the slopes will be given by the value of ξ^{Im} at irreducible water saturation.

As the solution used here is the $R=0$ self-similar solution for the representation of the purely counter-current flow condition, the solution strategy is still the shooting method for the two-point boundary value problem. The governing equations in their discretized form are shown in Eq (3.15) and Eq (3.16). The following figure shows the typical cases that will happen during the shooting process. In this example calculation, all input parameters are the same as shown in Table 4.1 except that $S_{wi}=0.15$, and this change applies to all subsequent illustrative calculations.

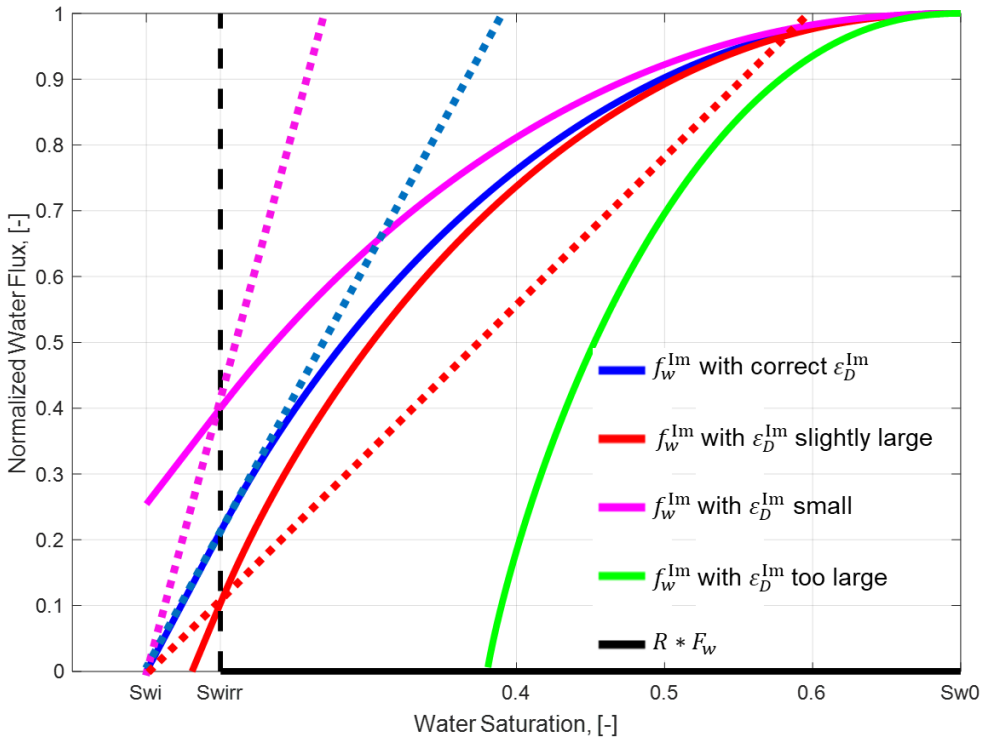

Figure 4.3 Normalized water flux shooting results with sub-irreducible initial water saturation

As we can see from the above figure, there are typically four types of outcome from the shooting algorithm for the normalized water flux. Only the blue curve with the correct $\varepsilon_D^{\text{Im}}$ value will satisfy the foot boundary condition. When $\varepsilon_D^{\text{Im}}$ is smaller than the correct value, the f_w^{Im} trajectory will end at a value higher than zero at the initial water saturation, and it is not physically possible as this condition indicates water movement at the initial water saturation. When $\varepsilon_D^{\text{Im}}$ is slightly larger, but still satisfy the condition where $f_w^{\text{Im}} > RF_w$, the trajectory will terminate at the saturation higher than S_{wi}. Finally, if the tested $\varepsilon_D^{\text{Im}}$ is too large, the normalized water flux trajectory will intersect with the $R \cdot F_w$ curve, causing $f_w^{\text{Im}} - R \cdot F_w = 0$ and the differential equation to diverge. The three dash lines represent the shock construction for $S_{wi} \le S_w \le S_{wirr}$ region for the corresponding three f_w^{Im} trajectories. It is clear that only the blue curve has both a continuous normalized water flux and continuous shock speed.

Another observation from the above figure is that for the cases where $\varepsilon_D^{\text{Im}}$ is too large, there still exists a shock saturation greater than the irreducible water saturation that will also form a concave envelope. We elaborate this behavior using the following figure:

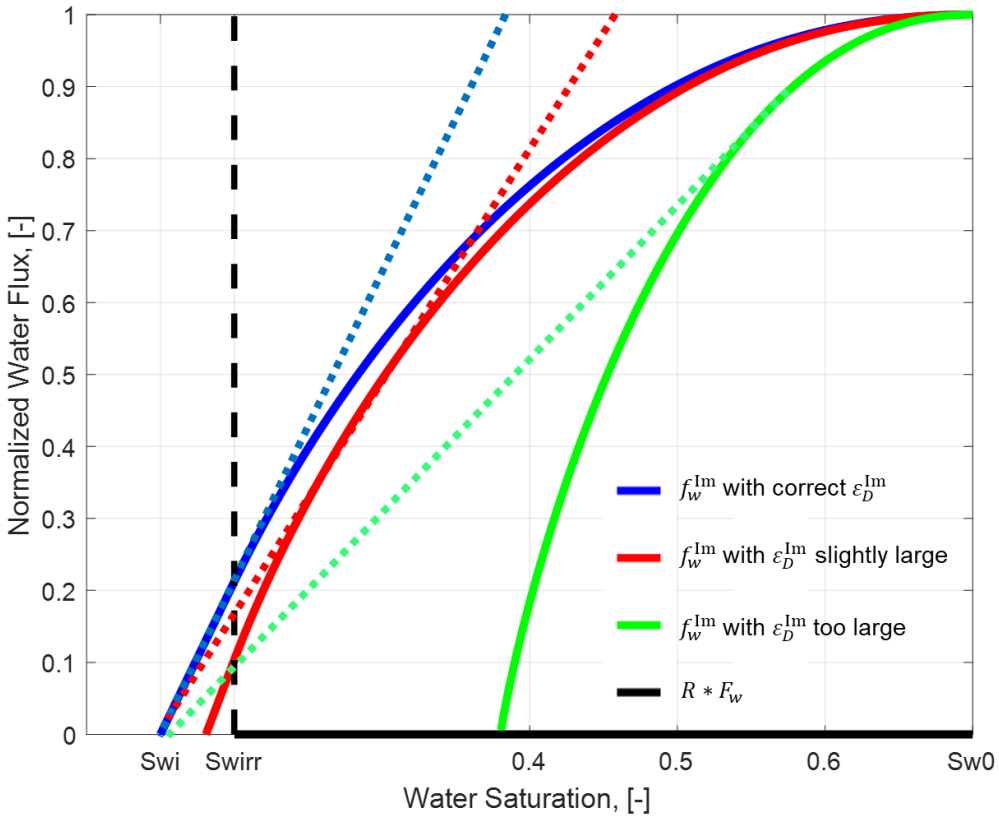

Figure 4.4 Normalized water flux shooting results with correct and large $\varepsilon_D^{\mathrm{Im}}$ values, and corresponding concave envelope of the normalized water flux

In the above figure, the red and green dash line represents the straight-line portion for the concave envelope of the normalized water flux for large $\varepsilon_D^{\mathrm{Im}}$ values. For these trajectories, the calculated concave envelope shock solution is at a value larger than S_{wirr}. But compared with the blue f_w^{Im} curve that is implicitly concave down and $S_w^* = S_{wirr}$, these two shock speeds are both smaller. This brings up the importance of the uniqueness of the entropy condition where the fastest speed shock solution will exist physically. Thus, the blue curve is the resulting solution for the spontaneous imbibition problem with initial

saturation being sub-irreducible. This completes our analytic solution for spontaneous imbibition with water adsorption for sub-irreducible flow, and it could certainly be extended to the transient imbibition solution as well.

4.3 Gravity Segregation in Hydraulic Fractures

The other constraint we are imposing for the analysis of the "water blocking" effect is the gravity segregation happening inside the fracture. In the above methodology for spontaneous imbibition, one major assumption is that the inlet is always constantly in contact with water. But in the case of fracturing fluid being imbibed into the rock matrix, the counter-currently produced hydrocarbon will take a portion of the volume of the fracture at the top, leading to the cessation of spontaneous imbibition at the top of the fracture face. This is illustrated in the following figure:

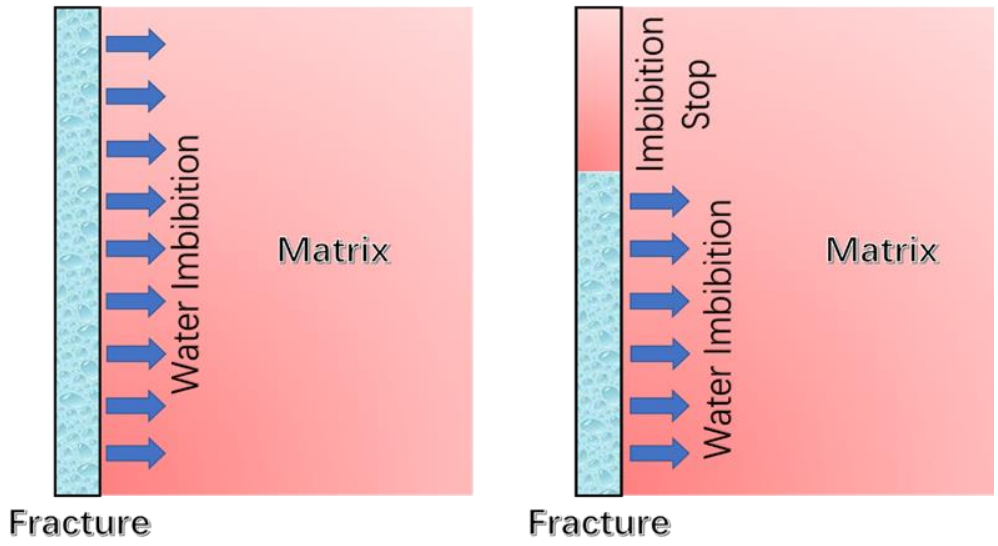

Figure 4.5 Illustration of the impact from gravity segregation on water invasion from fracture to matrix

As normally the fracture with proppant will have high conductivity, even in the vertical direction, we are assuming instantaneous segregation within the fracture. Thus, the following relationship applies to the volume change within the fracture:

$$\frac{dQ}{dt} = 2 \cdot u^{\mathrm{Im}} \cdot A_{open} \tag{4.6}$$

In the above equation, the term Q denotes the counter-current produced volume of gas going inside the fracture or the water suction volume from the fracture into the matrix. The u^{Im} is the Darcy velocity of the imbibition rate, and according to the self-similar solution, the value is determined by $C^{\mathrm{Im}}/\sqrt{t}$ where C^{Im} is an intrinsic constant. The A_{open} is the fracture surface area that is currently open for imbibition (the area that is still in contact with water). The pre-factor 2 represents the counter-current hydrocarbon flow from both sides of the fracture surface. According to the volume conservation of the pore volume within the fracture:

$$A_{open} = \frac{\dfrac{V_{frac}}{\phi_{frac}} - \dfrac{Q}{\phi_{frac}}}{D_{frac}} = \frac{2x_f h_{frac} D_{frac} \phi_{frac} - Q}{\phi_{frac} D_{frac}} = 2x_f h_{frac} - \frac{Q}{\phi_{frac} D_{frac}} \tag{4.7}$$

In the above equation, the term V_{frac} represents the fracture bulk volume. By combining Eq (4.6) with Eq (4.7), we have:

$$\frac{dQ}{dt} = 2 \cdot u^{\mathrm{Im}} \cdot \left(2x_f h_{frac} - \frac{Q}{\phi_{frac} D_{frac}} \right) = \frac{2C^{\mathrm{Im}}}{\sqrt{t}} \left(2x_f h_{frac} - \frac{Q}{\phi_{frac} D_{frac}} \right) \tag{4.8}$$

$$-\frac{\phi_{frac} D_{frac}}{2C^{\mathrm{Im}}} \ln\left(4C^{\mathrm{Im}} x_f h_{frac} - \frac{2C^{\mathrm{Im}}}{\phi_{frac} D_{frac}} Q \right) = 2\sqrt{t} + \gamma \tag{4.9}$$

From Eq (4.9), if $t \to \infty$, we have the part inside the natural logarithm being equal to zero. This, in turn, determines the limit of Q at infinite time would be equal to $2x_f h_{frac} D_{frac} \phi_{frac}$, which is the pore volume of the fracture. Thus, the asymptote of the cumulative production curve would be the pore volume of the fracture during soaking.

The other problem is the calculation of the constant value γ in Eq (4.9). As there might have been some leak off before the shut-in period, for example during the fracturing process when water is continuously pumped into the formation while imbibition is happening simultaneously, the starting time of this calculation t^* at which $Q = 0$ may not be exactly $t = 0$. For the sake of simplicity, we will assume the t^* time is right after the hydraulic fracturing process is finished and shut-in period happens thereafter, thus we can calculate the constant's value in Eq (4.9):

$$\gamma = -\frac{\phi_{frac} D_{frac}}{2C^{\mathrm{Im}}} \ln\left(4C^{\mathrm{Im}} x_f h_{frac} \right) - 2\sqrt{t^*} \tag{4.10}$$

For these water-wet systems, we will consider only spontaneous water imbibition and adsorption during the fracturing process, and the forced imbibition is not present. The reason is that the spontaneous imbibition and adsorption induced water flux will be much larger than the flux a viscous pressure drop could have achieved at the early time, and for unconventional shale systems with ultra-low permeability this phenomenon is more

obvious. The detailed explanation on this matter could be found in one of our previous research papers (Deng and King 2018). Finally, we will have the expression for the counter-currently produced hydrocarbon volume as a function time:

$$-\frac{\phi_{frac}D_{frac}}{2C^{\mathrm{Im}}}\ln\left(4C^{\mathrm{Im}}x_f h_{frac}-\frac{2C^{\mathrm{Im}}}{\phi_{frac}D_{frac}}Q\right)=2\sqrt{t}-2\sqrt{t^*}-\frac{\phi_{frac}D_{frac}}{2C^{\mathrm{Im}}}\ln\left(4C^{\mathrm{Im}}x_f h_{frac}\right) \tag{4.11}$$

$$Q=2x_f\phi_{frac}D_{frac}h_{frac}-\frac{\phi_{frac}D_{frac}}{2C^{\mathrm{Im}}}\exp\left[\frac{4C^{\mathrm{Im}}}{\phi_{frac}D_{frac}}\left(\sqrt{t^*}-\sqrt{t}\right)+\ln\left(4C^{\mathrm{Im}}x_f h_{frac}\right)\right] \tag{4.12}$$

From Eq (4.12), the actual counter-current imbibition rate with gravity segregation in fracture could easily be calculated by taking the derivative of Q with respect to time. And also, based on the interpretation from Figure 4.5, it is trivial that the upper part of the matrix should have less water invasion and the lower portion should have more invasion.

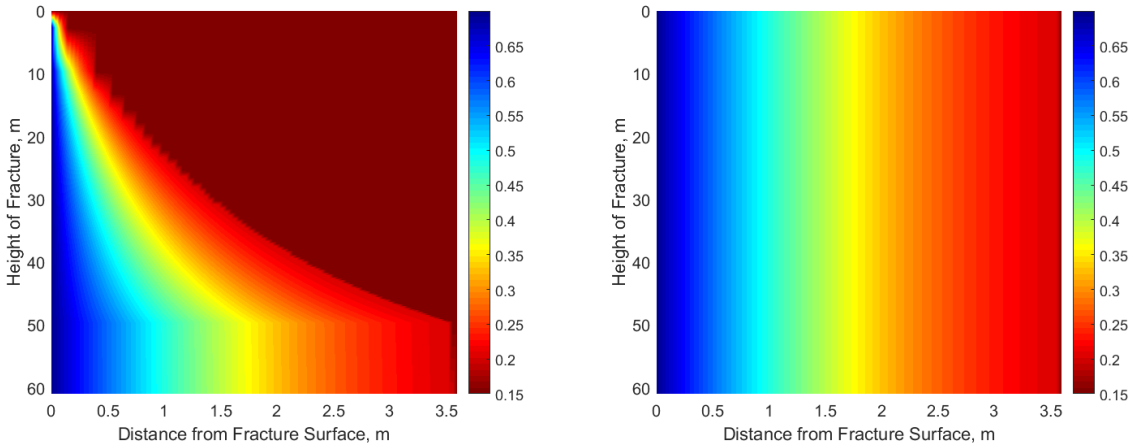

Figure 4.6 (a)- Water saturation profile with gravity segregation; (b)-water saturation profile without gravity segregation

From the above figures, we can see the difference between the cases with and without gravity segregation on the water invasion / water saturation profile. The main difference, as explained, is that the water invasion in the upper portion of the matrix is smaller than the water invasion at the bottom where the fracture surface is still in contact with water. With this saturation profile, we could evaluate the impact of water invasion.

To quantitatively evaluate the water invasion's impact, we would like to evaluate the apparent mobility of the gas phase and its change with time. With any saturation profile calculated as shown in Figure 4.6a, we can calculate have the following equation for the gas production rate:

$$q_g = \sum_{j=1}^{n} q_{g_j} = \sum_{j=1}^{n} \frac{kA_j \Delta p}{\mu_g \left[\int_{x=0}^{D_{frac}/2} 1/k_{rg}\, dx \right]_j} = \frac{2k\overline{k_{rg}} A \Delta p}{\mu_g D_{frac}} \tag{4.13}$$

In the above equation, the term j represents the discretization in the vertical direction. And the summation of the flow rates from each vertical incremental cross-sectional area would give us the total flow rate. Thus, we can have the representation of the apparent gas phase relative permeability with water invasion:

$$\overline{k_{rg}} = \sum_{j=1}^{n} \frac{A_j D_{frac} / 2}{A \left[\int_{x=0}^{D_{frac}/2} 1/k_{rg}\, dx \right]_j} \tag{4.14}$$

The above equation would give us the indication about the apparent average relative permeability $\overline{k_{rg}}$ or its corresponding mobility for the gas phase. This value will be used to evaluate the damage that the invaded water has brought to the flow of the gas

phase. It is obvious that as the water invades deeper into the matrix, the $\overline{k_{rg}}$ will become smaller and smaller. And for a strongly water-wet system where the gas relative permeability value is close to zero at the inlet saturation, the apparent relative permeability or mobility will be equivalently zero as well.

4.4 "Water Blocking" due to Spontaneous Imbibition and Water Adsorption

As we have shown in the previous section that the water invasion will cause the mobility to the gas phase to drop, but the field operation observations are stating that the water invasion into the matrix will benefit the gas production. We believe the trade-off lies in the difference between the counter-current gas flow rate due to spontaneous imbibition and adsorption and the achievable viscous gas production rate. Or in other words, is the water invasion caused by spontaneous imbibition and water adsorption really a production mechanism or a blocking mechanism?

As the spontaneous imbibition and adsorption mechanism will have a counter-current flow rate starting at infinity, at early stage the gas flow rate caused by this phenomenon will be higher than the achievable production rate supported by the viscous pressure drop. Thus, as a short-term criterion, the guideline for the length of the soaking period should really depend upon which flow rate controlled by the above two mechanisms would yield a higher production. Also, in the long-term, longer soaking should really be beneficial to have more gas and less water residing inside the fracture, and this will be the main driver to have higher initial gas production rate after the soaking

period. The other benefits would be to reduce the liquid loading in the fracture, to reduce the relative permeability effect inside the fracture and so on. In this following section, we will use the parameters showing in Table 4.1 and Table 4.2 as a test case to show both the short-term and long-term impact from well soaking. The changes here is still that $S_{wi} = 0.15 < S_{wirr}$ to show the effect from water adsorption. Also, according to the normal single stage hydraulic fracturing operation convention, we chose the t^* value to be two hours. The calculation period for this case is 6 months. The following figure shows the calculation results of the effective height reduction along with time. It also shows the comparison of the cumulative counter-current production volume between the one-dimensional self-similar solution and the case with gravity segregation in the fracture.

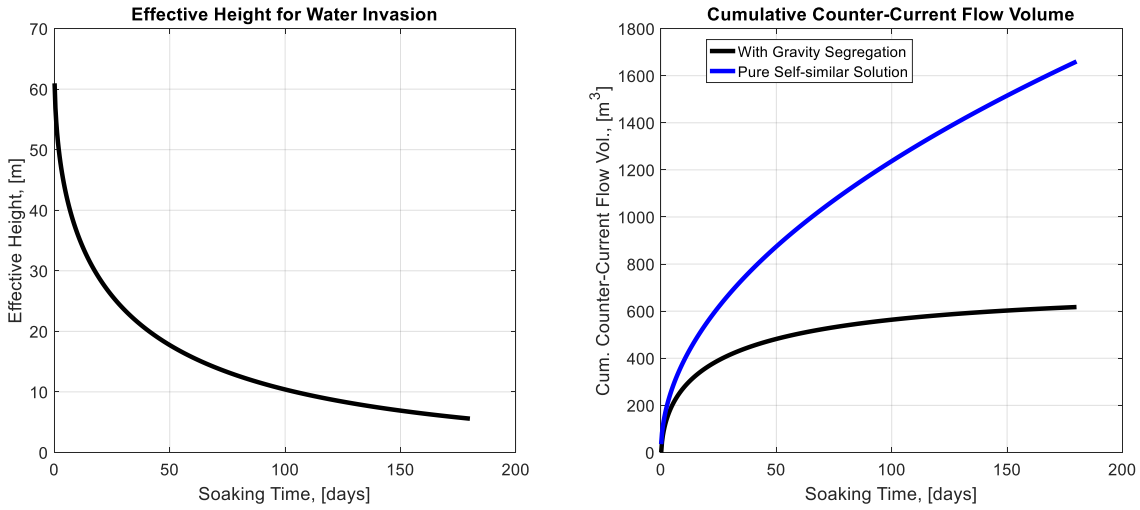

Figure 4.7 (a)- Effective height in contact with water decreasing with soaking time; (b)-cumulative counter-currently produced volume predicted by purely self-similar solution and the solution with gravity segregation

As we can see from Figure 4.7a that as soaking time increases, the effective portion of fracture height that opens for imbibition and adsorption is decreasing. This leads to the

result shown in Figure 4.7b where the production with gravity segregation will be smaller compared with the pure self-similar solution. As we have introduced, the limit of counter-current flow volume in the gravity segregation case will be the pore volume inside the fracture.

Also, according to the estimation of the water blocking side, we can estimate the apparent average gas relative permeability and its decline with respect to time.

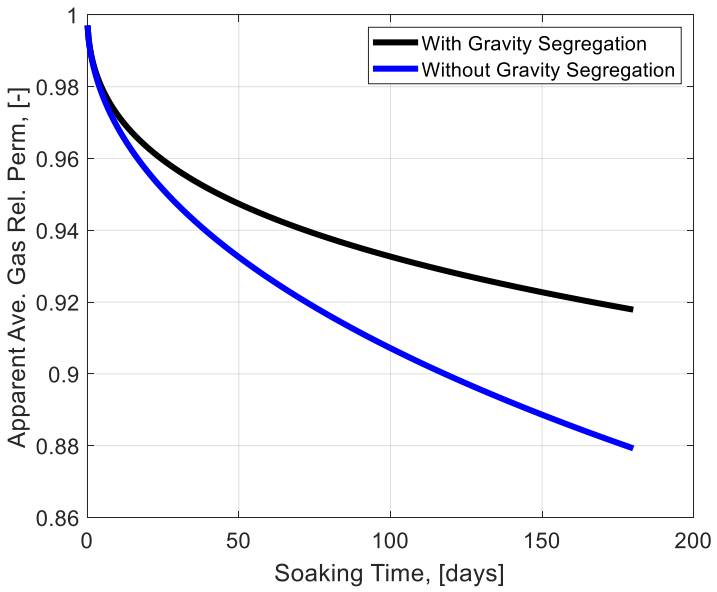

Figure 4.8 Apparent average gas phase relative permeability decreasing with increasing soaking time

In the above figure, we can see that in the current setting the water blocking is increasing along with time. If we compare the resulting apparent gas relative permeability between the cases with and without gravity segregation, as expected, the case without gravity segregation will yield a faster gas phase mobility decline as shown in the above figure. Another point to mention is that the initial apparent relative permeability is not 1

in Figure 4.8 is due to the fact that the leak off during the fracturing process itself, although a very short period, would have already caused some damage on the gas phase mobility. With the calculation result from Figure 4.8, the achievable viscous production rate could be estimated by applying a pressure drop. The pressure drop here is with respect to the gas phase pressure drop and the value we used, in this case, is 1000 psi. Then if we compare this production rate with the corresponding production rate from Figure 4.7b, we will have the following plot:

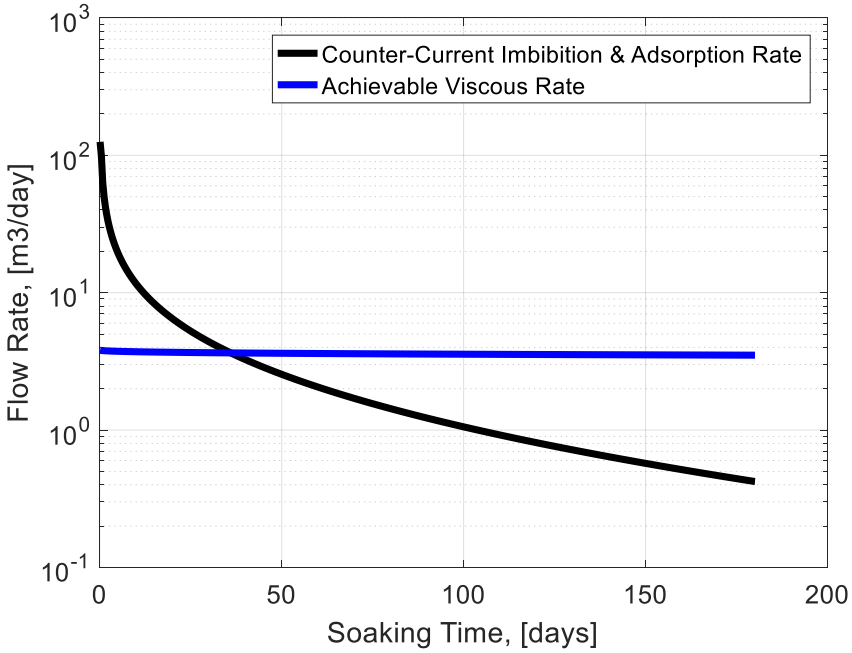

Figure 4.9 Calculation of cross-over time for well soaking

From the above figure, we can see the counter-current gas flow rate assisted by spontaneous imbibition and water adsorption will be a lot higher in the early period of time. But it is also dropping very fast, especially when compared with the achievable viscous flow rate reduction due to mobility-related water blocking effect. In other words,

the water blocking effect seems not strong compared with the imbibition and water adsorption rate. Also, the time where these two flow rates cross should be the best time interval for the well soaking period. For any soaking time before this time, the counter-current imbibition and water adsorption associated production will be higher than what we can achieve by lowering the BHP. Hence, for the interval before the cross-over time, the imbibition and adsorption of water should be considered as a production mechanism. However, after the cross-over time, any more water invasion will not be giving more gas flow rate contribution and the water is now acting as a blockage in the matrix. For this base case we are studying here, the cross-over time is about 859 hours, which is close to 36 days.

The above criterion is only for short-term well soaking management purpose. In a long-term sense, the water blocking effect caused by the apparent gas mobility reduction, although small, is still present. Then we can evaluate the long-term effect from well soaking by evaluating the ratio between total volume produced by counter-current imbibition and adsorption assisted flow during the soaking and the flow rate reduction caused by water blocking. And this ratio is the compensation time that could be used to represent the counter-current flow's long-term contribution to compensate the penalty caused by the water invasion.

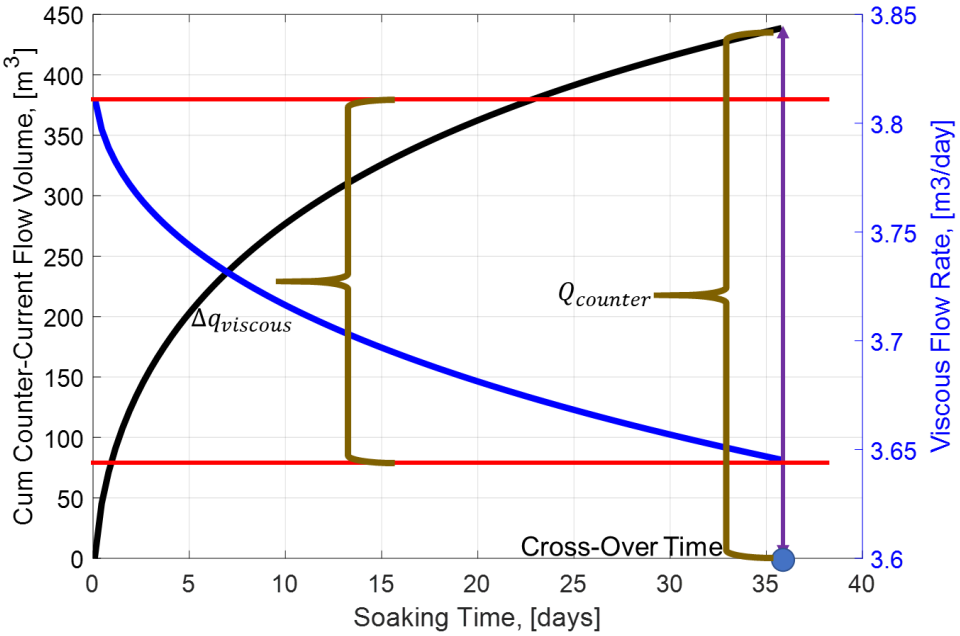

Figure 4.10 Illustration of the concept for calculating the compensation time

In this particular case, the compensation time is around 2637 days, which is about 7.2 years. This again proves that the initial high counter-current flow rate caused by spontaneous imbibition and water adsorption could really benefit the overall well performance, compared with the damage that water invasion could have caused. And this is the reason why we could see higher initial gas production after soaking as there has been more gas being expelled into the fracture during the soaking period.

To better understand the impact of the "water blocking" effect as well as the soaking process itself, we are performing more sensitivity analysis to investigate the impact from certain key parameters in order to further understand the applicability of the above analysis. The key parameters that are included in the sensitivity analysis are the matrix absolute permeability, matrix porosity, fracture spacing, fracture porosity, fracture

width, pressure drop during production phase and the J_c value which represents the strength of the capillary pressure. Using the values provided in Table 4.1 and Table 4.2 as the base case, the sensitivity analysis will perturb the parameter's value by plus/minus fifty percent individually and compare the cross-over time and compensation time results.

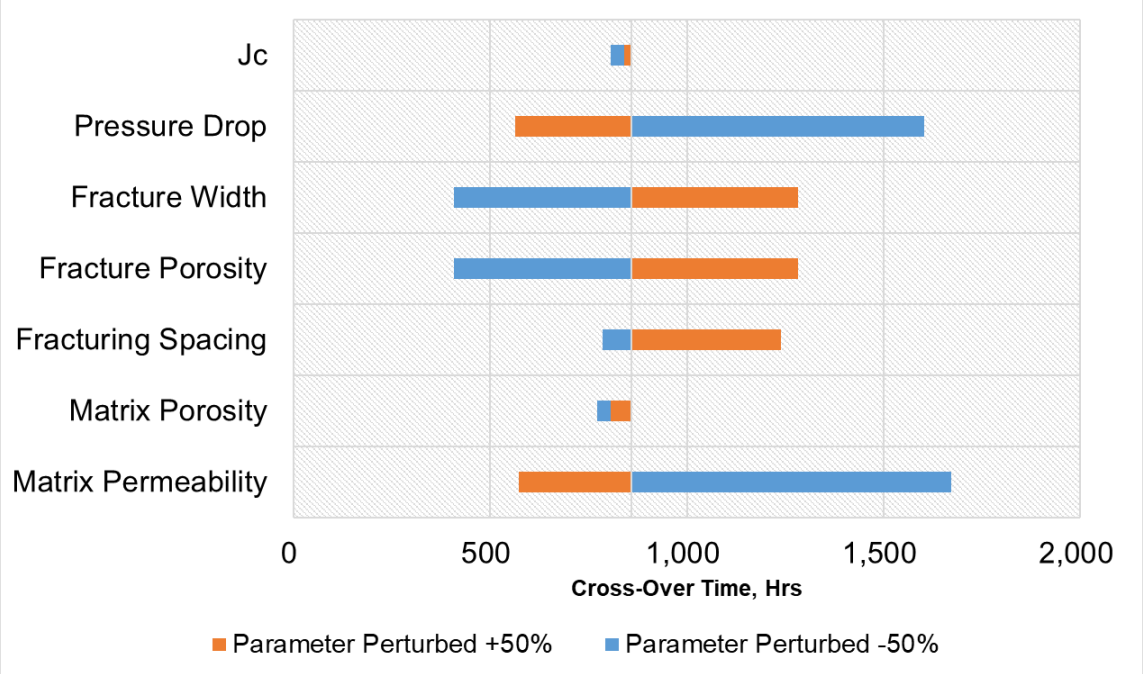

Figure 4.11 Sensitivity analysis of cross-over time

The above figure shows the sensitivity analysis of the different parameters on the cross-over time. The dominating parameters are the matrix permeability and the pressure drop during the production phase. Both two parameters are directly related to the achievable viscous flow rate. The matrix permeability, to some extent, is also related to the strength of capillary pressure as defined in Leverett-J function. The fracture width and fracture porosity are also very important as they control the total pore volume within the fracture, which further impacts the closure of the cross-sectional area open for imbibition.

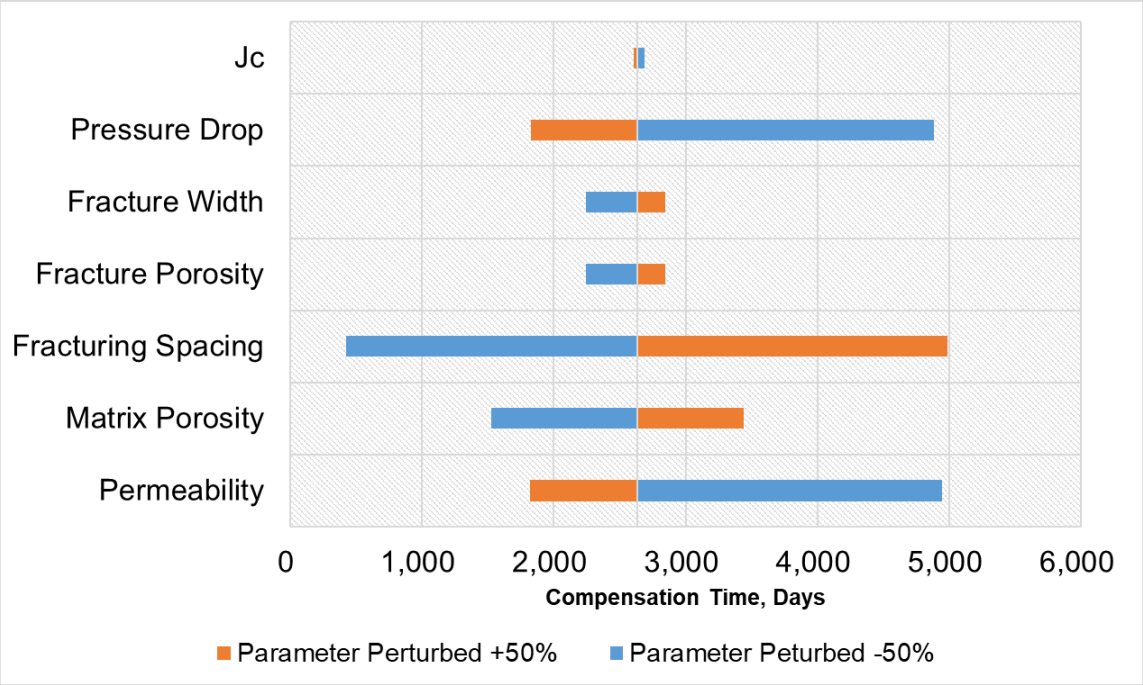

Figure 4.12 Sensitivity analysis of compensation time

The above figure shows the sensitivity analysis of the different parameters on the compensation time. The main difference for the compensation time calculation is that it already includes the carried-on sensitivity from the cross-over time. The compensation time is calculated until the cross-over time for each individual case.

There are also other types of sensitivity analysis that are more related to the qualitative description of the rock and fluid system itself. These include the wettability of the system as well as the hydrocarbon type of being gas or oil. In this section, in order to simplify the problem, we are using the S_{w0} value to represent the change in wettability. When the value of S_{w0} is closer to one minus the residual hydrocarbon saturation, the system is generally more water wet. In the base case, the system could be considered as a

relatively strongly water-wet case, and we would like to compare the results with a case that is less water-wet. In this case, the new value of S_{w0} is 0.5.

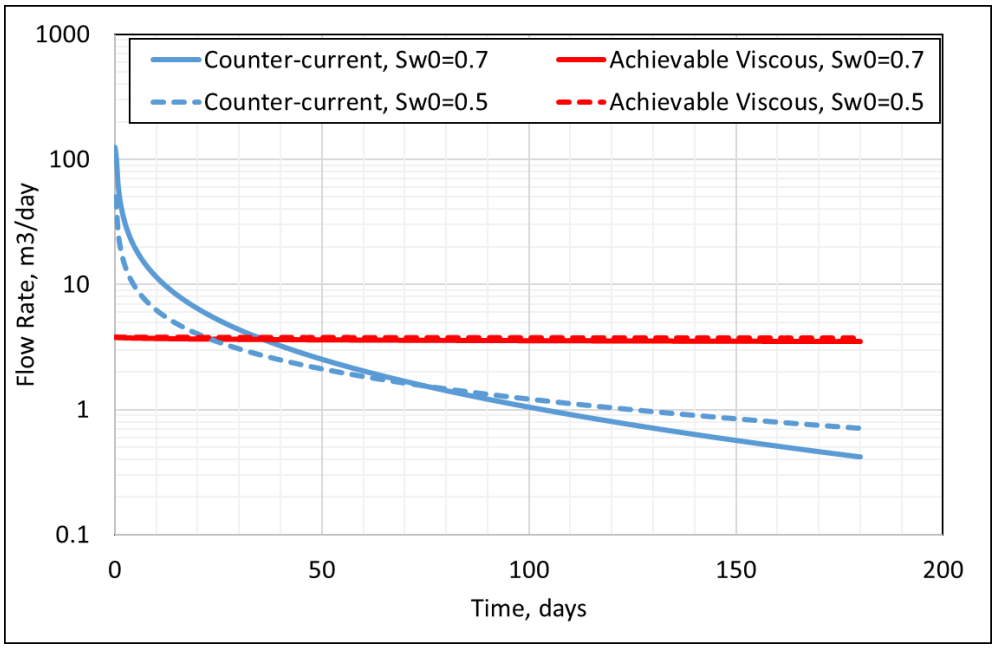

Figure 4.13 Counter-current and achievable viscous flow rates comparison between stronger and weaker water-wet cases

The above figure shows the comparison between these two cases. The difference in cross-over time is because when the system is less strong in terms of water wet, the imbibition and adsorption rate will be slower comparing with the strongly wet case. Then the weaker water wet case will approach the viscous achievable rate faster than the strongly water wet case. On the other hand, as the relative permeability of the gas phase at the free water saturation will be much higher in the weaker water case system, the mobility damage caused by water invasion is eased. Thus the damage to the viscous flow rate caused by water invasion until the cross-over time will be a lot smaller also in the

weaker water wet case. This leads to a higher compensation time comparing with the strongly water wet case.

We are also comparing the cases between the oil and gas reservoirs. As for both cases we are assuming immiscible flow, and there is few literatures discussing the physical properties such as relative permeability and capillary pressure values for unconventional reservoirs directly, we are only changing the magnitude of the hydrocarbon phase's viscosity for the current study. In the base case, the hydrocarbon phase is considered to be gas, and the viscosity is 1.5E-5 PaS. As for the synthetic oil reservoir case, we will be using 0.0015 PaS for the hydrocarbon phase.

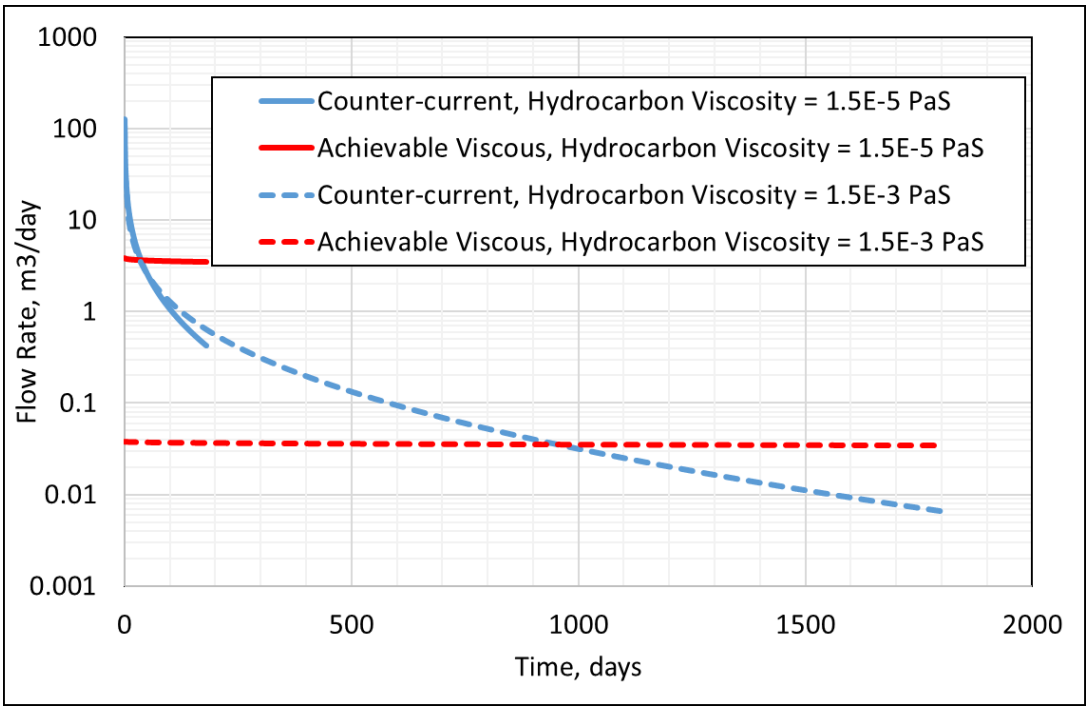

Figure 4.14 Counter-current and achievable viscous flow rates comparison between gas and oil reservoirs cases

From the above comparison, we can clearly see that for the higher viscosity (oil reservoir) case, the cross-over time is much larger. This is mainly because of the heavily

reduced achievable viscous flow rate using our current calculation method. This means that maybe soaking is even more beneficial for shale oil reservoirs, given the capillary pressure is still higher and the reservoir is still strongly water-wet. But normally the shale oil reservoirs will not be so strongly water-wet, leading to the trade-off on the benefits obtained from spontaneous imbibition and water adsorption.

4.5 Conclusions

In this chapter, we have first illustrated the impact of spontaneous imbibition in unconventional reservoirs. With the planar fracture assumption, the self-similar solution for the purely counter-current flow is applied to analyze the imbibition process between the matrix and the fracture. The results indicate that for these ultra-low permeability formations, although the imbibition velocity may not seem to be significant, the overall production rate is large due to the large contact area. Also, comparing with viscous flow by applying a pressure drop, the imbibition mechanism will yield higher production, especially at early time.

This has led us to revisit the explanation for increased production after soaking a well for some of the dry gas shale reservoirs. The mechanisms studied reconcile the apparent contradiction between current operational observations and the conventional multiphase flow theory on mobility reduction. It demonstrates that the water blocking effect is less severe compared with traditional imbibition models.

For the systems with sub-irreducible initial water saturation, the water adsorption effect is also taken into consideration in the analytic solution at the continuum scale. This presented self-similar solution is an extension of the imbibition solution studied in the previous chapter and is further extended to incorporate the gravity segregation inside the fracture to calculate the water invasion into the matrix during the soaking period. These calculations give the possibility to evaluate the damage caused by water blocking in the vicinity of the fracture surface by calculating the apparent relative permeability for the gas phase inside the matrix.

Although the invaded water will cause some mobility loss for the gas phase, the counter-currently produced hydrocarbon will also be beneficial to the production later. Thus, we have compared the viscous achievable gas flow rate with the counter-current gas rate by spontaneous imbibition and water adsorption and defined the cross of these two flow rates as the cross-over time. Theoretically, this cross-over time should act as the benchmark for the soaking time management to balance the trade-off between damage and additional production. Before this time, the imbibition and adsorption should really be considered as a production mechanism. But after this time, further soaking would probably damage the matrix. Also, the long-term impact caused by well soaking is quantified by another compensation time for the production loss due to water blocking.

CHAPTER V

CONCLUSIONS AND FUTURE WORK

5.1 Summary and Conclusions

This work studied the fundamental behavior of two-phase flow mechanisms in porous media. More specifically, both the Buckley-Leverett type viscous dominated flow with capillary corrections and the capillary dominated spontaneous imbibition are studied along with analytic solution being provided. This work is important because the analytic solutions, in their Lagrangian forms, are better comparing with numerical simulations in capturing the behavior of frontal advances. As in the spontaneous imbibition case, the numerical simulation will also have a hard time representing the actual boundary condition.

In the first study considering the capillary corrections to Buckley-Leverett flow:

1) We provided an extension of the Buckley-Leverett solution for multiphase flow to include capillary pressure corrections. The analytic solution is given by matched asymptotic expansions and the composite solution is a continuous solution which smoothly transitions across the Buckley-Leverett shock. The solution has been validated using numerical finite difference simulation.
2) A new dimensionless group has been introduced to describe the relative magnitude of capillary and viscous forces at the continuum scale. This dimensionless parameter is natural

3) The methodology has been applied to two laboratory-scale examples. The first has been to the prediction and analysis of the capillary end effect seen in core flood measurements. The second has been to use the experimental saturation profile to calibrate capillary pressure function.

In the above first part, our scope was restrained to viscous dominated flow as we are treating the capillarity as a correction only. In the second part of this study, we have moved from the viscous dominated flow condition to capillary dominated flow condition to complete our investigation.

1) The analytic solution for spontaneous imbibition originally developed by other authors in the literature has been studied, and more exact transient solutions have been developed. The solution strategy is a shooting algorithm as the problem in nature is a two-point boundary value problem.
2) Applied the transient solution to situations with physical outlet boundary conditions and validated with bespoke numerical simulation. There are mainly two transient problems analyzed, one is the constant outlet flux boundary condition, and the other is the outlet pressure boundary condition which is represented by the TEO free spontaneous imbibition experiment.
3) The outcome stability envelope is a new result to predict the rate of spontaneous water imbibition and counter-current oil production. And according to the predicted imbibition rate, the envelope could help differentiate stable and unstable situations during any imbibition process.

In the last part, we have applied the spontaneous imbibition solution to the unconventional reservoirs to quantitatively evaluate the impact from capillarity on hydraulically fractured shale reservoirs.

1) The production rate by imbibition in unconventional reservoirs is higher than what is achievable under normal viscous pressure drop. And also, due to the large cross-sectional area open for flow after hydraulic fracturing, higher volume is being produced due to imbibition as well.
2) We have extended self-similar analytical solution for quantitative evaluation of combined spontaneous imbibition and water adsorption at the continuum scale. We have also incorporated gravity segregation in hydraulic fractures during soaking period.
3) We have evaluated the mobility loss for the hydrocarbon phase and its trade-off in the presence of spontaneous imbibition counter-current flow. We proposed cross-over time for soaking time management, and we also proposed compensation time for long-term comparison between water invasion related damage and additional gain.

5.2 Suggestions for Future Work

Our work has proved that the spontaneous imbibition in unconventional reservoirs is beneficial for the initial production. This theory has provided further insight into the application of IOR techniques in tight formations. The counter-current flow rates are

extremely high at the early time. Even though the flow rate is decreasing rapidly due to combined effect from decreasing imbibition velocity and closing imbibition cross-sectional area, there still exists a long period where the flow rate by spontaneous imbibition is much higher than what is achievable under viscous pressure drops. Thus, we are trying to investigate one IOR technique that could possibly benefit the shale gas production, which is through water huff-n-puff.

At the initial condition of soaking after fracturing, water will be spontaneously imbibed from the fracture into the matrix due to capillary force. In the case where the initial water saturation is sub-irreducible, the water leak-off is controlled by adsorption in the presence of clay minerals. The counter-current imbibition rate drops rapidly from infinity and the fracture will be filled with counter-currently produced hydrocarbon progressively. Once the flow rate drops to a prescribed value or the fracture is fully occupied by hydrocarbon to cause the cessation of imbibition, the soaking of this cycle should be stopped for better huff-n-puff management. Following the production of hydrocarbon from fracture, water is re-injected to re-establish the imbibition condition at the fracture/matrix interface for the next cycle with higher initial water saturation inside the matrix.

Due to the high flow rate at the beginning of each cycle, the soaking is essential for the matrix to charge the fracture with hydrocarbon. The soaking time for each cycle may be increased in early period due to slower counter-current imbibition rate while still controlled by fracture pore volume. With the imbibition rate being even smaller, the soaking time should decrease due to faster decline to the target rate.

We believe that this IOR technique will indeed help higher bring higher production from unconventional reservoirs. One key future step for this proposed study is to investigate the possible paths to simulate the imbibition process through a commercial simulator or build a three-dimensional simulator. The analytic solution is good for constant initial saturation, however why we start to analyze different imbibition cycles, the capillary equilibrium and redistribution will happen after soaking and the saturation profile inside the matrix for the start of the next cycle will not be uniform. This situation is not easily tackled using analytic solution. Once the simulator is properly set up, the study could be carried on by finding the optimized huff-n-puff scenario.

REFERENCES

Abrams, A. and Vinegar, H.J. 1985. Impairment Mechanisms in Vicksburg Tight Gas Sands. Paper presented at the SPE/DOE Low Permeability Gas Reservoirs Symposium, Denver, Colorado, 19-22 March. SPE-13883-MS. Society of Petroleum Engineers. DOI: 10.2118/13883-MS.

Agrawal, S. and Sharma, M. 2013. Impact of Liquid Loading in Hydraulic Fractures on Well Productivity. Paper presented at the SPE Hydraulic Fracturing Technology Conference, The Woodlands, Texas, 4-6 February. SPE-163837-MS. Society of Petroleum Engineers. DOI: 10.2118/163837-MS.

Babchin, A., Brailovsky, I., Gordon, P. et al. 2008. Fingering Instability in Immiscible Displacement. *Physical Review E* **77** (2): 026301.

Barenblatt, G.I. 1952. On Self-Similar Movement of Compressible Fluid in a Porous Medium. *Prikladnaya Matematika i Mekhanika* **16** (6): 679-698.

Batycky, J.P., McCaffery, F.G., Hodgins, P.K. et al. 1981. Interpreting Relative Permeability and Wettability from Unsteady-State Displacement Measurements. *Society of Petroleum Engineers Journal* **21** (03): 296-308. SPE-9403-PA. DOI: 10.2118/9403-PA

Bell, J.B. and Shubin, G.R. 1985. Higher-Order Godunov Methods for Reducing Numerical Dispersion in Reservoir Simulation. Presented at the SPE Reservoir Simulation Symposium, Dallas, Texas, 10-13 February. SPE-13514-MS. DOI: 10.2118/13514-MS.

Bennion, B.D. and Thomas, F.B. 2005. Formation Damage Issues Impacting the Productivity of Low Permeability, Low Initial Water Saturation Gas Producing Formations. *Transactions of the ASME*. **127**: 240-247.

Bertoncello, A., Wallace, J., Blyton, C. et al. 2014. Imbibition and Water Blockage in Unconventional Reservoirs: Well-Management Implications During Flowback and Early Production. *SPE Reservoir Evaluation and Engineering* **17** (04): 497-506. DOI: 10.2118/167698-PA.

Bjørnarå, T.I. and Mathias, S.A. 2013. A Pseudospectral Approach to the Mcwhorter and Sunada Equation for Two-Phase Flow in Porous Media with Capillary Pressure. *Computational Geosciences* **17** (6): 889-897. DOI: 10.1007/s10596-013-9360-4

Bostrom, N., Chertov, M., Pagels, M. et al. 2014. The Time-Dependent Permeability Damage Caused by Fracture Fluid. Paper presented at the SPE International Symposium and Exhibition on Formation Damage Control, Lafayette, Louisiana, 26-28 March. SPE-168140-MS. Society of Petroleum Engineers. DOI: 10.2118/168140-MS.

Buckley, S.E. and Leverett, M.C. 1942. Mechanism of Fluid Displacement in Sands. *Transactions of the AIME* **146** (01): 107-116. SPE-942107-G. DOI: 10.2118/942107-G

Cai, J., You, L., Hu, X. et al. 2012. Prediction of Effective Permeability in Porous Media Based on Spontaneous Imbibition Effect. *International Journal of Modern Physics C*. **23**. DOI: 10.1142/S0129183112500544.

Chen, Z.X. 1988. Some Invariant Solutions to Two-Phase Fluid Displacement Problems Including Capillary Effect (Includes Associated Papers 18744 and 19037). *SPE Reservoir Enginnering* **3** (02): 691-700. SPE-14874-PA. DOI: 10.2118/14874-PA

Cheng, Y. 2012. Impact of Water Dynamics in Fractures on the Performance of Hydraulically Fractured Wells in Gas-Shale Reservoirs. *Journal of Canadian Petroleum Technology* **51** (02): 143-151. DOI: 10.2118/127863-PA

Chuoke, R.L., van Meurs, P., and van der Poel, C. 1959. The Instability of Slow, Immiscible, Viscous Liquid-Liquid Displacements in Permeable Media. *Petroleum Transactions, AIME* **216**: 188-194. SPE-1141-G. DOI: 10.2118/1141-G

Dake, L.P. 1983. *Fundamentals of Reservoir Engineering*: Elsevier. Original edition. ISBN 008056898X.

Das, P., Achalpurkar, M., and Pal, O. 2014. Impact of Formation Softening and Rock Mechanical Properties on Selection of Shale Stimulation Fluid: Laboratory Evaluation. Paper presented at the SPE/EAGE European Unconventional Resources Conference and Exhibition, Vienna, Austria, 25-27 February. SPE-167787-MS. Society of Petroleum Engineers. DOI: 10.2118/167787-MS.

Dehghanpour, H., Zubair, H.A., Chhabra, A. et al. 2012. Liquid Intake of Organic Shales. *Energy Fuels* **26** (09): 5750-5758. DOI: 10.1021/ef3009794

Deng, L. and King, M.J. 2015. Capillary Corrections to Buckley-Leverett Flow. Presented at the SPE Annual Technical Conference and Exhibition, Houston, Texas, 28-30 September. SPE-175150-MS. DOI: 10.2118/175150-MS.

Deng, L. and King, M.J. 2016. Estimation of Relative Permeability from Laboratory Displacement Experiments: Application of the Analytic Solution with Capillary Corrections. Presented at the Abu Dhabi International Petroleum Exhibition & Conference, Abu Dhabi, UAE, 7-10 November. SPE-183139-MS. DOI: 10.2118/183139-MS.

Deng, L. and King, M.J. 2018a. Theoretical Investigation of the Transition from Spontaneous to Forced Imbibition. Paper presented at the SPE Improved Oil Recovery Conference, Tulsa, Oklahoma, 14-18 April. SPE-190309-MS. Society of Petroleum Engineers. DOI: 10.2118/190309-MS.

Deng, L. and King, M.J. 2018b. Theoretical Investigation of Water Blocking in Unconventional Reservoirs Due to Spontaneous Imbibition and Water Adsorption. Paper presented at the Unconventional Resources Technology Conference, Houston, Texas, 23-25 July. URTEC-2875353-MS. Unconventional Resources Technology Conference. DOI: 10.15530/URTEC-2018-2875353.

Deng, L. and King, M.J. 2018c. Theoretical Investigation of Two-Ends-Open Free Spontaneous Imbibition. Paper presented at ECMOR XVI: 16th European Conference on the Mathematics of Oil Recovery, Barcelona, Spain, 3-6 September.

Deng, L. and King, M.J. 2018d. Theoretical Investigation of the Transition from Spontaneous to Forced Imbibition. *SPE Journal*. SPE-190309-PA. DOI: 10.2118/190309-PA

Desai, K.R., Pradhan, V.H., Daga, A.R. et al. 2015. Approximate Analytical Solution of Non-Linear Equation in One Dimensional Imbibitions Phenomenon in

Homogeneous Porous Media by Homotopy Perturbation Method. *Procedia Engineering* **127**: 994-1001. DOI: 10.1016/j.proeng.2015.11.448

Dutta, R., Lee, C., Odumabo, S. et al. 2012. Quantification of Fracturing Fluid Migration due to Spontaneous Imbibition in Fractured Tight Formations. Paper presented at the SPE Americas Unconventional Resources Conference, Pittsburgh, Pennsylvania, 5-7 June. SPE-154939-MS. Society of Petroleum Engineers. DOI: 10.2118/154939-MS.

Fan, L., Thompson, J. W., and Robinson, J. R. 2010. Understanding Gas Production Mechanism and Effectiveness of Well Stimulation in the Haynesville Shale Through Reservoir Simulation. Paper presented at the Canadian Unconventional Resources and International Petroleum Conference, Calgary, Alberta, Canada, 19-21 October. SPE-136696-MS. Society of Petroleum Engineers. DOI: 10.2118/136696-MS.

Farajzadeh, R., Meulenbroek, B., Daniel, D. et al. 2013. An Empirical Theory for Gravitationally Unstable Flow in Porous Media. *Computational Geosciences* **17** (3): 515-527. DOI: 10.1007/s10596-012-9336-9

Fayers, F.J. and Sheldon, J.W. 1959. The Effect of Capillary Pressure and Gravity on Two-Phase Fluid Flow in a Porous Medium. *Petroleum Transactions, AIME* **216**: 147-155. SPE-1089-G. DOI: 10.2118/1089-G

Ferno, M.A., Haugen, A., Brattekas, B. et al. 2015. Quick and Affordable SCAL: Spontaneous Core Analysis. International Symposium of the Society of Core Analysis. Society of Core Analysis. SCA2015-003.

Fučík, R., Mikyška, J., Beneš, M. et al. 2007. An Improved Semi-Analytical Solution for Verification of Numerical Models of Two-Phase Flow in Porous Media. *Vadose Zone Journal* **6** (1): 93-104. DOI: 10.2136/vzj2006.0024

Hadley, G. F. and Handy, L. L. 1956. A Theoretical and Experimental Study of the Steady State Capillary End Effect. Paper presented at Fall Meeting of the Petroleum Branch of AIME, 14-17 October, Los Angeles, California. SPE-707-G. Society of Petroleum Engineers. DOI:10.2118/707-G

Haugen, A., Ferno, M.A., Mason, G. et al. 2014. Capillary Pressure and Relative Permeability Estimated from a Single Spontaneous Imbibition Test. *Journal of Petroleum Science and Engineering* **115**: 66-77. DOI: 10.1016/j.petrol.2014.02.001.

Heaviside, J. and Black, C.J.J. 1983. Fundamentals of Relative Permeability: Experimental and Theoretical Considerations. Presented at the SPE Annual Technical Conference and Exhibition, San Francisco, California, 5-8 October. SPE-12173-MS. DOI: 10.2118/12173-MS.

Helba, A.A., Sahimi, M., Scriven, L.E. et al. 1992. Percolation Theory of Two-Phase Relative Permeability. *SPE Reservoir Engineering* **7** (01): 123-132. SPE-11015-PA. DOI: 10.2118/11015-PA

Holditch, S.A. 1979. Factors Affecting Water Blocking and Gas Flow from Hydraulically Fractured Gas Wells. *Journal of Petroleum Technology* **31** (12): 1515-1524. DOI: 10.2118/7561-PA.

Johnson, E.F., Bossler, D.P., and Naumann Bossler, V.O. 1959. Calculation of Relative Permeability from Displacement Experiments. *Petroleum Transactions, AIME* **216**: 370-372. SPE-1023-G. DOI: 10.2118/1023-G.

Jones, S.C. and Roszelle, W.O. 1978. Graphical Techniques for Determining Relative Permeability from Displacement Experiments. *Journal of Petroleum Technology* **30** (05): 807-817, SPE-6045-PA. DOI: 10.2118/6045-PA.

Karimaie, H., Pourmohammadi, S., Samiei, M. et al. 2004. 1D-Simulation of Countercurrent Imbibition Process in a Water Wet Matrix Block. Paper presented at the International Symposium of the Society of Core Analysis, Abu Dhabi, UAE. Society of Core Analysis.

Kerig, P.D. and Watson, A.T. 1986. Relative-Permeability Estimation from Displacement Experiments: An Error Analysis. *SPE Reservoir Engineering* **1** (02): 175-182. SPE-12589-PA. DOI: 10.2118/12589-PA

King, M.J. and Dunayevsky, V.A. 1989. Why Waterflood Works: A Linearized Stability Analysis. Presented at the SPE Annual Technical Conference and Exhibition, San Antonio, Texas, 8-11 October. SPE-19648-MS. DOI: 10.2118/19648-MS.

Kuru, E., Parmar, J. S., and Dehghanpour, H. 2013. Drainage Against Gravity: Factors Impacting the Load Recovery in Fractures. Paper presented at the SPE Unconventional Resources Conference-USA, The Woodlands, Texas, 10-12 April. SPE-164530-MS. Society of Petroleum Engineers. DOI: 10.2118/164530-MS.

Kyte, J.R. and Rapoport, L.A. 1958. Linear Waterflood Behavior and End Effects in Water-Wet Porous Media. *Journal of Petroleum Technology* **10** (10): 47-50. SPE-929-G. DOI: 10.2118/929-G

Lee, S., von Allmen, P., Fink, W. et al. 2005. Comparison of Multi-Objective Genetic Algorithms in Optimizing Q-Law Low-Thrust Orbit Transfers. Paper presented at GECCO, Washington DC, USA, 25-29 June.

Longoria, R. A., Liang, T., Nguyen, Q. P. et al. 2015. When Less Flowback Is More: A Mechanism of Permeability Damage and its Implications on the Application of EOR Techniques. Paper presented at the Unconventional Resources Technology Conference, San Antonio, Texas, 20-22 July. URTEC-2154266-MS. Unconventional Resources Technology Conference. DOI: 10.15530/URTEC-2015-2154266.

Longoria, R.A., Liang, T., Huynh, U.T. et al. 2017. Water Blocks in Tight Formations: The Role of Matrix/Fracture Interaction in Hydrocarbon-Permeability Reduction and Its Implications in the Use of Enhanced Oil Recovery Techniques. *SPE Journal* **22** (05): 1393-1401, SPE-185962-PA. DOI: 10.2118/185962-PA

Makhanov, K., Habibi, A., Dehghanpour, H. et al. 2014. Liquid Uptake of Gas Shales: A Workflow to Estimate Water Loss During Shut-in Periods after Fracturing Operations. *Journal of Unconventional Oil and Gas Resources* **7**: 22-23. DOI: 10 .1016/j.juogr.2014.04.001.

McEwen, C.R. 1959. A Numerical Solution of the Linear Displacement Equation with Capillary Pressure. *Journal of Petroleum Technology* **11** (08): 45-48. SPE-1160-G. DOI: 10.2118/1160-G

McWhorter, D.B. and Sunada, D.K. 1990. Exact Integral Solutions for Two-Phase Flow. *Water Resources Research* **26** (3): 399-413. DOI: 10.1029/WR026i003p00399

McWhorter, S. 2017. Reservoir Implications of Desiccations in Organic-Rich Shale. Presentation material at the 2017 Berg-Hughes Research Symposium at Texas A&M University.

Nicholls, C.I. and Heaviside, J. 1988. Gamma-Ray-Absorption Techniques Improve Analysis of Core Displacement Tests. *SPE Formation Evaluation* **3** (01): 69-75. SPE-14421-PA. DOI: 10.2118/14421-PA

Nooruddin, H.A. and Blunt, M.J. 2016. Analytical and Numerical Investigations of Spontaneous Imbibition in Porous Media. *Water Resources Research* **52** (9): 7284-7310. DOI: 10.1002/2015WR018451

Odusina, E. O., Sondergeld, C. H., and Rai, C. S. 2011. NMR Study of Shale Wettability. Paper presented at the Canadian Unconventional Resources Conference, Calgary, Alberta, Canada, 15-17 November. SPE-147371-MS. Society of Petroleum Engineers. DOI: 10.2118/147371-MS.

Osher, S. 1984. Riemann Solvers, the Entropy Condition, and Difference. *SIAM Journal on Numerical Analysis* **21** (2): 217-235.

Parmar, J. S., Dehghanpour, H. and Kuru, E. 2013. Displacement of Water by Gas in Propped Fractures: Combined Effects of Gravity, Surface Tension, and Wettability. *Journal of Unconventional Oil and Gas Resources* **5**: 10-21. DOI: 10.1016/j.juogr.2013.11.005.

Qadeer, S., Dehghani, K., Ogbe, D.O. et al. 1988. Correcting Oil/Water Relative Permeability Data for Capillary End Effect in Displacement Experiments. Presented at the SPE California Regional Meeting, Long Beach, California, 23-25 March. SPE-17423-MS. DOI: 10.2118/17423-MS.

Rapoport, L.A. and Leas, W.J. 1953. Properties of Linear Waterfloods. *Journal of Petroleum Technology* **5** (05): 139-148. SPE-213-G. DOI: 10.2118/213-G

Rashid, B., A., M., Bal, A. et al. 2012. Quantifying the Impact of Permeability Heterogeneity on Secondary-Recovery Performance. *SPE Journal* **17** (02): 455-468. SPE-135125-PA. DOI: 10.2118/135125-PA

Richmond, P.C. and Watsons, A.T. 1990. Estimation of Multiphase Flow Functions from Displacement Experiments. *SPE Reservoir Engineering* **5** (01): 121-127. SPE-18569-PA. DOI: 10.2118/18569-PA

Roychaudhuri, B., Tsotsis, T. T., and Jessen, K. 2011. An Experimental and Numerical Investigation of Spontaneous Imbibition in Gas Shales. Paper presented at the SPE Annual Technical Conference and Exhibition, Denver, Colorado, 30 October-2 November. SPE-147652-MS. Society of Petroleum Engineers. DOI: 10.2118/147652-MS.

Ruth, D.W., Mason, G., Ferno, M.A. et al. 2015. Numerical Simulation of Combined Co-current/Counter-current Spontaneous Imbibition. Paper presented at the International Symposium of the Society of Core Analysis, St. John's, Newfoundland and Labrador, Canada. Society of Core Analysis.

Schmid, K.S., Alyafei, N., Geiger, S. et al. 2016. Analytical Solutions for Spontaneous Imbibition: Fractional-Flow Theory and Experimental Analysis. *SPE Journal* **21** (06): 2308-2316, SPE-184393-PA. DOI: 10.2118/184393-PA

Schmid, K.S. and Geiger, S. 2012. Universal Scaling of Spontaneous Imbibition for Water-Wet Systems. *Water Resources Research* **48** (3). DOI: 10.1029/2011WR011566.

Shaoul, J. R., Van Zelm, L. F., and De Pater, H. J. 2011. Damage Mechanisms in Unconventional Gas Well Stimulation - A New Look at an Old Problem. Paper presented at the SPE Middle East Unconventional Gas Conference and Exhibition, Muscat, Oman, 31 January-2 February. SPE-142479-MS. Society of Petroleum Engineers. DOI: 10.2118/142479-MS.

Sigmund, P.M. and McCaffery, F.G. 1979. An Improved Unsteady-State Procedure for Determining the Relative-Permeability Characteristics of Heterogeneous Porous Media (Includes Associated Papers 8028 and 8777). *Society of Petroleum Engineers Journal* **19** (01): 15-28. SPE-6720-PA. DOI: 10.2118/6720-PA

Steigemeir, G.L. 1977. Mechanisms of Entrapment and Mobilization of Oil in Porous Media. In *Improved Oil Recovery by Surfactant and Polymer Flooding*: New York: Academic Press.

Tannich, J.D. 1975. Liquid Removal from Hydraulically Fracture Gas Wells. *Journal of Petroleum Technology* **27** (11): 1309-1317. DOI: 10.2118/5113-PA.

Terwilliger, P.L., Wilsey, L.E., Hall, H.N. et al. 1951. An Experimental and Theoretical Investigation of Gravity Drainage Performance. *Journal of Petroleum Technology* **3** (11): 285-296. SPE-951285-G. DOI: 10.2118/951285-G

Wallach, R. 1998. A Small Perturbations Solution for Nonequilibrium Chemical Transport through Soils with Relatively High Desorption Rate. *Water Resources Research* **34** (1): 149-154. DOI: 10.1029/97WR02490

Wang, F.P. and Reed, R.M. 2009. Pore Networks and Fluid Flow in Gas Shales. Paper presented at the SPE Annual Technical Conference and Exhibition, New Orleans, Louisiana, 4-7 October. SPE-124253-MS. Society of Petroleum Engineers. DOI: 10.2118/124253-MS.

Welge, H.J. 1952. A Simplified Method for Computing Oil Recovery by Gas or Water Drive. *Journal of Petroleum Technology* **4** (4): 91-98. SPE-124-G. DOI: 10.2118/124-G

Wellington, S.L. and Vinegar, H.J. 1987. X-Ray Computerized Tomography. *Journal of Petroleum Technology* **39** (08): 885-898. SPE-16983-PA. DOI: 10.2118/16983-PA

Wu, Y.-S. and Pan, L. 2003. Special Relative Permeability Functions with Analytical Solutions for Transient Flow into Unsaturated Rock Matrix. *Water Resources Research* **39** (4): DOI: 10.1029/2002WR001495

Yortsos, Y.C. and Fokas, A.S. 1983. An Analytical Solution for Linear Waterflood Including the Effects of Capillary Pressure. *Society of Petroleum Engineers Journal* **23** (01): 115 - 124, SPE-9407-PA. DOI: 10.2118/9407-PA

Zazovskii, A.F. 1985. Structure of Discontinuities in Problems of Oil Displacement by Reactants That Influence the Phase Equilibrium. *Fluid Dynamics* **20** (5): 765-774. DOI: 10.1007/BF01050091

APPENDIX A:

MASS BALANCE CLOSURE FOR BUCKLEY-LEVERETT SOLUTION WITH CAPILLARY CORRECTIONS

To complete the solution, the function $X_0(t)$ must be obtained for the inner solution, Eq (2.29). It will be obtained by a mass balance closure of the composite solution from the inlet $(X=0, f_w=1)$ to the unknown location of the foot of the profile $\left(X = X_{foot}(T), S^C = 0\right)$. We express the unknowns in terms of the inner saturation at the foot S_1, and at the inlet S_2.

For the equations involved in the mass balance closure, at the foot of the saturation profile, we have $X_{foot}(T)$, $S^O_{foot} = S^* - S_1$, $S^I_{foot} = S_1$ and $S^C_{foot} = 0$. On the other hand, at the inlet of the system, we have $X=0$, $S^O_{inlet} = 1$, $S^I_{inlet} = S_2$ and $S^C_{inlet} = 1 - \left(S^* - S_2\right)$.

First, we express the equations for the foot in terms of both the outer and the inner solutions.

$$X_{foot} = T \cdot F_w'\left(S^O_{foot}\right) = X_0 - \frac{\varepsilon}{q} H\left(S_1\right) \tag{A.1}$$

This determines X_0 within the expression for the inner solution. Since $S^O_{foot} < S^*$, the position of the foot is advanced beyond the Buckley-Leverett shock location. However, to maintain monotonicity, we must have $F_w''\left(S^O_{foot}\right) < 0$, which places a constraint on these closure equations.

$$X = T \cdot F_w'\left(S_{foot}^O\right) - \frac{\varepsilon}{q}\left\{H\left(S^I\right) - H\left(S_1\right)\right\} \tag{A.2}$$

This expression may be evaluated at the inlet to determine S_2.

$$T \cdot F_w'\left(S_{foot}^O\right) = \frac{\varepsilon}{q}\left\{H\left(S_2\right) - H\left(S_1\right)\right\} \tag{A.3}$$

The overall mass balance follows from Eq (2.12).

$$T = \int_{Inlet}^{Foot} S^C dX = \int_{Inlet}^{Foot} S^O dX - \int_{Inlet}^{Foot}\left(S^* - S^I\right) dX \tag{A.4}$$

From the outer solution we have:

$$\int_{Inlet}^{Foot} S^O dX = T \cdot \left\{1 + S_{foot}^O \cdot F_w'\left(S_{foot}^O\right) - F_w\left(S_{foot}^O\right)\right\} \tag{A.5}$$

From the inner solution we have:

$$\int_{Inlet}^{Foot}\left(S^* - S^I\right) dX = \frac{\varepsilon}{q}\left\{M\left(S_2\right) - M\left(S_1\right)\right\} \quad where \quad M\left(S^I\right) = \int_0^{S^I} \frac{\left(S^* - S\right)G\left(S\right)}{cS - F_w\left(S\right)} dS \tag{A.6}$$

Combining these equations, and substituting for S_{foot}^O, we have:

$$\frac{qT}{\varepsilon} = \frac{H\left(S_2\right) - H\left(S_1\right)}{F_w'\left(S_{foot}^O\right)} = \frac{M\left(S_2\right) - M\left(S_1\right)}{S_{foot}^O F_w'\left(S_{foot}^O\right) - F_w\left(S_{foot}^O\right)} \quad where \quad S_{foot}^O = S^* - S_1 \tag{A.7}$$

If we treat S_{foot}^I as the independent variable, then we have two relations in terms of S_1. First, we have an equation for the inner saturation at the inlet $S_{inlet}^I = S_2$. Second, we also determine the strength of capillarity through the dimensionless variable ε_D.

An example of this construction is shown in Figure A.1. In Figure A.1a, for a specific value of S_1, the functions within Eq (A.7) are each plotted as functions of $S^* - S_2$. Where they cross determines S_2 and also ε_D. This construction is repeated for a range of values of S_1, to generate Figure A.1b. As discussed earlier, monotonicity requires that $F_w''\left(S_{foot}^O\right) < 0$, $S_{foot}^O = S^* - S_1$, which places a constraint on the maximum possible value for S_1. This requirement is graphically shown in Figure A.2a and Figure A.2b.

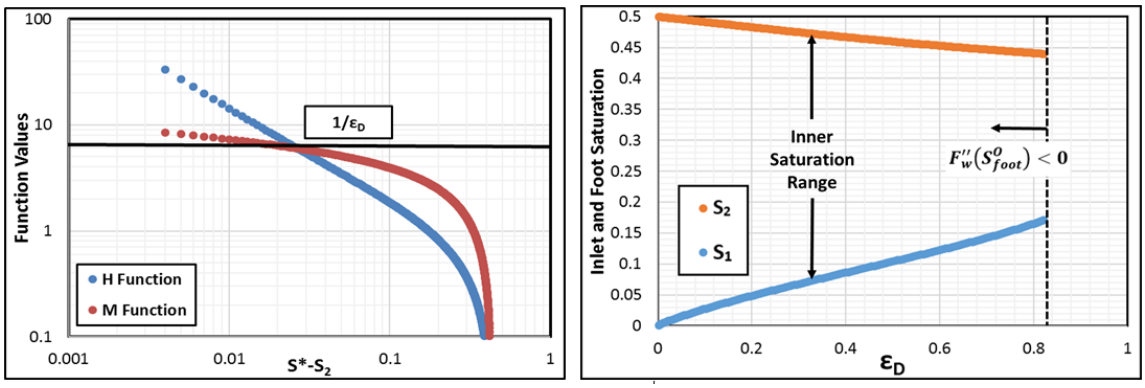

Figure A.1 (a)-Mass balance closure integral functions plotted vs S^*-S_2; (b)-inner solution saturation at inlet and foot as a function of the dimensionless capillary group

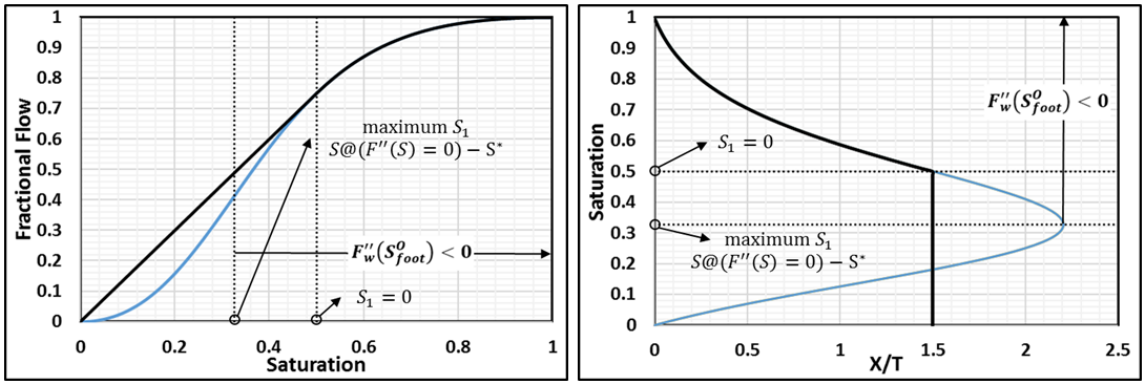

Figure A.2 (a)-Graphical interpretation of monotonicity requirement from fractional flow curve; (b)-Graphical interpretation of monotonicity requirement from saturation profile

The small ε_D behavior of the $H(S)$ and $M(S)$ functions can be determined analytically as the integrand in each is singular as $S \to S^*$. We can expand the denominator in a power series at the shock saturation:

$$cS - F_w(S) = \left\{cS^* - F_w(S^*)\right\} + (S - S^*)\left\{c - F'_w(S^*)\right\} + \tfrac{1}{2}(S - S^*)^2\left\{-F''_w(S^*)\right\} + \ldots \tag{A.8}$$

The constant and linear terms both vanish because of the properties of the shock saturation. Hence, we may approximate each of the functions.

$$H(S)=\int_{S=0}\frac{G(S)}{cS-F_w(S)}dS$$
$$\approx-\int_{S=0}\frac{2G(S^*)}{(S-S^*)^2F_w''(S^*)}dS=-\frac{2G(S^*)}{F_w''(S^*)}\left\{\frac{1}{S^*-S}-\frac{1}{S^*}\right\} \tag{A.9}$$

$$M(S)=\int_{S=0}\frac{(S^*-S)G(S)}{cS-F_w(S)}dS$$
$$\approx-\int_{S=0}\frac{2G(S^*)}{(S^*-S)F_w''(S^*)}dS=-\frac{2G(S^*)}{F_w''(S^*)}\ln\left(\frac{S^*-S}{S^*}\right) \tag{A.10}$$

We may apply the expression for $H(S)$, to Eq (A.3) to obtain S_2 to leading order. Because of the double pole in this integrand, $S^*-S_2=Order(\varepsilon_D)$. A similar analysis from the mass balance relationship shows that $S_1=Order(\varepsilon_D\ln\varepsilon_D)$. The dimensionless group, ε_D, is the small parameter which controls the validity of our perturbative expansion.

With the above derivation, all terms required for the composite solution for the capillary corrections to Buckley-Leverett flow equation are determined.

APPENDIX B:

CONVERGENCE ANALYSIS OF THE ANALYTIC SOLUTION FOR TRANSIENT IMBIBITION USING FINITE DIFFERENCE APPROACH

In this section, we will show the convergence analysis of finite difference method we used for the transient imbibition solution. Since we have two parts of discretization here, both in S_w and in T^{Im}, we performed the truncation analysis with different levels of discretization on both parameters, and have determined the convergence rate for the dimensionless capillary parameter $\varepsilon_D{}^{\mathrm{Im}}$. The following truncation analysis is done using the input parameters and model configuration from TEO free spontaneous imbibition discussed in the previous chapter.

The analysis is performed by fitting the equation:

$$\varepsilon_D{}^{\mathrm{Im}}\left(N_T, N_{S_w}\right) = \left[\varepsilon_D{}^{\mathrm{Im}}\right]_{true} + a \cdot N_{T^{\mathrm{Im}}}{}^{-b} + c \cdot N_{S_w}{}^{-d} \tag{B.1}$$

The left-hand side of the above equation represents the calculated value of $\varepsilon_D{}^{\mathrm{Im}}$ at different levels of discretization. We utilize these calculated values and their corresponding discretization refinements to fit the above equation by changing the $\left[\varepsilon_D{}^{\mathrm{Im}}\right]_{true}$, a, b, c and d values. The parameters b and d will give us the apparent convergence rates for our finite difference approach. In this analysis, we have used 25 different choices of discretization to perform the convergence analysis. $N_{T^{\mathrm{Im}}}$ values used

are 10, 20, 30, 40 and 50 intervals, and N_{S_w} values are 100, 200, 300, 400 and 500 intervals, as shown in the following table:

$\varepsilon_D^{\text{Im}}$		$N_{T^{\text{Im}}}$				
		10	20	30	40	50
N_{S_w}	100	10.70331	10.69111	10.68734	10.68551	10.68443
	200	10.72746	10.71532	10.71157	10.70975	10.70867
	300	10.7365	10.72438	10.72064	10.71882	10.71775
	400	10.74134	10.72923	10.72549	10.72368	10.7226
	500	10.74439	10.73228	10.72855	10.72673	10.72566

Table B.1 Data used for the finite difference convergence analysis from TEO free transient imbibition

The convergence test result is shown in the following figure:

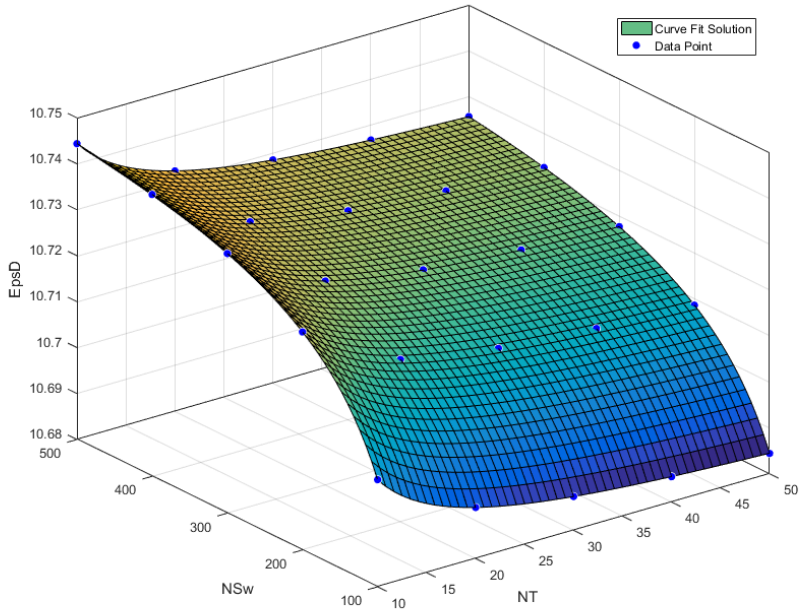

Figure B.1 Convergence solution for the finite difference convergence analysis from TEO free transient imbibition

According to the curve fitting result, the best fit equation is:

$$\varepsilon_D{}^{\mathrm{Im}}\left(N_T, N_{S_w}\right) = 10.74 + 0.2943 \cdot N_{T^{\mathrm{Im}}}{}^{-1.117} + 2.273 \cdot N_{S_w}{}^{-0.8009} \tag{B.2}$$

The R square value of the above fit is 1.0000, which indicates it is a very good fit. Through the outcome of the curve fitting for our convergence test, the solution is seen to be consistent with first order convergence on both the temporal variable and the water saturation. Other discretization scheme such as discretization in R instead of T^{Im} and its corresponding convergence is discussed in Deng and King (2018d).